

Interfacial Instabilities and Wetting Behaviour in Confinement

Siti Aminah Setu

Christ Church
University of Oxford

Supervisor: Professor Dirk Aarts

A thesis submitted for the degree of
Doctor of Philosophy

Hilary Term 2014

And it is He who has released (simultaneously) the two seas,

one fresh and sweet and one salty and bitter,

and He placed between them a barrier and prohibiting partition.

The Quran (25:53).

Abstract

Interfacial instabilities and wetting phenomena of phase separated colloid-polymer mixtures are addressed in this study. Colloidal particles offer certain advantages over molecular systems, due to their larger lengthscales and slower timescales. Moreover, the phenomena can be directly visualised using laser scanning confocal microscopy, and a perfect match with soft-lithography fabrication techniques can be exploited.

In particular, we study the viscous fingering instability in three dimensions, focusing on the role of wetting conditions and of thermal fluctuations. Combined with results obtained by lattice Boltzmann simulations, we reveal that the cross-over of the meniscus in the direction across the channel thickness is controlled by the capillary and Peclet numbers, and viscosity contrast of the system. The curvature of the meniscus has a pronounced effect on the onset of the Saffman-Taylor instability, in which the formation of the viscous fingers is suppressed up to a certain threshold. Furthermore, we investigate a related contact line instability, which leads to entrainment and subsequent droplet pinch-off. A theoretical prediction for the onset of the instability is developed, which shows a good agreement with the experimental observations and yields a method to directly measure the slip length of the interface. The large thermal fluctuations of our interface play an important role in pinch-off events, leading to periodic emission of droplets of similar sizes.

Finally, we study wetting phenomena at geometrically sculpted walls. We focus on the shape, the thickness and the radius of curvature of the adsorbed liquid film, and find good agreement with theory. Changing the curvature of the wedge from a flat surface to a capillary slit furthermore smoothly connects wetting behaviour and capillary condensation, again in qualitative agreement with theory. Non-equilibrium effects may interfere with the data and are difficult to rule out. We end with recommendations for future work.

Declaration

This thesis is submitted for the degree of Doctor of Philosophy in Physical and Theoretical Chemistry at the University of Oxford. No part of this thesis has been accepted or is currently being submitted for any degree, diploma, certificate or other qualification in this University or elsewhere. This thesis is wholly my own work, except where indicated.

Contents

Abstract **iii**

Declaration **v**

1 Interfaces at ultralow interfacial tension **1**

1.1 Colloids 2

1.2 Colloid + non-adsorbing polymer 3

1.3 Physical scales 5

1.4 Scope of the thesis 7

Appendix: Physical scales of the colloid-polymer system 8

2 Experimental system and techniques **9**

2.1 Introduction 10

2.2 PMMA-xanthan mixtures 11

2.3 Analysis of thermal capillary waves 14

2.4 Experimental techniques 19

2.4.1 Rheology 19

2.4.2 Fabrication of microfluidic devices 22

2.4.3 Confocal microscopy 24

2.5 Conclusion 28

Appendix: Physical properties of the PMMA-xanthan mixtures 29

3 The Saffman-Taylor instability **31**

3.1 Introduction 32

3.2 Origin of the Saffman-Taylor instability 34

3.3 McLean-Saffman 2D predictions 35

3.4 The 3^{rd} dimension 36
3.5 Viscous fingering at ultralow interfacial tension 39
3.6 Conclusion 40

4 Viscous fingering at ultralow interfacial tension: the 3^{rd} dimension **41**

4.1 Introduction 42
4.2 Experimental details 44
4.2.1 Experimental set-up 44
4.2.2 Image analysis 45
4.3 Lattice Boltzmann simulation 48
4.4 Results and discussion 49
4.4.1 Three-dimensional profile 49
4.4.2 Comparison with lattice Boltzmann simulations 50
4.4.3 Steady state finger in the channel thickness direction 53
4.4.4 Curvature of the leading interface in the xz-plane 56
4.5 Conclusion 57

5 Viscous fingering at ultralow interfacial tension: xy-fingering **59**

5.1 Introduction 60
5.2 Linear stability analysis in the two-dimensional limit 61
5.3 Experimental details 64
5.4 Lattice Boltzmann simulation 65
5.5 Results and discussion 65
5.5.1 Fingering in the xy-plane 65
5.5.2 Interplay between interfacial curvature in the xz-plane and xy-fingering . 67
5.5.3 Stability of viscous fingers 70
5.6 Conclusion and outlook 73

6 Drop spitting instability in superconfinement **75**

6.1 Introduction 76
6.2 Experimental set-up 77
6.3 Results and discussion 78

6.3.1 Fluid fronts instability induced by superconfinement 78
6.3.2 Jet formation and drop emission 85
6.3.3 Related behaviour due to the thermal fluctuations 88
6.4 Conclusion 90

7 Wetting phenomena at geometrically sculpted wedges **91**
7.1 Introduction 92
7.2 Experimental details 93
7.2.1 Set-up 93
7.2.2 Image analysis 95
7.3 Results and discussion 96
7.3.1 Complete wetting on a flat substrate 96
7.3.2 Shape of the wedge walls (s) 99
7.3.3 Wetting phenomena at geometrically structured substrates 99
7.3.4 Capillary condensation 105
7.4 Conclusion and outlook 107

Summary **109**

List of publications **123**

Acknowledgments **125**

Chapter 1

Interfaces at ultralow interfacial tension

> "He has let free the two bodies of flowing water, meeting together. Between them is a barrier which they do not transgress." (The Quran) [1]

The above refers to the interface-related phenomena in nature. In our daily life, interfaces play an important role. We frequently observe interface phenomena, e.g. demixing of oil and water, floating of ice cream in soft drinks in making ice cream soda, the rise of water when putting a straw in a glass of water, etc. Scientifically, the study of the interfacial phenomena has a long ongoing history; it brings the great name of van der Waals to mind, who was the first to propose a theory of interfaces, which led to the thermodynamic description of a flat interface between a gas and a liquid [2]. In 1908, von Smoluchowski [3] then realised that the interface is actually rough, corrugated by thermal capillary waves. This observation was followed by work of Mandelstam [4], and later rediscovered by Buff *et al.* in 1965 [5]. Their theories continue to inspire other researches from a variety of fields to further study the interface.

Experimentally, the study of the fluctuations of the interface was first performed by light [6] and X-ray scattering [7,8] techniques. The capillary waves were studied at a microscopic level in computer simulations of molecular systems [9]. Recently, Aarts and co-workers [10–13] presented a new method which led to a direct visualisation of the thermal fluctuations. They simply lowered the interfacial tension γ of the system — a key characteristic of the interface — down to a few

nN/m by using colloid-polymer mixtures. Thus, the length- and time-scales of the fluctuations became accessible by confocal microscopy. The ultralow interfacial tension of the system can be understood by following the scaling relation below [14, 15]:

$$\gamma \sim \frac{\epsilon}{d^2} \sim \frac{k_B T}{2R_c^2}, \tag{1.1}$$

where ϵ is the strength of the molecular interactions and d is of the order of the molecular diameter. For a colloidal system, the attraction is entropic; thus, $\epsilon \sim k_B T$, with k_B the Boltzmann constant and T the absolute temperature. Furthermore, far away from the gas-liquid critical point, the intrinsic lengthscale is of the order of the colloidal diameter, $d \sim 2R_c$. Since the size of the colloidal suspensions is in the range of submicrometres, the interfacial tension consequently becomes ultralow. This is in contrast with that observed for atoms/molecules where the interfacial tension is of the order of a few mN/m.

Inspired by the above work, in this thesis we will use a mixture of colloidal suspensions and a polymer solution to address a number of fundamental interface-related problems. The system thus provides a different way to study the problems, in some situations giving easier access than in atomic/molecular systems, and in other cases focussing on different physics.

In this chapter, we will introduce colloids in section 1.1 and colloid-polymer mixtures in section 1.2. The properties of the colloidal interfaces and the possible consequences due to ultralow interfacial tension are given in section 1.3. In section 1.4, we present the scope of this thesis.

1.1 Colloids

Fifty years after the establishment of the colloidal particles by Thomas Graham in 1861 [16], Jean Perrin opened up a new chapter in colloid science through his simple yet brilliant experimental investigation on Brownian movement [17, 18]. This phenomenon, which studies the erratic motion of small particles due to random collisions with solvent molecules, had begun with observations of Robert Brown on pollen grains in water, and was followed by a theoretical explanation by Einstein [17, 19]. In the early 1900s, Perrin, by exploiting his favoured colloidal particles, *gamboge*, suspended in water and with the help of the optical microscopy [20, 21] was able to directly quantify the motion. His measurements helped settle the debate on the reality

of atoms and provided an unambiguous determination of Avogadro's constant. For this, and his related work on sedimentation, colloid science became intimately connected with statistical physics [19–21].

Perrin's work in a way also defined the size of colloids, balancing the gravitational effect on the particles by thermal energy. This can be expressed through a Peclet number Pe:

$$Pe = \frac{6\pi\eta R_c^3 u}{k_B T} = \frac{u R_c^2}{D}, \tag{1.2}$$

which measured the ratio of the advection to the diffusion timescales. Here, u is the sedimentation velocity and $D = k_B T/6\pi\eta R_c$, the diffusion coefficient of a spherical particle of radius R_c in a solvent of viscosity η, following the Stokes relation. For colloids with $R_c \sim \mu$m, hence $Pe \sim$1, it meant that the colloids exhibit Brownian motion and are stable against sedimentation. In practice, the size of the colloids lies roughly in between 1 nm and 1 μm, whereas atoms are typically in the range of Angstroms. This is a relevant lengthscale for application in fields as diverse as engineering, microfluidics and biology.

The larger lengthscale of the colloids consequently gives several advantages to the system over their molecular counterparts: (i) they show slower timescales of diffusion, allowing the tracking at the individual particle level. (ii) Since the lengthscale is of the order of the wavelength of light, they can be imaged using optical techniques. Recent development in laser scanning confocal microscopy (LSCM), for example, even allows to image the particles in three dimensions, giving detailed information on the local behaviour of the colloids. (iii) Colloids are "soft" material, since they are sensitive to small external forces, including thermal fluctuations. In addition, their interactions are strongly tunable, for example, by changing the electrical charge at the colloidal surface or by adding a third component (see section 1.2).

1.2 Colloid + non-adsorbing polymer

When two colloidal particles approach one another, their interaction is determined by the electrical double layer repulsion and the van der Waals attraction [22], which can be described by the DLVO potential. The potential curve has a secondary attractive minimum at a certain distance from colloidal surfaces. Experimentally, it is difficult to control the potential energy, although possible in principle [23]. However, the addition of a third component, e.g. polymers,

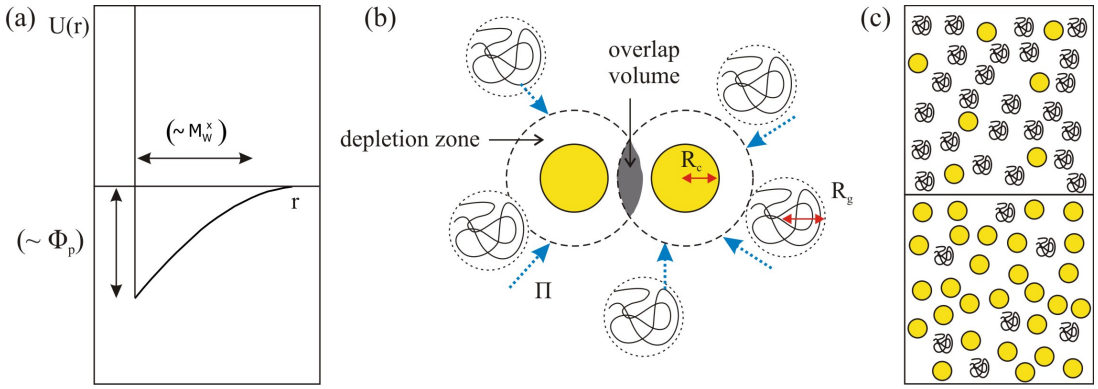


Figure 1.1: (a) Pair potential of depletion interactions determined by DLVO theory [26, 27]. (b) Schematic drawing of the depletion interaction between two colloidal particles of radius R_c surrounded by polymer coils of radius of gyration R_g. (c) Fluid-fluid phase separated colloid-polymer mixtures; (upper phase) a colloid-poor polymer-rich (gas) phase in coexistence with (lower phase) a colloid-rich polymer-poor (liquid) phase.

as mentioned above, provides an alternative and flexible method to manipulate the potential energy [24], in such a way that the depth of the potential is proportional to the thermal energy k_BT and the width is in the range of the colloidal diameter $2R_c$ [24]. Thus, the system may undergo a fluid-fluid phase separation. Figure 1.1 (a) shows the pair potential of two colloids surrounded by polymer particles, which is similar to that observed in a molecular system described by the Lennard-Jones potential [25]. Therefore, the colloidal system is an excellent model for the molecular system, with well-defined and analogous thermodynamic potential.

In particular, the addition of the non-adsorbing polymers, with radius of gyration R_g to the colloidal suspensions, leads to the so-called *depletion interaction;* there is a region around the colloidal surfaces where the centres of mass of the polymer chains will be entropically excluded. This entropy-driven interaction was first described by Asakura and Oosawa in 1954 [28, 29] and then 20 years later by Vrij [24]. If two such depletion regions overlap, then there is an osmotic imbalance pushing the particles together (see figure 1.1 (b)). The resulting effective attraction between the colloidal particles can be described as:

$$U(r) = -\Pi V_{overlap} \tag{1.3}$$

where Π is the osmotic pressure of the polymer solution, which in turn depends on the concentration of the polymers, and the overlap volume $V_{overlap}$ (indicated as the grey area in figure 1.1 (b)) is a function of the size of the polymer and of the colloid; thus, all of the interactions

are highly controllable. At sufficient concentrations of both components, a fluid-fluid demixing transition may lead to a colloid-poor polymer-rich (gas) phase in coexistence with a colloid-rich polymer-poor (liquid) phase, as shown in figure 1.1 (c) [24]. Note that a third phase is possible — an ordered colloid-rich polymer-poor (crystal) phase [30] — and even more complicated phases [31, 32]. In this thesis, we only consider the colloidal gas-colloidal liquid phases, which have been widely accepted as an analogue to the gas-liquid phase separation found in molecular liquids [33]. In addition, the phase diagram of such phase behaviour is dependent on the colloid-polymer size ratio $q = R_g/R_c$, as shown in [34–36]. The three-phase coexistence calculated using free volume theory and the polymer partitioning between phases was presented in the work of Lekkerkerker *et al.* [30, 37]. For an excellent introduction to the subject, see a recent book by Lekkerkerker and Tuinier [38].

1.3 Physical scales

The demixing process of colloid-polymer mixtures results in two separated colloidal phases with an interface between them. As mentioned above, the interfacial tension associated with this interface scales as [14, 15]:

$$\gamma \sim \frac{k_B T}{2R_c^2}. \tag{1.4}$$

Since $R_c \sim \mu$m, this leads to ultralow values for the interfacial tension of around nN/m, as has been confirmed experimentally [10, 39–44] and theoretically [45–49]. The values may easily be around six orders of magnitude smaller than those obtained for the atomic/molecular system, where the interfacial tension is in the range of mN/m.

The ultralow interfacial tension of colloid-polymer mixtures offers a unique opportunity to study a wide variety of interface-related problems, the way of which allows both the static and dynamic behaviour of interfaces to be consequently altered. Firstly, the roughness of the free interface corrugated by thermal capillary waves, which scales as:

$$L_T = \sqrt{\frac{k_B T}{\gamma}}, \tag{1.5}$$

is subsequently a thousand times larger than what it is in atomic/molecular systems. Such large interface roughness (of the order of microns) can be directly observed by using optical

microscopy [10]. Secondly, the capillary length L_c, i.e. the characteristic lengthscale of the interface fluctuations parallel to the plane, which is given by [4]:

$$L_c = \sqrt{\frac{\gamma}{g\Delta\rho}} \tag{1.6}$$

where g is Earth's acceleration and $\Delta\rho$ the density difference between the two phases, is significantly decreased — a thousand times smaller — in comparison to its molecular counterpart. It is also the typical lengthscale to measure the shape of the meniscus close to the wall [50, 51]; since L_c is small for colloid-polymer mixtures, the interface between its separated phases appears to be flat in close proximity to the wall when viewed by eye.

Furthermore, the ultralow values of interfacial tension in colloid-polymer mixtures lead to a small magnitude of the capillary velocity u_c. This is the characteristic velocity when inertia is irrelevant, given by:

$$u_c = \gamma/\eta. \tag{1.7}$$

Here, η is the viscosity, typically the sum or average of the viscosities of both phases, which depends on the problem studied. This allows to study interface phenomena such as contact line motion and droplet snap-off in great detail (chapter 6). Finally, the typical decay time τ of thermal capillary waves [52]:

$$\tau = \frac{L_c}{u_c} = \frac{L_c\eta}{\gamma}, \tag{1.8}$$

is significantly increased of the order of seconds, again since γ is ultralow. This allows to follow the fluctuations of the interface in real space. The physical properties introduced in this section are summarised in table 1.1 in the appendix and will be used frequently throughout this thesis. Clearly, all of the characteristic quantities found in the colloid-polymer system are highly compatible with length- and time-scales accessible by microfluidics and optical microscopy techniques. This allows us to study several interface-related phenomena forming the topic of this thesis.

1.4 Scope of the thesis

In this thesis we will investigate the interfacial instabilities and wetting phenomena in confined microchannels using colloid-polymer mixtures as our model fluid. We use laser scanning confocal microscopy to observe the phenomena in real-space and -time. We will highlight the consequences of ultralow interfacial tension, and focus on the special role of the strong interface fluctuations.

In chapter 2, we will describe the system and techniques used in this study. The system consists of poly(methylmethacrylate) (PMMA) colloids and non-adsorbing xanthan polymer dispersed in water. We explain the analysis of thermal capillary waves of the free interface used to obtain the physical properties of the system. Other techniques include rheology, soft-lithography and the confocal microscopy.

To avoid repetition, in chapter 3 we briefly introduce the Saffman-Taylor instability: the fingering phenomenon that emerges when a low viscous fluid displaces a more viscous one. In order to fully capture the behaviour of the viscous fingers, we first focus on the observations across the channel thickness direction (xz-plane) (chapter 4), and then continue with the observations in the wide dimension of the channel (xy-plane) (chapter 5). This work is combined with results obtained by lattice Boltzmann simulations run by Dr. I. Zacharoudiou [53]. Later, in chapter 6, we present our work on the contact line motion and droplet snap-off, which is an extension of the Saffman-Taylor fingering experiments in our microfluidics set-up. A theoretical framework developed based on diffuse interface models by Dr. R. Ledesma-Aguilar will be used to interpret the results.

In chapter 7, we turn our attention to the wetting behaviour of phase separated colloid-polymer mixtures confined to geometrically shaped wedges. This study was motivated by work of Rascón and Parry [54, 55], where a theoretical scaling argument was given to describe the wetting phenomena for different wedge shapes. Finally, we end with a conclusion of this thesis (Summary).

Appendix: Physical scales of the colloid-polymer system

Table 1.1: Summary of the physical properties in a colloid-polymer mixture [56].

			colloid + polymer
interfacial tension	γ	(N/m)	10^{-7}
viscosity	η	(Pa s)	10^{-2}
density difference	$\Delta\rho$	(kg/m^3)	10^{3}
interface roughness	L_T	(m)	10^{-7}
capillary length	L_c	(m)	10^{-5}
capillary velocity	u_c	(m/s)	10^{-5}
capillary time	τ	(s)	10^{0}

Chapter 2

Experimental system and techniques

ABSTRACT

The colloid-polymer mixtures and experimental techniques used in this thesis are introduced and described in detail. The system consists of fluorescently labelled PMMA colloids + xanthan polymer dispersed in water as a solvent, which is compatible with microfluidic devices fabricated in poly(dimethylsiloxane). We quantified the system's fluid-fluid interface fluctuations by presenting three main results, namely the interfacial roughness, the static and dynamic correlation functions, which are well described by capillary wave theory. This directly leads to the various interfacial parameters in the system, which are of central importance in studying problems concerning interfaces and wetting. As techniques, we introduce the TA AR-G2 rheometer, whose properties and measurements are described as well. We also detail how to fabricate microfluidic channels using soft-lithography as a fast, flexible and cheap fabrication technique with high reproducibility. Finally, we introduce the laser scanning confocal microscopy as a powerful technique to explore the interfacial and wetting phenomena in real space, in all three dimensions.

2.1 Introduction

This thesis aims to investigate problems concerning interfaces and wetting behaviour of complex fluids in confinement, where the interfacial tension is roughly a million times lower than in a molecular system. As our model system, we use a mixture of spherical colloids and non-adsorbing polymers, which are separated into a colloidal liquid phase (colloid-rich, polymer-poor) in coexistence with a colloidal gas phase (colloid-poor, polymer-rich) due to the depletion interaction [24, 28, 29]. This mixture has several attractive features: (i) the colloids can be fluorescently labelled using, e.g. a dye, so that they can be directly observed by means of confocal microscopy. (ii) The colloids and polymer interactions can be tuned such that a system with the desired interfacial properties can be easily constructed. (iii) Since the diameter of colloidal particles is a thousand times larger than a typical molecular diameter, the interfacial tensions are of the order of $10^{-9} - 10^{-6}$ N/m [10, 39–44]; therefore, the surface roughness is $\sim \mu$m, which is resolvable by confocal microscopy. This allows the possibility to study not only the interfacial and wetting phenomena but also the effects of thermal capillary waves.

Previous experimental work has shown the opportunities and advantages of using colloid-polymer systems in studying a range of static and dynamic interfacial phenomena in unprecedented detail (see, for example, [10, 12, 56–63]). Their work has mainly been performed on systems in organic solvents, e.g. a mixture of poly(methylmethacrylate) (PMMA) colloids + polystyrene polymer dispersed in decalin. However, it can be challenging to bring the systems in confinement, especially compatible with microfluidic devices made out of poly(dimethylsiloxane) (PDMS) elastomer (the material widely used in microfluidics [64]). Many factors have to be considered. To develop a good colloid-polymer system, both colloids and polymers should separately be stable in the solvent, such as water, which is a perfect match with PDMS, and when mixed together the polymers must be non-adsorbing. The colloids and the solvent refractive indexes should be reasonably matched in order to screen the van der Waals interactions, as well as to minimise scattering as the light passed through the sample. Furthermore, the density difference between the colloids and the solvent has to be small enough such that sedimentation is not too prominent and the chemical potential is constant over a distance of one particle diameter along the direction of gravity. Lastly, in order to obtain a stable fluid-fluid phase coexistence, the polymer radius of gyration R_g needs — as a rule of thumb — to be at least 1/3 of the colloid radius to induce the phase separation [30].

In this chapter, we will introduce the PMMA + xanthan mixtures in water (section 2.2), which have proven to be compatible with PDMS microfluidic devices (see, for example, [44, 65, 66]). In section 2.3, we study the fluctuations at the free fluid-fluid interface using capillary wave theory to determine the interfacial properties of the system. Meanwhile, the rheological properties of the system are described in section 2.4.1. The method to fabricate the microfluidic devices will be explained in section 2.4.2, and the technique of confocal microscopy will be discussed in section 2.4.3. In section 2.5, a verdict over the system and techniques will be given.

2.2 PMMA-xanthan mixtures

This system was first prepared by Dr. E. A. G. Jamie and M. D. Howe [44,67,68]. The PMMA spheres were synthesised by following the first part of the emulsion polymerisation method described by Kumacheva *et al.* [69]. The particles were fluorescently labelled by incorporation of the rhodamine dye monomer in ethanol prepared as in [70] at the final stage of the synthesis. The radius of the particles R_c was found to be 110 nm, estimated from scanning electron microscopy images (see figure 2.1; *the image was obtained by Dr. E. A. G. Jamie* [68]), and the density was 1.17 g/mL. The particle suspension has a fairly low polydispersity as it displayed a crystallising sediment. The refractive index of colloids ($n_{PMMA} = 1.49$) is slightly different from the refractive index of the solvent ($n_{water} = 1.33$), which leads to significant scattering events here compared to the systems in an organic solvent [10, 56]. The refractive index mismatch also has consequences for the strength of van der Waals forces, which can lead to irreversible aggregation of the colloidal particles. However, the particles were stabilised by charge, which makes them relatively insensitive to the van der Waals attractions, and no aggregation of the particles was observed.

The xanthan polymer solution with molecular weight $M_w = 4$ x 10^6 g/mol was prepared as described briefly in [67, 71, 72]. The polymer was kindly provided by Dr. R. H. Tromp (Nizo, Ede, The Netherlands) and was used without purification. The xanthan stock solution with concentration of 2 mg/mL contains 0.1 M NaCl to screen double-layer repulsions and 2 mM NaN_3 to prevent bacterial growth. The radius of gyration R_g and its persistence length were 264 nm and 120 nm, respectively, as estimated from data in the literature [71] which implies semiflexible double-helical xanthan chains.

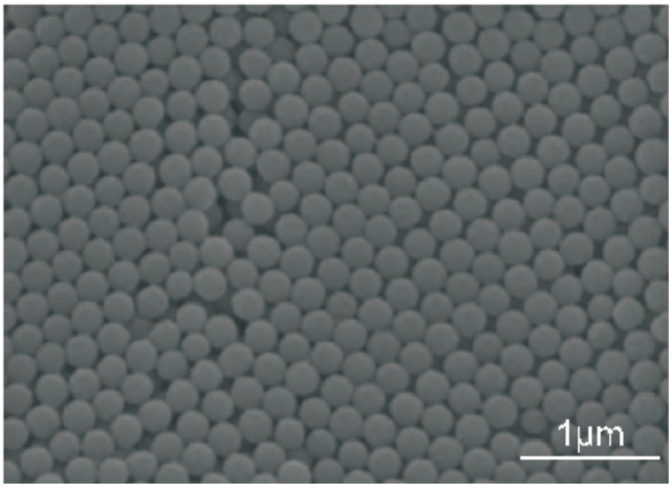


Figure 2.1: Scanning electron microscopy image of PMMA spheres with a radius of 110 nm obtained by Dr. E. A. G. Jamie. Image is taken from [68].

PMMA-xanthan samples were prepared in cut-off cuvettes with a glass microscope slide fixed to the bottom by mixing colloid- and polymer-stock dispersion and diluting with water. The phase separation was taking place if the sample immediately became turbid after homogenisation by hand. The phase diagram originally constructed by Dr. E. A. G. Jamie [68, 73] was reproduced in figure 2.2 to select a suitable fluid-fluid separating statepoint for the study of interface instabilities and wetting behaviour in the upcoming chapters. The concentrations of colloid and polymer solutions are given in terms of their volume fraction $\phi_c = \frac{4}{3}\pi R_c^3 n_c$ and $\phi_p = \frac{4}{3}\pi R_g^3 n_p$, where n_c and n_p are the number densities of colloids and polymers, respectively. In theory, the form of the phase diagram stems from the polymer-colloid size ratio; for $R_g/R_c \leqslant 0.3$, fluid-crystal phase coexistence might be observed, whereas for $R_g/R_c \geqslant 0.3$ the phase diagram is showing both fluid-crystal and gas-liquid-crystal phase coexistence [30, 34, 74]. However, in our case with $R_g/R_c = 2.5$, only gas-liquid phase coexistence was observed, and the system gelled at too high concentrations. The fluid-crystal coexistence was possibly suppressed by the polydispersity of the system; the polydispersity delays the onset of fluid-crystal coexistence and favours the gas-liquid separation, as has been theoretically predicted in [75–79]. At very low concentrations, no phase separation is observed. The full black line represents the approximate location of the binodal separating the one- and two-phase regions. The phase separation was reversible and reproducible for all samples. When a phase separated sample was shaken, a homogeneous solution was obtained, and after about 5–10 minutes the macroscopic interface was formed again. Furthermore, no sign of polymer adsorption was observed at any statepoints explored, showing that xanthan does not adsorb at PMMA. Also, xanthan is a very

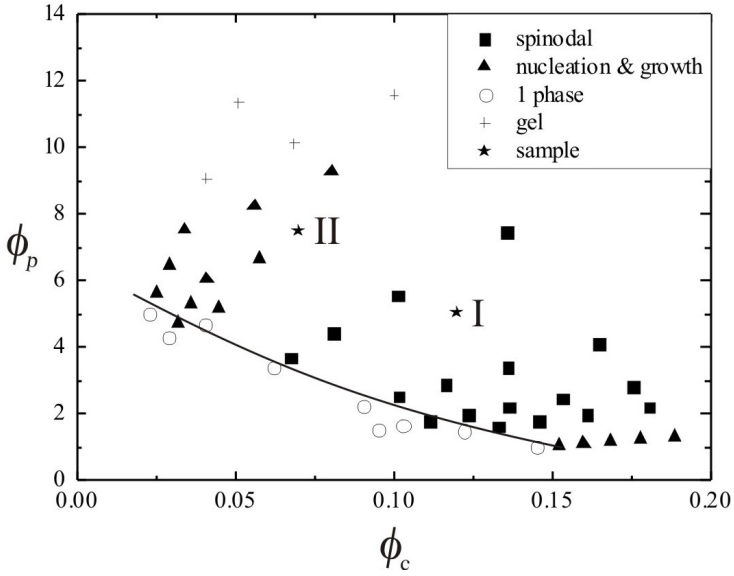


Figure 2.2: Phase diagram of PMMA-xanthan-water system [68, 73]. The full black line represents the approximate position of the binodal. The symbols in the two phases region show a different mechanism of the phase separation process at an early stage via spinodal decomposition (filled squares) and nucleation and growth (filled triangles). At very high colloid and polymer concentrations, the system gels (pluses). The stars indicate statepoint which will be prepared repeatedly throughout this thesis.

effective depletion agent because it can induce a phase separation already at low concentrations. This is similar to the observations made in [71], although a different colloidal particle was used, yet with identical polymers.

We used laser scanning confocal microscopy (LSCM) to follow real-space and -time evolution of the phase separating mixtures. This technique gives clear images, as shown in figure 2.3. In all images, the bright phase is the colloid-rich (liquid) phase and the darker phase is the colloid-poor (gas) phase; note that the microscope only records the fluorescence of excited dye within the colloids. The phase separation process can roughly be divided into three stages [80–83]. At an early stage, the system separates through spinodal decomposition (image 1). The interface then coarsens in time (image 2), where the droplets were seen coarsening through coalescence and diffusion, as first suggested in [84]. The coarsening step was followed by gravity-driven collapse and flow of the network, where the heavier liquid phase sedimented downwards with the lighter gas phase going upwards (image 3). Finally, a sharp macroscopic interface is formed (image 4), although it takes up to several hours before most of the drops completely coalesced with their bulk phases.

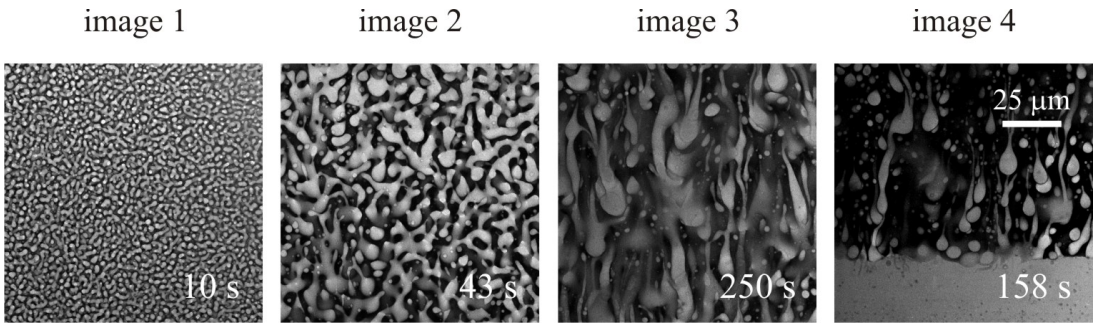


Figure 2.3: Phase separation process of PMMA-xanthan-water system which proceeded via spinodal decomposition.

The resulting interface between separated phases of the colloid-polymer mixtures is rough; the interface is corrugated by thermal capillary waves, which is driven by the thermal energy k_BT. Using the LSCM enables resolving the details of the fluctuations of the interface. Next in section 2.3, we will discuss a method to quantify the fluctuations using capillary wave theory, which directly leads to the determination of various interfacial parameters of the system, for example, the capillary length L_c, the interfacial tension γ, and the capillary time τ. These parameters are of central importance to the phenomena of interfacial instabilities and wetting.

Finally, in figure 2.4 (a) we show that our colloid-polymer system is compatible with microfluidic channels fabricated in PDMS. Our sample shows a complete wetting behaviour through the presence of thick wetting layers of the colloidal liquid phase on the walls, which results in a concave meniscus of the interface. This phenomenon is a consequence of the depletion interactions (figure 2.4 (b)); due to a strong attraction between colloidal particles and the wall (indicated as the blue crossed area), the colloidal liquid phase favours the wall, thus wetting the wall completely [49, 85]. Note that the fluctuations of the interface are clearly visible. In the upcoming chapters, we will show the consequences of the complete wetting and the large thermal interface roughness display by our system in studying the flow instabilities phenomena in confined channels.

2.3 Analysis of thermal capillary waves

In order to study the capillary wave fluctuations at the interface, we will discuss three main results, namely the interfacial roughness, the static and the dynamic correlation functions.

A sample at statepoint $\phi_c = 0.12$ and $\phi_p = 5.08$ (point I in figure 2.2) was prepared. The

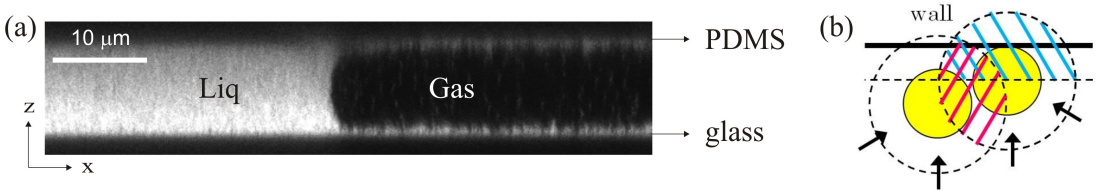


Figure 2.4: (a) LSCM snapshot of our PMMA-xanthan-water sample in a PDMS microfluidic channel where the colloidal liquid phase completely wets the walls. Note that the fluctuations of the interface are clearly visible. (b) Schematic interactions of two colloids near a flat, hard wall [49, 85]. Crossed areas indicate the overlap volume between colloid-colloid (red) and colloid-wall (blue).

sample at this statepoint is prepared repeatedly throughout this thesis. Here, the demixing proceeded via spinodal decomposition. The sample was sealed in a glass capillary of dimensions 2 mm x 10 mm x 0.2 mm (Vitrotubes P/N 5010), such that the system is not confined, and was allowed to phase separate and equilibrate overnight. The interface fluctuations were recorded for 5,000 frames using LSCM. Figure 2.5 shows examples of an (a) LSCM image and (b) schematic drawing of a free colloidal-liquid and -gas interface with thermal fluctuations. The upper phase is the colloidal gas phase and the lower phase is the colloidal liquid phase. To locate the position of the interface across the whole image, the intensity profile of the pixels along each column was fitted with a tangent hyperbolic function [11, 44, 86] (see figure 2.5 (c)). The located interface is represented by white dots in the image (a). This step provides initial data to analyse the fluctuations of the interface.

We may then construct the height correlation function g_h of the fluctuations by using a similar method described in [11, 44]. In general, the correlation function may be defined as:

$$g_h(x,t) = \langle [h(x',t') - \bar{h}(t')][h(x'+x,t'+t) - \bar{h}(t)] \rangle, \tag{2.1}$$

where $\langle \cdots \rangle$ denote averages over primed quantities, x is the coordinate along the interface, and t is the time. For each frame the height h is defined with respect to the average height at that time $\bar{h}(t)$, such that any systematic drift in the sample positioning is eliminated.

From the theory of capillary waves, first derived by Mandelstam in 1913 [4], each Fourier mode with wave vector $\mathbf{q}$ has a mean square amplitude given by:

$$\langle |h_{\mathbf{q}}|^2 \rangle = \frac{k_B T}{\gamma L^2} \frac{1}{q^2 + L_c^{-2}}. \tag{2.2}$$

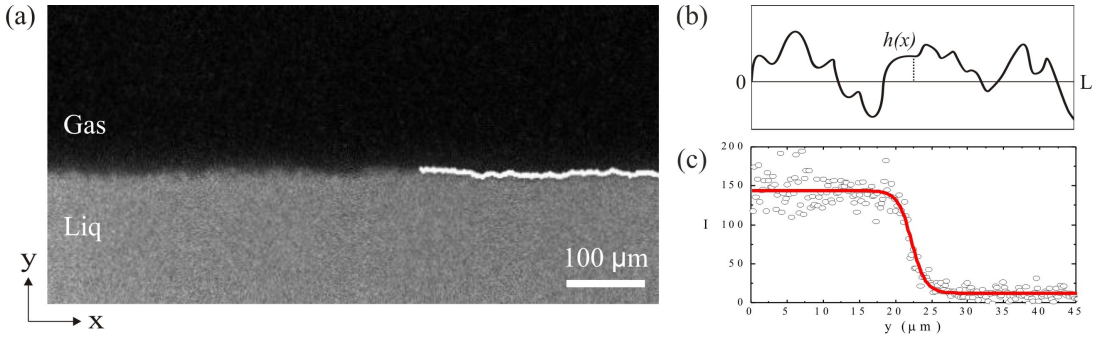


Figure 2.5: (a) LSCM snapshot of capillary waves at the interface in a phase separated PMMA-xanthan-water system. The lower phase is the colloidal liquid phase and the upper phase is the colloidal gas phase. The position of the interface is indicated with white dots. (b) Schematic depiction of the interface profile $h(x)$ over a length L. (c) Fitting the intensity profile of a column of pixels with a tanh function.

Here, $\langle \cdots \rangle$ denote a thermal average, k_B is the Boltzmann constant, T is the absolute temperature, γ is the interfacial tension between two fluids, q is the absolute value of the wave vector $\mathbf{q}$, and L_c is the capillary length given by:

$$L_c = \sqrt{\frac{\gamma}{\Delta\rho g}}, \tag{2.3}$$

where $\Delta\rho$ is the mass density difference between the two fluids and g is Earth's acceleration. Firstly, from equation (2.2), and by converting the sum to an integral over all q values:

$$\sum_{\mathbf{q}} \langle |h_{\mathbf{q}}|^2 \rangle \rightarrow \left(\frac{L}{2\pi}\right)^2 \int_{q_{min}}^{q_{max}} \langle |h_{\mathbf{q}}|^2 \rangle \, d\mathbf{q} \tag{2.4}$$

the mean square roughness of the interface is found to be:

$$\langle h^2 \rangle = \frac{k_B T}{4\pi\gamma} \ln\left(\frac{q_{max}^2 + L_c^{-2}}{q_{min}^2 + L_c^{-2}}\right). \tag{2.5}$$

Here, $q_{min} = 2\pi/L$ and $q_{max} = 2\pi/l$. L is related to the system size and l is a microscopic length which can, e.g. be interpreted as the size of the colloids [5]. Thus, the interfacial roughness $L_T = \sqrt{\langle h^2 \rangle}$ is proportional to $\sqrt{k_B T/\gamma}$. Furthermore, the interface heights are distributed according to the Gaussian:

$$P(h) = \frac{\exp(-h^2/2\sigma^2)}{(2\pi\sigma^2)^{1/2}} \tag{2.6}$$

with its variance σ^2 being given by equation (2.5). In figure 2.6 (a), we plot the height distri-

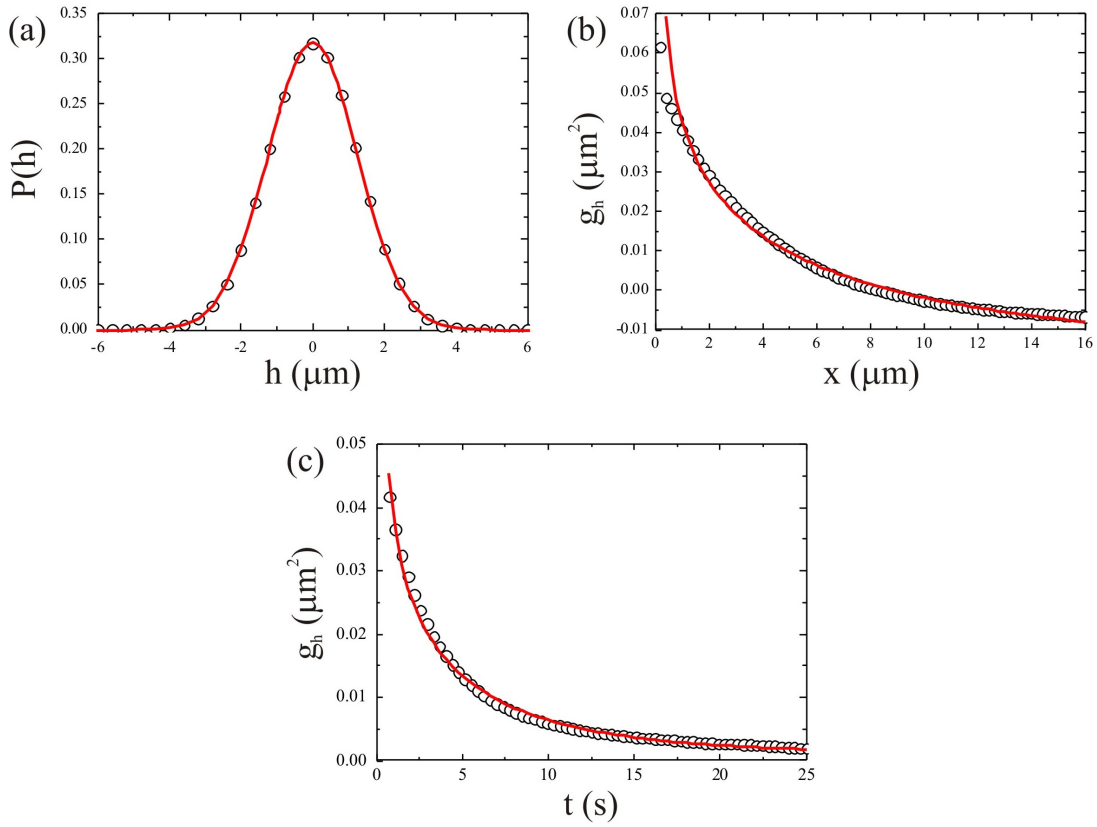


Figure 2.6: (a) Height distribution, (b) static and (c) dynamic correlation functions of the interface fluctuations of the PMMA-xanthan-water system. The open circles represent the experimental data. The full line curves represent the fit from (a) Gaussian and capillary wave theory for (b) static and (c) dynamic correlation functions.

bution of our fluctuations relative to the average interface position in each image (open circles), which shows that the interface roughness is Gaussian (full line), as expected [10,87]. The width of the distribution reflects the roughness of the interface.

Secondly, we look at the static correlation function. By Fourier transforming equation (2.2), the static correlation function can be derived as [4,10,88–90]:

$$g_h(x,0) = \frac{k_B T}{2\pi\gamma} K_0\Big(\frac{x}{L_c}\Big), \tag{2.7}$$

where K_0 is the modified Bessel function of the second kind. This real space expression for the spatial correlation function contains physical fitting parameters of the interfacial tension γ and capillary length L_c with an additional constant parameter included to account for any baseline offset (a term which is usually small). In figure 2.6 (b) we show results for the static correlation function $g_h(x, t = 0)$. The open circles represent the experimental data and the full

line curve represents the fit from capillary wave theory (equation (2.7)). Comparing the data to the theoretical correlation function produces a very good fit, although there is a clear deviation for $x \to 0$. Much debate is ongoing in understanding the behaviour of the interface and its interfacial tension at these short wavelengths (see, for example, [8,91–93]). The fitting yields an interfacial tension of 30 x 10^{-9} N/m and a capillary length of 14 μm — values of a similar order of magnitude in comparison with those observed in previous experiments [10, 44, 86].

Thirdly, we may derive the dynamic correlation function. Theoretically, in the overdamped regime, each mode decays exponentially as $\exp[-t/2\tau_q]$ with the dispersion relation [52]:

$$\omega_q = \frac{\gamma}{2\eta L_c}(\bar{q} + (\bar{q})^{-1}) = \frac{\bar{q} + (\bar{q})^{-1}}{2\tau} \tag{2.8}$$

with $\eta = \eta_L + \eta_G$ being the sum of viscosities of both phases, $\bar{q} = qL_c$ and the capillary time τ given by the expression:

$$\tau = \frac{\eta L_c}{\gamma}. \tag{2.9}$$

By Fourier transforming equation (2.2), and now by introducing the damping factor, one obtains the dynamical correlation function as [10, 88, 90]:

$$g_h(0,t) = \frac{k_B T}{(2\pi)^2 \gamma} \int_{\bar{q}_{min}}^{\bar{q}_{max}} d\bar{q} \frac{\bar{q}}{1+\bar{q}^2}\, e^{-\omega_q t} = \frac{k_B T}{2\pi\gamma} K_0\Big(\frac{t}{\tau}\Big). \tag{2.10}$$

Note that the integral limits can be set to $q_{min} = 0$, since the length of the system is much greater than the capillary length ($L \gg L_c$), and $q_{max} = \infty$, since the particles are significantly smaller in size than the capillary length ($l \ll L_c$). Also, for a concise review of derivation of the Bessel function, see [94]. In figure 2.6 (c), we show experimental results for $g_h(x = 0, t)$ (open circles) and their fit to the theoretical expression (equation (2.10)) (full line curve). The agreement between the theoretical fit and the experiments is even better than in the static case. Similar to the static case, this function contains the interfacial tension γ and the capillary time τ as physical fitting parameters and an additional constant parameter to compensate for any baseline offset. From the fitting, we obtain an interfacial tension of 49 x 10^{-9} N/m and capillary time of 10 s, again comparable to those obtained in previous experiments [10, 44, 86].

Moreover, the relation of these equilibrium quantities through equation (2.9) allows for an independent check of the consistency of our measurements. For example, from the interfacial

tensions, capillary length and capillary time obtained from height correlation functions, we obtained a value of 21 mPa s for the combined viscosities of the colloidal phases, which is reasonable with our rheological measurements explained below ($\eta_L + \eta_G = 22$ mPa s).

2.4 Experimental techniques

2.4.1 Rheology

Rheology is the science of the deformation and flow of matter, a term first invented by E. C. Bingham, Professor at Lafayette College, in 1920 [95]. The deformation of material when subjected to constant stress characterises its rheological behaviour; the material is Newtonian when its deformation is proportional to the applied stress, whereas when the deformation is non-linear, the material is said to be viscoelastic. In particular, the material is shear thinning when the viscosity decreases, or shear thickening when the viscosity increases with the rate of stress. This is common in complex fluid, e.g. polymer suspension. Moreover, at low shear rates most materials have a zero shear viscosity (standing viscosity) where deformation does not effect change in the structure. Using a rheometer, a number of measurements can be made to determine a materials rheological behaviour under stress.

In this thesis, the rheological measurements were performed using a TA AR-G2 rheometer with a cone-plate 1°/60 mm geometry and a truncation gap of 34 μm. The cone was attached to a magnetic air bearing, which rotates with low resistance to apply a uniform shear rate. Figure 2.7 shows the rheometer and geometry set-up. A PMMA-xanthan mixture at the same statepoint as above was prepared and allowed to completely phase separate overnight. The separated phases with a 1:2 liquid-to-gas volume ratio were then carefully isolated and a rheological characterisation of each phase was performed. All of the measurements have been performed with a solvent trap to prevent evaporation of the solvent.

(i) Steady shear experiments

Figure 2.8 (a) shows steady shear flow curves for colloidal-liquid and -gas phases at a shear rate $\dot{\gamma}$ range from 0.1 to 100 s^{-1}. No hysteresis was observed for both phases. For the colloidal liquid phase (filled squares) the viscosity depends only slightly on the shear rate. The viscosity follows

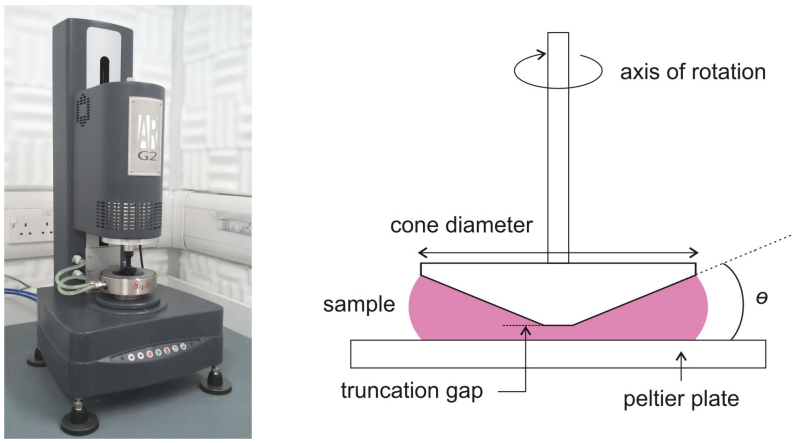


Figure 2.7: (left) TA AR-G2 rheometer and (right) schematic set-up of cone and plate geometry used for measurements.

a power-law dependence (red line):

$$\eta \propto \dot{\gamma}^m \tag{2.11}$$

where the index m determines the types of fluid (i.e. $m = 1$ in Newtonian behaviour, $m > 1$ increasing the shear thickening behaviour and $m < 1$ increasing the shear thinning behaviour). Here, we found $m = 0.97$, showing a small deviation from Newtonian behaviour. The viscosity of the colloidal gas phase, however, decreases with an increasing shear rate (filled circles). The non-Newtonian character of the colloidal gas was analysed with the well-known Cross model (blue line), which is of the form [96]:

$$\eta = \eta_\infty + \frac{\eta_0 - \eta_\infty}{1 + (k\dot{\gamma})^m} \tag{2.12}$$

where η_0 and η_∞ are the viscosities at a zero and infinite shear rate, respectively. The constant k is the structural relaxation time and its reciprocal $1/k$ gives a critical shear rate $\dot{\gamma}_c$, indicating the onset of shear thinning. Here, we found $\dot{\gamma}_c = 33$ s^{-1}, which is reasonably consistent with previous experimental findings [72] where a similar polymer was used. This is expected as adding colloids naturally slows down the dynamics of the dissolved polymer. In the shear thinning region ($\dot{\gamma} > \dot{\gamma}_c$), the flow curve exhibits a power-law behaviour $\eta \propto \dot{\gamma}_c^m$, which is typical of semidilute polymer solutions, with a shear thinning index $m = 0.60$. Furthermore, the low-shear viscosity determined by extrapolating the flow curves to $\dot{\gamma} = 0$ s^{-1} gives $\eta_L = 7$ mPa s for the colloidal liquid and $\eta_G = 15$ mPa s for colloidal gas phases, respectively.

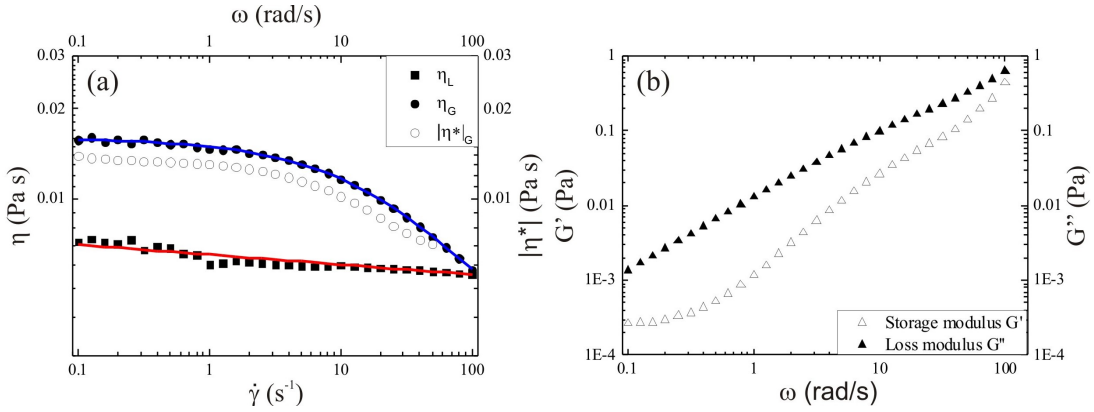


Figure 2.8: Rheological measurements on colloidal-gas and -liquid phases. (a) Apparent viscosity $\eta(\dot{\gamma})$ vs shear rate $\dot{\gamma}$ for both phases (filled symbols), and complex viscosity $|\eta^*|(\omega)$ vs radial frequency ω for the colloidal gas phase (open symbols). (b) Storage modulus G' (open symbols) and loss modulus G'' (closed symbols) of the colloidal gas phase as a function of the radial frequency ω.

(ii) Oscillatory shear experiments

The measurements were performed at frequencies ω ranging from 0.1 to 100 rad s^{-1} with a constant strain $\sigma = 0.5$, such that the measurements remain in the linear viscoelastic regime. Figure 2.8 (b) shows the elastic component, storage modulus $G^{'}$ and the viscous component, loss modulus $G^{''}$ as a function of applied frequencies ω for the colloidal gas phase. At low angular frequencies, $G^{''} > G^{'}$, showing that the phase behaves predominantly viscous. The loss modulus follows the scaling $G^{''} \propto \omega$ characteristic of Newtonian polymeric solutions. At critical frequency ω_c, a cross-over from liquid to solid-like behaviour is observed, which was estimated to be at ~ 100 rad/s. The reciprocal of the cross-over frequency leads to a characteristic relaxation time $\tau_c = 1/\omega_c$, which corresponds to the lifetime of the entanglements. Finally, at higher frequencies, we expect that the phase being predominantly elastic with $G^{'} > G^{''}$.

In addition, according to the empirical Cox-Merz theory [97], the frequency dependence of the absolute magnitude of the complex viscosity $|\eta^*|(\omega)$ (open circles in figure 2.8 (a)) can be defined as

$$|\eta^*| = \frac{\sqrt{(G')^2 + (G'')^2}}{\omega}. \tag{2.13}$$

Comparing to the shear rate dependence of the steady shear viscosity $\eta(\dot{\gamma})$, a small disagreement was observed, which suggest that the xanthan chains may be connected by crosslinks formed by

physical bonds, forming a weak gel-like structure.

2.4.2 Fabrication of microfluidic devices

Throughout the chapters that follow, the microfluidic channels used to study the colloidal interface flow behaviour were created by a soft-lithography technique with polydimethylsiloxane (PDMS) elastomer. The soft-lithography technique was first introduced by G. M. Whitesides *et al.* [98–100], offering an inexpensive, simple and flexible technique to fabricate a variety of channel patterns at the scale of nano- and micrometres [101,102]. For a brief review of this technique, see [103]. The fabrication of nano/microstructures is increasingly important nowadays as components for many "lab-on-a-chip" applications which resulted in a reduction of reagent volume, sample size, time, cost and power consumption, yet an improvement in detection limits and product analysis [64,104–107]. In addition, the outstanding optical properties of the PDMS elastomer are a perfect match for optical microscopy techniques.

The processes involved to fabricate microfluidic devices are schematically shown in figure 2.9 (a). Firstly, a silicon wafer surface was constructed with a positive or negative pattern of SU-8 photoresist (Chestech) using photolithography. The SU-8 polymer was spin-coated onto the wafer, followed by a soft baking step in order to remove the solvent and improve the resist-substrate adhesion. The baking was typically performed by heating the SU-8 film up to 95°C on a flat-levelled hotplate. Lower temperatures or short time baking leave resist film with a high solvent content, which will evaporate and, therefore, generate high film stress during post-exposure baking. Then, the wafer was irradiated by UV light through a photomask to polymerise the SU-8 in the desired pattern, followed by a post-baking step to increase the cross-linking process and stabilise it against the action of solvents during the post-development step. A development step is performed by immersing the wafer in a suitable solvent at room temperature to remove the excess unpolymerised SU-8. The wafer is subsequently rinsed with isopropanol. Finally, to cure the resist pattern on the substrate, a hard baking step at temperatures between 150°C and 200°C was performed. The actual spin coating conditions and processing times for baking, UV irradiation and development are dependent on the film thickness and the properties of the SU-8 used [108,109].

The constructed wafer is used as a master for fabrication with PDMS elastomer, creating a polymeric mold with the channel pattern imprint. A single master can be used to generate

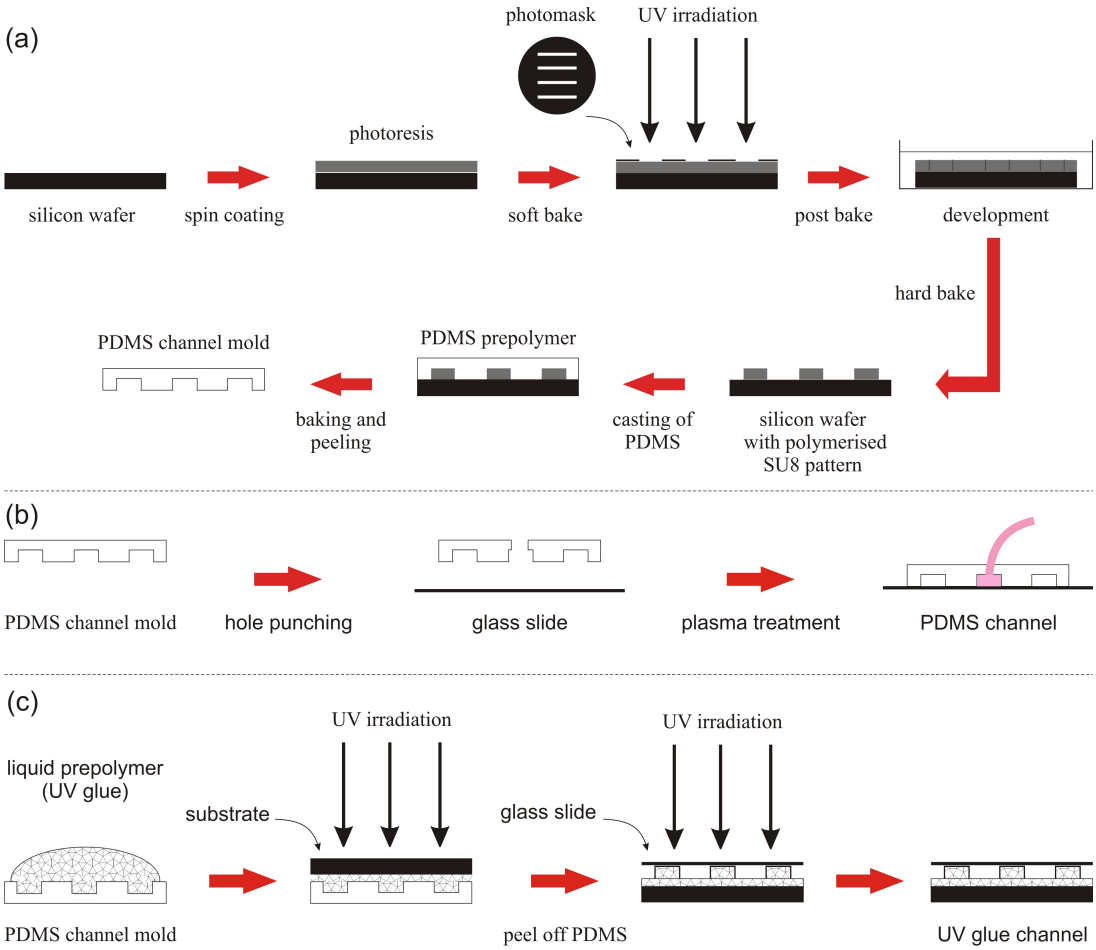


Figure 2.9: Schematic procedure of the process involved in fabrication of microfluidic devices. (a) A silicon master with polymerised SU-8 structures was first constructed by photolithography. Then, a polymeric mold was made by curing a prepolymer of PDMS onto the master; its surface replicates the relief structures on the surface of the master. The channel could then be made of (b) PDMS or (c) UV glue.

multiple copies of the PDMS mold without reducing the quality of the structures. Here, PDMS (Sylgard^{TM} 184) was obtained from Dow Corning. The PDMS prepolymer liquid was prepared by mixing the silicon elastomer and curing agent in a ratio of 10:1, poured onto the master and heated at 85°C for 1 hour. Once solidified, the PDMS layer was separated from the master. The channel could then be made out of this PDMS mold. Holes were made in the elastomer to allow the channel to be filled by tubes. The PDMS channel was finally sealed with a glass slide by modifying both the PDMS and glass surfaces to their hydrophilic form with oxygen plasma treatment, allowing them to be bonded together permanently. The steps involved are illustrated in figure 2.9 (b). This enables us to flow the colloid-polymer system in the channels at desired dimensions, and view its interfacial behaviour through the glass window.

Alternatively, the PDMS mold was used to produce channels of a UV glue (Norland optical adhesive 81) (see figure 2.9 (c)). The use of an elastomeric (rather than a rigid) mold to transfer the microstructure pattern onto a substrate enormously increased the ease of separating the mold and the substrate and protected the fragile structures during separation. A thin layer of liquid prepolymer was applied to the patterned surface of the PDMS mold and then placed in contact with a substrate. The prepolymer was cured to a solid by illuminating with UV light. When the PDMS mold was peeled away carefully, a channel pattern was left on the surface of the substrate. A glass coverslip was placed on top of the channel and irradiated with UV light again. The channels were designed so that they remained open and may be filled by capillary action. To increase the surface hydrophilicity, the channel was treated with oxygen plasma for several minutes. The channel was finally sealed with UV glue, which enables us to study wetting behaviour on walls.

2.4.3 Confocal microscopy

To study fluid-fluid interfacial instabilities and wetting behaviour of colloidal system we used a Zeiss Exciter LSM 5 laser scanning confocal microscopy. Our instrument was fitted with a rolling table (see figure 2.10), so that it can be placed in a way that the sample can be viewed in the plane perpendicular (left) or parallel (right) to gravity.

Optical microscopy is an essential technique to obtain real-space and -time information about complex mechanisms in soft matter physics, such as in complex fluids and colloidal dispersions, at length scales of the order of the wavelength of visible light [110,111]. In conventional (transmission light) microscopies, fluorescent light emitted by the sample often happens through the whole excited volume. Thus, visualisation of optically dense samples, such as a colloidal suspension, can be made difficult as the light undergoes many scattering events as it passes through the suspension. This tends to overwhelm details in the actual image plane and cause blurriness of the image.

In contrast, confocal microscopy provides high-quality images with improved contrast and resolution. The basic keys of the confocal approach are: (i) rejection of an out-of-focus signal using a special pinhole in front of the detector and (ii) point-by-point illumination of the sample to minimise scattered emission that occurs at points above and below the objective focal plane. This principle was originally invented by Marvin Minsky in the mid-1950s when he wanted to

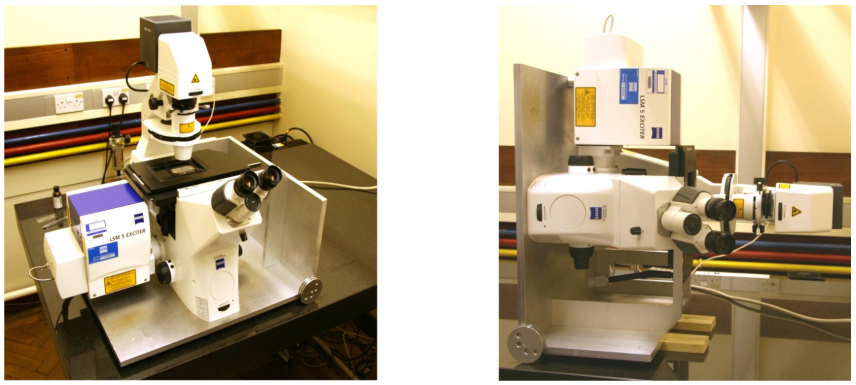


Figure 2.10: Zeiss Confocal Microscope in the position of (left) perpendicular and (right) parallel to gravity.

study neural networks in unstained preparations of living brains at Harvard University [112]. A schematic set-up of the confocal microscope is shown in figure 2.11 (a) [113, 114]. Light from a point source passes through a pinhole to create a sufficiently thin laser beam. The light is directed by a dichroic mirror and focused by the objective lens into the focal plane within the fluorescently labelled sample. The emission light from that spot on the sample passes back through the collector lens and is detected by, e.g. a photomultiplier tube. The objective and collector lens are usually identical. The detector pinhole is placed in the conjugate focal plane — hence the term *confocal microscopy* — filtering out background light arriving from the sample. The laser scans across the focal plane and allows us to build up a complete 2D image. A 3D image of the sample can be performed by combining a series of such slices at different depths, that is, by changing the height of the focal plane. The introduction of the laser as a light source improves the ability of 3D imaging; strong illumination is required to obtain a reasonable signal at a large focal depth. This 3D capability is one of the main advantages of confocal microscopy.

To further quantify how the contrast and resolution are improved when utilising the confocal microscope, we may study the point spread function (PSF) where we follow the review of [113, 115, 116]. The PSF $p(\rho, \xi)$ is defined as the probability that photons will reach the point ρ (in the focal plane) and ξ (along the optical axis) or that photons will be received from that point. The corresponding PSF function is given by:

$$p(\rho, 0) = \left(\frac{2J_1(\rho)}{\rho} \right)^4 \qquad \text{PSF for a point in the focal plane} \qquad (2.14)$$

$$p(0, \xi) = \left(\frac{\sin(\xi/4)}{\xi/4} \right)^4 \qquad \text{PSF for a point along the optical axis} \qquad (2.15)$$

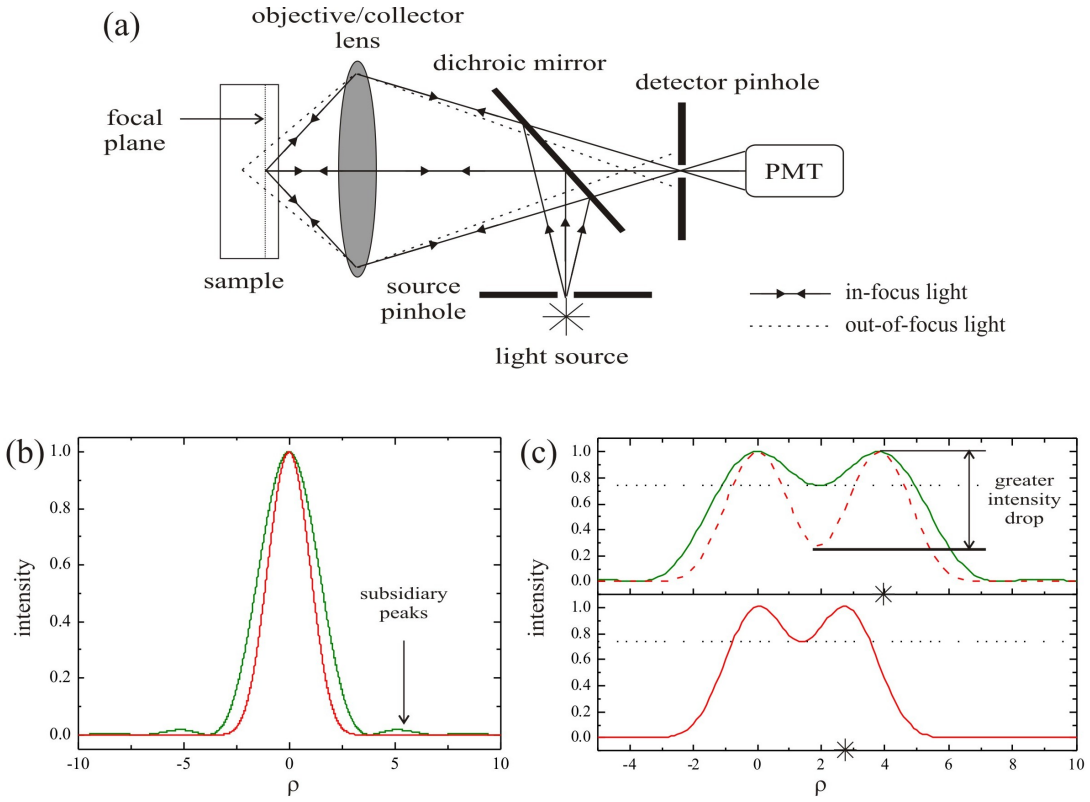


Figure 2.11: (a) Schematic diagram of the optics of a confocal microscope [113, 114]. (b) Comparison of radial PSFs of conventional microscopy (green) and confocal microscopy (red). (c) PSF intensity profile of two similar point sources for conventional microscopy (green) and confocal microscopy (red). The stars at the horizontal axis denote the Rayleigh distance. The top-dashed/red curve shows a much greater intensity drop, which meant improved contrast in confocal microscopy. The bottom-full/red curve fulfills the exactly confocal Rayleigh criterion (i.e. the horizontal line) at smaller separation, leading to an improved resolution. Similar trends are observed for PSF along the optical axis.

where J_1 is the Bessel function of the first kind. Note that both equations are the square of the conventional PSFs as the light in the confocal microscope passes through the same objective twice. The optical point ρ and ξ can be related to the real distances r and z by:

$$\rho = r(2\pi NA/\lambda) \tag{2.16}$$

$$\xi = z(2\pi NA^2/n\lambda) \tag{2.17}$$

where λ is the wavelength of the light, n the refractive index of the medium, and NA the numerical aperture of the objective. NA is defined as $NA = n\sin\alpha$, with α being the half angle of the maximum cone of light that can enter or exit the objective. Figure 2.11 (b) shows the

PSFs of conventional (green) and confocal (red) microscopy in the focal plane (equation (2.14)). The central peak is known as the Airy disk, with the distance to where the PSF first drops to zero ($p(\rho_{airy}, 0)) = 0$ being given by the radius of the Airy disk, of which the size depends on the wavelength of the laser light and the numerical aperture of the objective lens. Comparing the PSFs reveals that the width of the PSF and the subsidiary peaks for confocal microscopy decreases significantly compared to the case of conventional microscopy. Thus, in confocal microscopy, each point can be imaged with a greater resolution as more light is contained in the central peak and due to the narrow intensity distribution of the PSF.

If two objects of equal intensity are positioned at a certain distance, the resulting image is then composed by the sum of the two Airy disks. The capability of distinguishing the two objects is thus directly related to the microscope resolution. Such resolution measurement is given by the Rayleigh criterion; the two points are resolved if the drop in intensity between maxima is 26% [110]. The Rayleigh criterion is illustrated in figure 2.11 (c), which shows the intensity profile of two point sources within the focal plane. For conventional microscopy (green curve) the Rayleigh distance (i.e. the star at the horizontal axis) is exactly the radius of the Airy disk. However, in confocal microscopy (bottom-full/red curve), the Rayleigh distance decreases by a factor of 1.4 due to increased resolution. Moreover, if two points separated by the conventional Rayleigh distance are imaged in a confocal system, a much greater intensity drop was observed (top-dashed/red curve). This clearly demonstrates the improved contrast in confocal microscopy. Similar trends are observed for the PSF along the optical axis.

The ability of microscopy to capture images at high speed is also crucial for us to study the instability dynamics and the thermal fluctuating interface of our systems. Most commonly, galvanometers are used to move the internal mirrors back and forth in a saw-tooth pattern to scan over the entire sample plane [115], although an enormous increase in scanning speed may be obtained by employing a rotating Nipkow disk [110]. Our LSCM set-up allows for capturing images with a maximal rate of about three frames (512 x 512 pixels) per second.

2.5 Conclusion

As will become clear throughout this thesis, the development of our new colloid-polymer system dispersed in water brings many advantages. Its interfacial tension is ultralow and the thermal roughness is therefore large, allowing us to directly observe the thermal capillary wave fluctuations on the free interface. We have shown that the fluctuating fluid-fluid interface can be seen directly in real space with a resolution close to the particle size using confocal microscopy. We demonstrated the application of a capillary wave analysis to this system and obtained interfacial properties in line with previous work. This system will prove to be very useful in the investigation of hydrodynamic effects, such as the fingering instability and droplet emission. In addition, this system allows studying wetting phenomena at geometrically sculpted walls. As techniques, we outline the use of a TA AR-G2 rheometer to determine the rheological properties of the separated colloidal phases under stress. We have also outlined a simple method to fabricate microfluidic cells, and the use of a confocal microscope to image the behaviour of the colloid-polymer systems in full three dimensions in real space.

Appendix: Physical properties of the PMMA-xanthan mixtures

Table 2.1: Summary of the physical properties of the PMMA-xanthan mixtures. The interfacial tension γ, capillary length L_c, interfacial roughness L_T, capillary time τ, and density difference of the two colloidal phases $\Delta\rho$ were obtained from the capillary wave spectrum. A rheological characterisation was performed on a TA AR-G2 rheometer.

			PMMA	xanthan	water	Point I	Point II
radius	R	(nm)	110	264			
density	ρ	(g/mL)	1.17		0.99		
molecular weight	M_w	(kg/mol)		4000			
refractive index	n		1.49		1.33		
statepoint	ϕ_c					0.12	0.07
	ϕ_p					5.08	7.50
interfacial tension	γ	(nN/m)				30	50
capillary length	L_c	(μm)				14	52
interface roughness	L_T	(μm)				1.2	1.4
capillary time	τ	(s)				10	10
density difference	$\Delta\rho$	(kg/m^3)				15	1.9
viscosity - liquid phase	η_L	(mPa s)				7	
viscosity - gas phase	η_G	(mPa s)				15	

Chapter 3

The Saffman-Taylor instability

ABSTRACT

A concise review of the Saffman-Taylor instability is presented, starting with the original work by Saffman and Taylor. This is followed by a discussion of an extension of their two-dimensional theory, dealing with the role of surface tension and the three-dimensional nature of the viscous fingering. We further introduce the colloidal system as our model to explore the Saffman-Taylor instability, including its advantages.

3.1 Introduction

> "It has been pointed out (Taylor 1950) and verified experimentally (Lewis 1950) that when two superposed fluids of different densities and negligible viscosities are accelerated in a direction perpendicular to their interface, this surface is stable or unstable for small deviations according as the acceleration is directed from the more dense to the less dense fluid or vice versa." (Saffman & Taylor, 1958) [117]

Whenever a low viscosity fluid (fluid 1) displaces a high viscosity fluid (fluid 2) in a porous medium or Hele-Shaw cell (a very thin channel consisting of two flat plates), the interface is rendered unstable and viscous fingers develop, grow and compete (see figure 3.1 for a picture of the phenomenon). This instability was first studied experimentally and theoretically by Saffman and Taylor in 1958 [117]. Since then the viscous fingering instability has received much attention in the previous half century due to its relative simplicity in studying the motion of the fluid-fluid interface [51,118] and in understanding the general problem of a pattern formation in non-linear systems [119–124]. Recently, developments on the dynamics of fingering patterns have witnessed a renewed interest, for example, in the role of viscoelastic effects [125], the importance of three-dimensional phenomena [126], possible stabilisation mechanisms through channel geometries [127], and as a means of providing efficient mixing in microfluidics channels [128]. The classic zero-surface-tension limit also continues to inspire experimental studies, for example on granular matter [123] where, instead of rounded fingers, a fractal structure with sharp cusps develops.

Moreover, the viscous fingering is of central importance to a number of technological processes, most arguably in enhanced oil recovery, in which gas or water is injected into the reservoir to mix with the oil and displace the oil to the surface [129–131]. Here, interfacial instabilities can be a serious problem if the displacing fluid has a lower viscosity than the oil, where oil cannot be displaced completely, but instead the displacing fluid penetrates the porous rock as a finger. On the other hand, viscous fingering can be beneficial to chromatographic separation [132] and can improve mixing in non-turbulence systems and microfluidic devices [128] by increasing the interfacial contact area. The fact that we depend on the ability to control the interface to remain stable or unstable makes the understanding of viscous fingering behaviour an active field of research in both fundamental and practical applications.

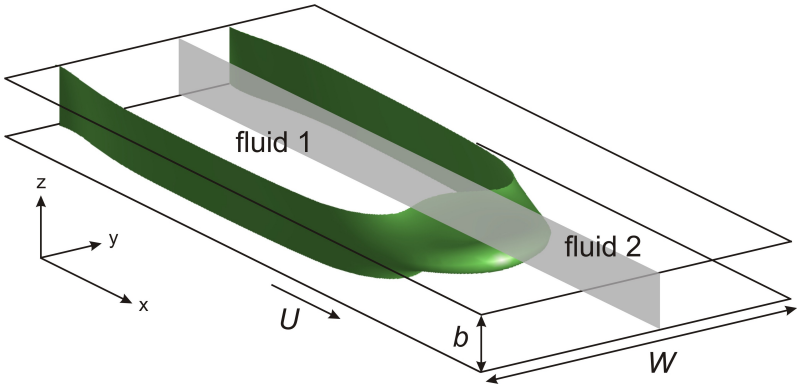


Figure 3.1: Schematic depiction of a computer-generated viscous finger in a Hele-Shaw geometry, with fluid 1 (low viscosity) displacing fluid 2 (high viscosity). Observations in the xy-plane correspond to the top view of the channel, while the xz-plane (grey plane) refers to the projections along the channel thickness direction.

In an effort to explore and understand the viscous fingering behaviour, here we use a colloidal system together with microfluidics and confocal microscopy techniques, which enables us to address the phenomena in the full three dimensions, at the scales down to the thermal fluctuations. To begin, in this chapter we give a review of the Saffman-Taylor problem. In the next chapters, details of our experimental set-up and results will be presented. Specifically, in chapter 4 we will discuss the observations in the xz-plane (grey plane in figure 3.1), where we make a cut through the finger as it develops. We will focus on the interfacial curvature along z. This will be followed by chapter 5 where fingering in the xy-plane, the wide dimension of the channel, is observed. Here, we will discuss the interplay between the curvature in the z-direction and the fingering in the xy-plane. In chapter 6, we study a related contact line instability, i.e. the intersection point between the fluid-fluid interface and the channel walls, which leads to periodic emission of droplets by exploiting the viscous fingering experiments in our microfluidics set-up.

This chapter is organised as follows. In section 3.2, we introduce the origin of the viscous fingering instability by Saffman and Taylor, followed by an extension of their two-dimensional theory, focusing on the role of surface tension (section 3.3) and the third dimension of the viscous finger (section 3.4). In section 3.5, we highlight the key advantage of using the colloidal system as a model fluid over molecular fluid in studying the viscous fingering instability. We end with a conclusion in section 3.6.

3.2 Origin of the Saffman-Taylor instability

The Saffman-Taylor instability refers to the interfacial instability between two fluids which leads to the formation of finger-like structures. Classic Saffman-Taylor experiments have been performed in a Hele-Shaw cell due to its simplicity and its well-characterised set-up. It also provides good visibility of the flow dynamics, in contrast to a porous medium. The Hele-Shaw cell with thickness b and width W provides a two-dimensional limiting framework where the velocity of the two fluids is averaged over the channel thickness and the interface is considered a line. Figure 3.2 (a) shows an example of the Saffman-Taylor experiments in a Hele-Shaw cell where air (upper fluid) is used to displace glycerine (lower fluid) [117]. The interface becomes unstable as it moves downwards (image 1), leading to the competitive growth of finger-like structures (image 2), and eventually a single dominant finger propagates over its neighbours (image 3). The onset of the instability in the Hele-Shaw cell (linear stability analysis) will be explained later in chapter 5.

The finger has a steady state shape (inset figure 3.2 (b)), measured as a relative finger width $\lambda_f = W_f/W$, as a function of the capillary number defined as $Ca = \eta U/\gamma$, which is the ratio of viscous forces to the surface tension forces. Here, W_f is the width of the advancing finger, U is the finger flow velocity, γ is interfacial tension of the system, and $\eta = \eta_2$ is viscosity of the more viscous fluid — the less viscous fluid, η_1 is considered inviscid. Experimentally, Saffman and Taylor showed that the finger width λ_f tends rapidly to an asymptotic value of $1/2$ as Ca increases (see figure 3.2 (b)).

Saffman and Taylor also solved the viscous fingering problem theoretically, in the absence of surface tension in the two-dimensional limit, and found that the shape of the finger can be described by [117]:

$$x' = \Big(\frac{1-\lambda_f}{\pi}\Big) \ln\Big[\frac{1}{2}\Big(1+\cos\frac{\pi y'}{\lambda_f}\Big)\Big], \tag{3.1}$$

where x', y' measure the distance from the finger tip in units of half the channel width W. Finger profiles evaluated using equation (3.1) are shown in figure 3.2 (c). A good agreement with the experimental finger profile was obtained as $\lambda_f \to 1/2$. At low Ca, when the effect of surface tension is important, the calculated shapes, however, differ substantially from the actual ones. Furthermore, the solution predicts a continuous family of the finger width λ_f at each velocity,

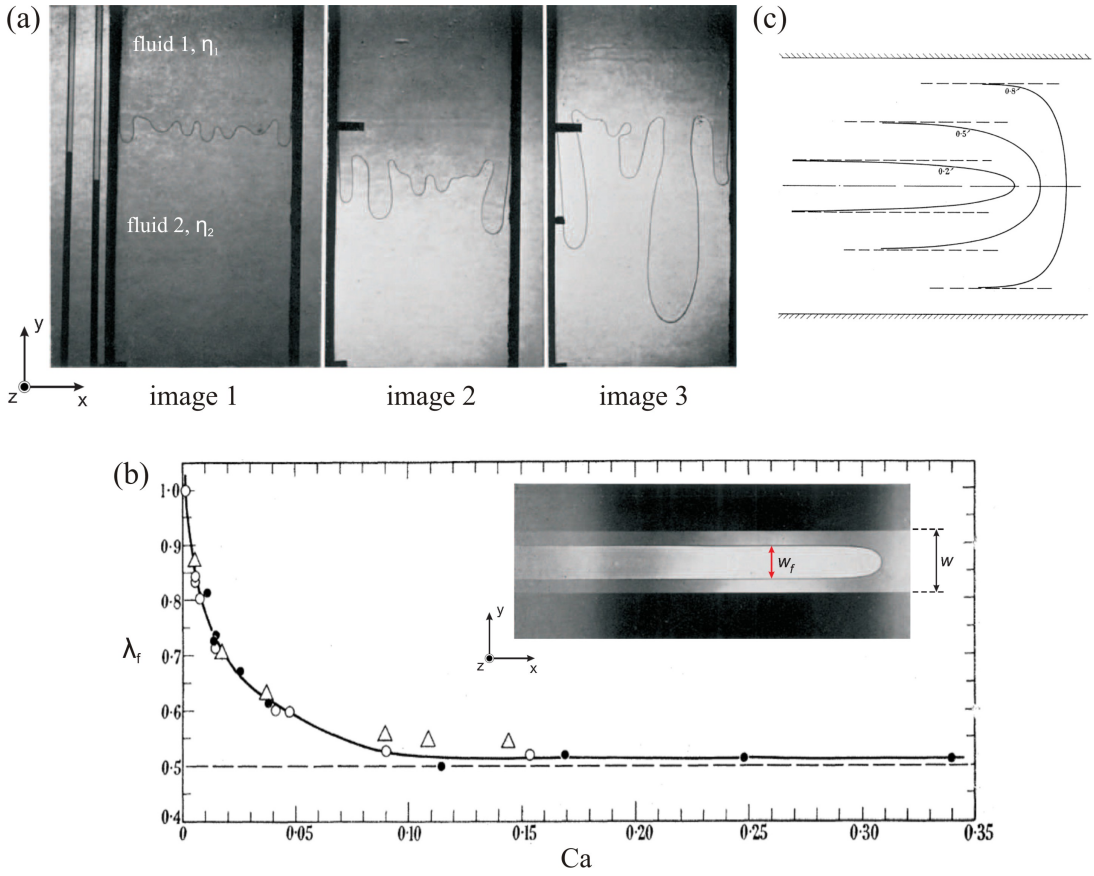


Figure 3.2: (a) Saffman-Taylor experiments in a Hele-Shaw cell where air (upper fluid) is used to displace glycerine (lower fluid). (b) Finger width λ_f versus Ca for systems of water penetrating into different oils (different symbols). Inset: A single finger at a steady state with width $\lambda_f = W_f/W$. (c) Shapes of the finger with $\lambda_f = 0.2$, 0.5 and 0.8 evaluated using equation (3.1). Figures are taken from [117].

which is in disagreement with experimental observations. This non-uniqueness of the solution meant that they were unable to predict the dependence of λ_f with the finger velocity U.

3.3 McLean-Saffman 2D predictions

In 1981, more than 20 years after the seminal paper of Saffman and Taylor, McLean and Saffman [133] included the effect of surface tension in a big step to solve the non-uniqueness of the Saffman-Taylor results. By solving the integral equation for the interface numerically in the two-dimensional limit, they were the first to show that there is an infinite family of solution for

the relative finger width λ_f which is governed by a dimensionless parameter defined as:

$$\frac{1}{B} = \frac{12}{\epsilon^2}\frac{\Delta\eta U}{\gamma} \tag{3.2}$$

where $\Delta\eta = \eta_1 - \eta_2$, the viscosity difference of the two fluids with $\eta_1 < \eta_2$ and $\epsilon = b/W$ accounts for the channel aspect ratio. Similar to previous studies, the numerical results of McLean and Saffman suggested that λ_f is a monotonically decreasing function of $1/B$ that saturates to $\lambda_f \to 1/2$ as $1/B \to \infty$. Further mathematical development also showed the precise role of the surface tension, which acts as a singular perturbation in the selection problem [134–136]. This observation initiates intense study in the viscous fingering instability, culminating in breakthroughs in theory and in experiments dealing with the role of surface tension [137, 138].

3.4 The 3^{rd} dimension

Experiments carried out by Tabeling and Libchaber [137] showed that introducing the McLean-Saffman control parameter [133] alone is not enough to fully describe the instability. As shown in figure 3.3 (a), the theoretical prediction disagreed with their experimental results. They argued that this is due to a thin layer of the more viscous fluid, which adhered to the walls and left behind the advancing finger, which changes the curvature of the interface and renders the problem three-dimensional.

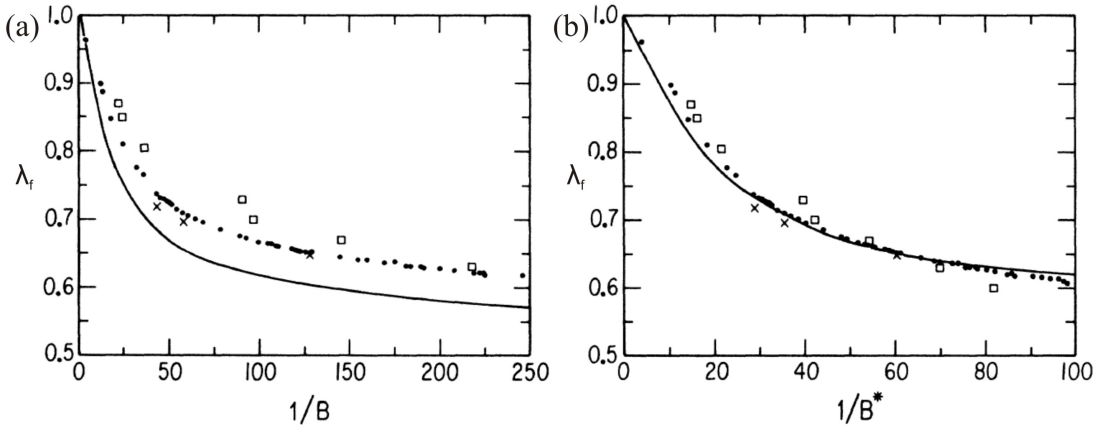


Figure 3.3: Finger width λ_f as a function of (a) 1/B and (b) rescaled control parameter $1/B^*$. Symbols denote experimental results of Saffman and Taylor (□) [117] and Tabeling and Lichaber (•, ×) [137]. The solid line describes the theoretical prediction of McLean and Saffman [133]. Figures are taken from [137].

In the McLean-Saffman prediction, the variation of the curvature in the z-direction is neglected and it is assumed that the curvature is constant with the motion of the finger which equals half of the channel gap. The interface is actually three-dimensional with two radii of curvature, one in the plane of the instability $R_{\parallel}$ (xy-plane) and one perpendicular to the plate $R_{\perp}$ (xz-plane). Thus, the pressure drop across the interface can be written as:

$$\Delta P = \gamma \left(\frac{1}{R_{\parallel}} + \frac{1}{R_{\perp}} \right) = \frac{\gamma}{R_{\parallel}} \Big(1 + \frac{R_{\parallel}}{R_{\perp}} \Big). \tag{3.3}$$

Firstly, if $1/R_{\parallel}$ is assumed to be much larger than $1/R_{\perp}$, the interface is expected to be flat in the z-direction, hence the system being two-dimensional and the pressure drop being simplified to $\Delta P = \gamma / R_{\parallel}$. However, given the fact that in most experiments, the displaced fluid wets the walls, then $R_{\perp} \ll R_{\parallel}$. For such cases, Tabeling and Lichaber have proposed that thin film effects can be captured by defining an effective surface tension, more clearly defined in [53, 126]:

$$\gamma^{*} = \gamma \Big(1 + \frac{R_{\parallel}}{R_{\perp}} \Big). \tag{3.4}$$

Experimentally, it turned out to be not possible to measure $R_{\perp}$. For this purpose, Tabeling and Lichaber used the theoretical prediction of Park and Homsy [139] for the pressure drop across the interface for $Ca \to 0$:

$$\Delta P = \frac{\gamma}{b/2} \Big(1 + 3.80\, Ca^{2/3} \Big) + \frac{\pi}{4} \frac{\gamma}{R_{\parallel}}, \tag{3.5}$$

and found that their experimental pressure drop could be written as:

$$\Delta P = \frac{\gamma}{R_{\parallel}} \Big(\frac{\pi}{4} + 7.4\, Ca^{2/3} \cos^{2/3}(\theta)\, \frac{R_{\parallel}}{b} \Big), \tag{3.6}$$

where θ is the angle of the normal of the interface and the direction of the finger motion. From this expression, they derived a rescaled surface tension:

$$\gamma^{*} = \gamma \Big(\frac{\pi}{4} + 1.7\, \lambda_f\, (W/b)\, Ca^{2/3} \Big) \tag{3.7}$$

and a modified capillary number:

$$\frac{1}{B^{*}} = \frac{12}{\epsilon^2} \frac{\Delta \eta U}{\gamma^{*}} = \frac{1}{B} \Big(\frac{\gamma}{\gamma^{*}} \Big). \tag{3.8}$$

Their experimental results for the finger width λ_f indeed collapsed to the McLean-Saffman curve

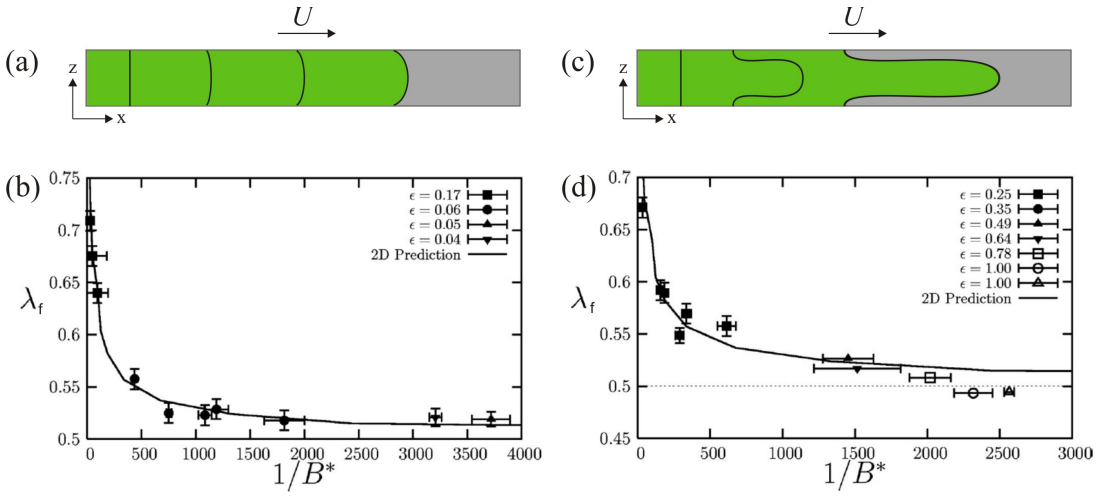


Figure 3.4: Finger width λ_f as a function of rescaled control parameter $1/B^*$ when the interface in the z-direction (a,b) advances as meniscus and (c,d) develops into the finger. Figures (b,d) taken from [126].

when plotted as a function of the parameter 1/B* (see figure 3.3 (b)). However, for large values of 1/B*, the experiments showed that the relative finger width λ_f can fall below the 1/2 limit [140]. More advanced simulations have indeed shown that such finger widths are possible [141].

Very recently, the forced displacement of a fluid-fluid interface in a three-dimensional channel, i.e. like the one depicted in figure 3.1, has been studied by Ledesma *et al.* [126, 142] by means of lattice Boltzmann simulations, with a focus on a neutral wetting situation (the contact angle between the two fluids and the boundary walls equals 90°). They found that the interface profile in the direction across the channel thickness (xz-plane) can develop into two possible configurations, determined by the velocity mismatch between the leading interface and the contact line. (i) When both velocities are comparable, the interface advances as a meniscus, as shown in figure 3.4 (a). (ii) Conversely, when the slip velocity cannot keep up with the leading interface velocity, the interface develops a finger shape, leaving behind a thin film of fluid adhered to the wall of the channel (see figure 3.4 (c)).

They proposed that the observed interfacial configurations are controlled by the following dimensionless parameters, the capillary and the Peclet numbers. The Peclet number is given by:

$$Pe = \frac{Ub}{D} \tag{3.9}$$

where D is the diffusivity of the concentration field, gives the ratio between advective and diffusive timescales.

They furthermore have shown that when the interface is a meniscus, the finger width λ_f can also be applied to a 2D prediction of McLean and Saffman [133] by introducing the effective surface tension (figure 3.4 (b)). Moreover, when a thin film is left behind in the xz-plane, the simulations revealed that the finger width λ_f decreases with an increasing aspect ratio ϵ, especially at high $1/B^*$, an observation that is consistent with previous experiments [140] (figure 3.4 (d)). The finger widths deviate systematically from the McLean-Saffman curve. This clearly demonstrates the importance of the third dimension in understanding the physics of viscous fingering.

3.5 Viscous fingering at ultralow interfacial tension

In the next chapters, we study the Saffman-Taylor instability by using colloidal fluids in microfluidics. This provides an excellent model system to study dynamics of fluid-fluid interfaces that are not accessible at the molecular scale. In particular, the colloidal system offers the following advantages: (i) since we are dealing with a colloidal, rather than a molecular fluid, the surface tension is reduced by a factor of $\sim 10^6$. This ties into the discussion about the surface tension acting as a singular perturbation in the Saffman-Taylor problem and, specifically, in its McLean-Saffman solutions (see, for example, [119, 141] for reviews of the problems). The experiments may thus shine light on the zero-surface-tension limit mentioned above [123]. (ii) The ultralow interfacial tension consequently gives rise to relatively large thermal fluctuations of the interface, with a width of the order of micrometres. This means that the role of interface fluctuations in the Saffman-Taylor problem can be explored in great detail. (iii) The large lengthscale and slow timescales of colloidal systems make them highly compatible with microfluidics techniques and laser scanning confocal microscopy (LSCM). In figure 3.5, we show that our combination of systems and techniques makes it possible to directly observe the finger in all three dimensions. Thus, it is possible to observe not only the fingering instability in the xy-plane (chapter 5) but also the curvature of the interface in the xz-plane (chapter 4).

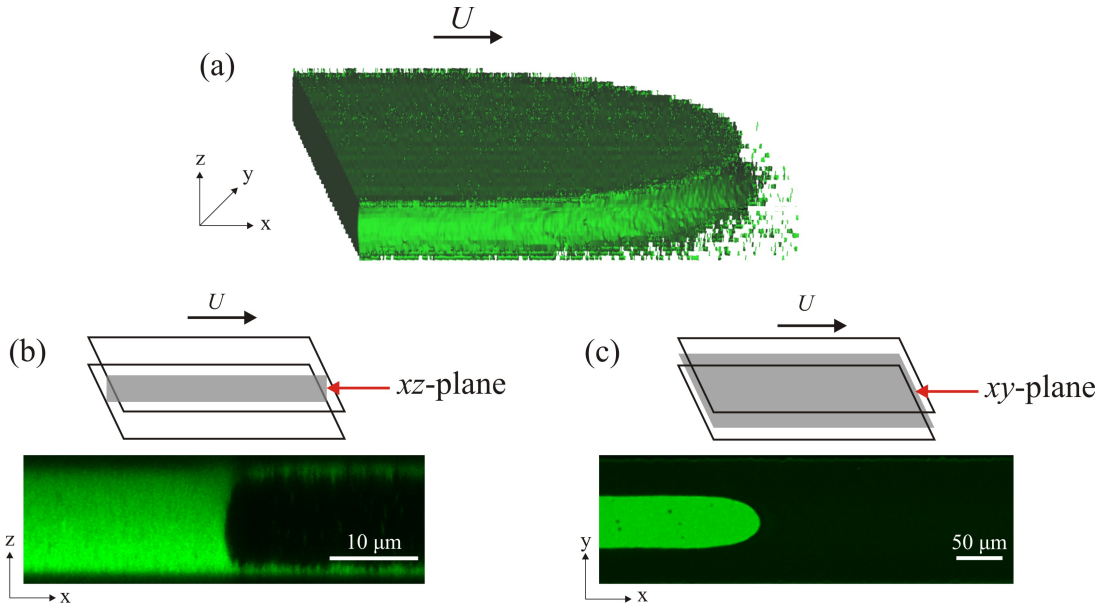


Figure 3.5: (a) Three-dimensional image of viscous fingering in microfluidic channel. (b) Interfacial curvature in the xz-plane observed by making a cut through the tip of the finger. (c) Saffman-Taylor finger in the xy-plane observed in the centre of the channel ($b/2$). All images were recorded by using LSCM.

3.6 Conclusion

We introduced the Saffman-Taylor instability. Starting with the classical two-dimensional results presented by Saffman and Taylor, we explained how the problem was tackled with a focus on the role of surface tension as a singular perturbation in the selection of the fingers. Discrepancies still remained between the experimental results and theoretical predictions, which were then linked to the three-dimensional nature of the interface.

Next, we explained that our colloidal system comes with several advantages, and the combination of the microfluidics technique and LSCM enables us to explore the viscous fingering instability in three dimensions. In the upcoming chapters, we will discuss our experimental set-up and results, beginning with observations in the xz-plane (chapter 4), followed by the Saffman-Taylor instability in the xy-plane (chapter 5). In chapter 6, we present a related dynamic contact line instability by exploiting the Saffman-Taylor experiments.

Chapter 4

Viscous fingering at ultralow interfacial tension: the 3^{rd} dimension

ABSTRACT

We experimentally study the viscous fingering instability in a fluid-fluid phase separated colloid-polymer mixture by means of laser scanning confocal microscopy and microfluidic devices. We focus on the variations of the interfacial curvature in the channel thickness direction (xz-plane) as a function of flow velocity, dealing with the following two aspects: (i) the interface between the two demixed phases has an ultralow surface tension, such that we can address the role of thermal interface fluctuations. (ii) The displacing fluid wets all walls completely, in contrast to traditional viscous fingering experiments in which the displaced fluid wets the walls. We make comparisons with lattice Boltzmann simulations, which help to interpret the experimental observations.

4.1 Introduction

The dynamics of the interface between two fluids confined to a porous medium or Hele-Shaw cell have stimulated applied and fundamental research over the last decennia. A typical example is the viscous fingering process, where a low viscosity fluid penetrates a high viscosity one. The phenomenon leads to an unstable interface where a finger-like structure emerges and competes until finally only a single finger becomes dominant. As we have discussed in chapter 3, the finger is a fundamental three-dimensional structure; a thin film of the more viscous fluid, adhered to the walls and left behind the advancing finger, modifies the capillary pressure, thus changing the curvature of the interface in the 3^{rd} dimension. This has been confirmed in experimental work by Tabeling and Lichaber [137], in which they demonstrated that this was an important ingredient in the viscous fingering instability.

In this chapter, we study the penetration of the interface in the channel thickness direction (lateral view of the viscous fingers — grey plane in figure 4.1) by using colloidal fluids, which enables us to revisit the problem introduced above. We study the interfacial profile by means of laser scanning confocal microscopy (LSCM) in microfluidics. Specifically, we address the following two different issues: (i) the interface of the phase separated colloidal fluids is characterised by an ultralow interfacial tension, which makes it possible to directly observe thermal capillary waves at the interface [10]. Furthermore, thermal interface fluctuations may modify continuum hydrodynamics [143–145] and, thus, the instability. (ii) In our system the low viscosity, displacing phase completely wets the confining walls, which is the opposite wetting situation to traditional viscous fingering experiments, where the displaced fluid wets the walls and leaves behind a thin film, as explained above. Such a strong attraction to the walls, consequently results in a concave meniscus of the interface at rest, where the behaviour as a function of flow velocity is expected to be much richer, as illustrated in figure 4.1 (c). This directly implies that the interface curvature in the xz-plane will play a different, more pronounced role than in the experiments of Tabeling and Libchaber [137]. We furthermore note that our wetting situation is similar to that in imbibition experiments [146], where a liquid is sucked up in, e.g. a porous medium by capillary effects; however, we push the displacing fluid, which has a lower viscosity than the displaced fluid, at velocities of at least an order of magnitude above the spontaneous imbibition velocity as checked by simulations, and the observed phenomena are therefore best analysed within the viscous fingering framework.

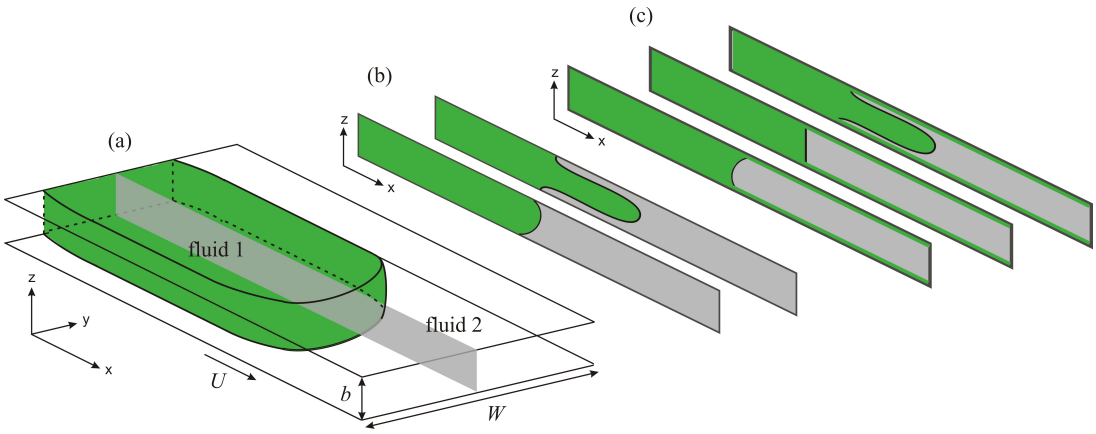


Figure 4.1: (a) Schematic depiction of a viscous finger in a Hele-Shaw geometry, with fluid 1 (low viscosity) displacing fluid 2 (high viscosity). The evolution of the interfacial curvature in the xz-plane (grey plane) will be made through the tip of the finger by means of LSCM. (b) Two possible interface configurations can be foreseen in the case of neutral wetting [142]: (left) a meniscus and (right) a finger shape (see chapter 3). (c) In our complete wetting situations, the behaviour of the interface as a function of flow velocity is expected to be much richer.

Our strategy is first studying the three-dimensional profile of the interface as a function of flow velocity and establishing the relevant control parameters to describe the phenomena. Secondly, we will study the behaviour of the penetrated finger in the xz-plane at a steady state, in which the width λ_b and the curvature of the leading interface κ will be analysed.

To further elucidate our experimental findings, we will compare experiments to lattice Boltzmann (LB) simulations, which effectively solve the Navier-Stokes equations and provide detailed information about the various physical parameters at play, which can be varied over a wide range.

The chapter is organised as follows. In section 4.2 we introduce the experimental details, followed by a description of the lattice Boltzmann simulation technique in section 4.3. Section 4.4 describes the results and discussion, and finally the work is concluded in section 4.5. In the next chapter (chapter 5), we will address the role of the interfacial curvature in the xz-plane in the viscous fingering in the xy-plane.

4.2 Experimental details

4.2.1 Experimental set-up

We used the system of fluorescently labelled poly(methylmethacrylate) (PMMA) colloidal particles and xanthan polymer dispersed in water at statepoint $\phi_c = 0.12$, $\phi_p = 5.08$ (point I in figure 2.2, chapter 2) to perform the viscous fingering experiments in microfluidic channels. A stock solution of a colloid-polymer mixture of around 1 g was prepared, homogenised by vigorous shaking, and allowed to phase separate completely within 24 hours. The two resulting colloidal-liquid and -gas phases were then carefully isolated with a syringe. Gravity was found to have a pronounced effect on the distribution of the colloidal particles in each phase [73, 147] and care must be taken that this does not affect the experiments. Those effects only start to play a role after $\sim$ 2 days and phases were isolated before that. The two colloidal phases will be at coexistence when brought into contact again. The interfacial tension $\gamma = 30$ nN/m was obtained from the analysis of the capillary wave spectrum (section 2.3, chapter 2). A rheological characterisation was performed on a TA AR-G2 rheometer giving a viscosity contrast ratio of $r = (\eta_2 - \eta_1)/(\eta_2 + \eta_1) = 0.4$ (section 2.4.1, chapter 2). Noticeable shear thinning, which is known to have a thinning effect on the Saffman-Taylor fingers (see, for example, [125, 148] and references therein), was observed for the colloidal gas phase from a shear rate of ~ 30 s^{-1}, which was above the maximum shear rate in the experiment (estimated as $U/b \sim 0.3$ s^{-1}).

The experimental set-up was shown in figure 4.2 (a). The microfluidic channels which have been designed as in figure 4.2 (b) were fabricated using soft-lithography techniques in which the width W and thickness b were fixed at 110 μm and 10 μm, respectively. Two inlet holes and one outlet hole were punched at the ends of the channel. To perform the viscous fingering experiments, the separated colloidal fluids were directly injected into the inlet ports of the channels using syringes through micro-gauge tubes. The flow of the individual fluids was controlled using gravity by changing the height of the syringes. A flat interface was first formed at the centre of the cross-channel. The colloidal liquid phase, which had a lower viscosity η_1, then pushed the colloidal gas phase (with viscosity η_2) along the straight channel, from which point the development of viscous fingers was recorded. The spontaneous development of the fingers in three dimensions was directly recorded by means of LSCM in which only the fluorescence of excited dye within the colloids (colloidal liquid phase) was visualised. The LSCM technique

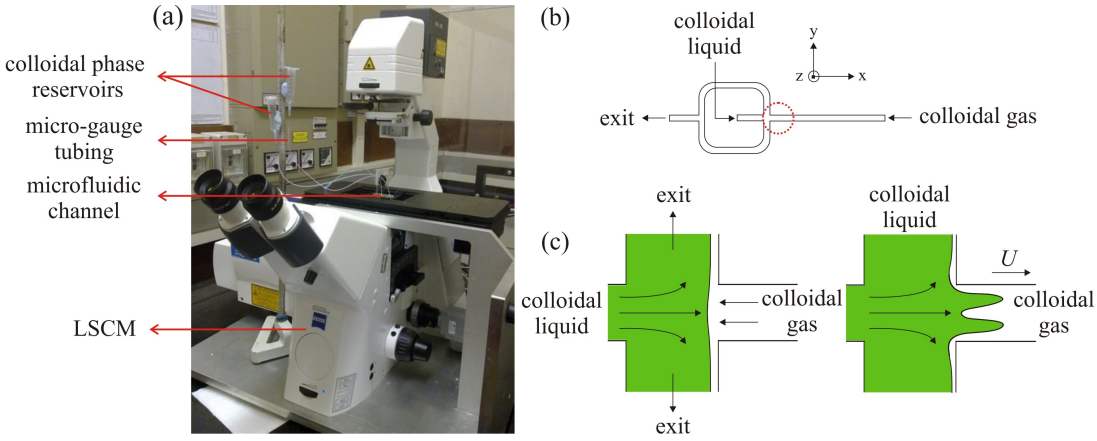


Figure 4.2: (a) Experimental set-up. LSCM (Zeiss Exiter) was used to image the instability phenomena. (b) Schematic depiction of the microfluidic devices. (c) The zoomed area indicated by the dashed red circle showing the flow of the colloidal fluids in microfluidics. A straight colloidal interface was first formed before the low viscosity, colloidal liquid phase was pushed into a long, flat channel whereby initiating fingering.

gives us an advantage to record the viscous finger in all three dimensions, including the curvature of the interface in the xz-plane, with very high-resolution imaging due to its ability to image a very thin slice of the system. Thus, it minimises the shadow and reflection effects when scanning across the channel thickness direction.

4.2.2 Image analysis

(i) Finger width λ_b in the z-direction

A steady state finger is characterised by the width relative to the thickness of the channel, $\lambda_b = W_b/b$, with W_b being the finger width in the xz-plane. To analyse, we first binarised the LSCM image, and then constructed an intensity profile by averaging the intensity of each row in the image. We only consider data at the front of the finger where it has flat sides. An example of the binarised image and its intensity profile are demonstrated in figure 4.3 (a) and (b), respectively. The intensity profile can become distorted in the z-direction due to scattering by the colloids. Additional distortion of the intensity profile can be caused by the refractive index mismatch between the sample (where we consider the refractive index of the solvent to be a representation of the refractive index of the sample; $n_{sample} = 1.33$) and the immersion medium of the lens ($n_{oil} = 1.51$, Zeiss 'Immersol'), leading to an elongation of the image. The

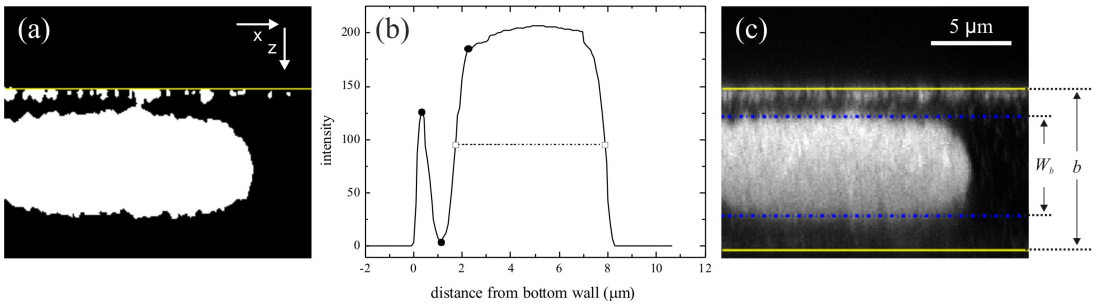


Figure 4.3: (a) Binarised image and the yellow line indicating the located position of the bottom wall. (b) Intensity profile showing the position of relevant turning points (full circles) and crossing points at half peak height (open squares). (c) Example of calculated finger width W_b (dashed/blue lines) and channel thickness b (yellow lines).

image is stretched by a factor of 1.2 in the z-direction, in order to correct for this [149].

The location of the wall was determined by finding the location of the steepest gradient in the first peak of the profile. Figure 4.3 (a) shows the calculated position of the wall (yellow line). With this analysis it was not possible to determine the top of the wall, as the intensity becomes too low due to scattering of the colloidal particles. Alternatively, the position of the top wall was estimated through visual examination of the image with the improved contrast using Mathematica software, although this was not as accurate as for the bottom wall. However, by filling the channels with glycerol + rhodamine dye, which leads to a smaller distortion ($n_{glycerol} = 1.47$), the channel thickness b was measured to be 10 μm. The value was used to determine the correction factor when measuring the channel thickness in the aqueous systems.

The width of the finger W_b was calculated by locating the positions of the peaks in the intensity profile by numerical differentiation. The located positions of these peaks can be seen in figure 4.3 (b) (full circles). The halfway intensity value between the second and third points was calculated (marked as an open square) and extrapolated through crossing the profile. The finger width was taken as the distance between the crossing points, as shown by the dashed line. When we consider the colloid-polymer mixtures, the interface is rough due to the large thermal capillary fluctuations, leading to a possible overestimation of the finger width. The thermal roughness was found to be 1.2 μm (see section 2.3). Half of this value was considered an error bar when calculating the width of the finger W_b. In figure 4.3 (c), we show the calculated finger width W_b (dashed/blue lines) and the thickness of the channel b (yellow lines).

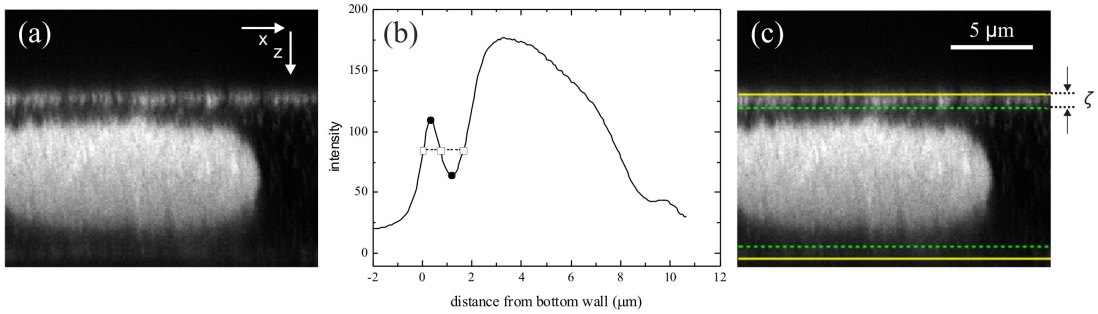


Figure 4.4: (a) LSCM image. (b) Intensity profile showing the position of relevant turning points (full circles) and crossing points at half peak height (open squares). (c) Example of calculated thickness of wetting layers ζ (dashed/green lines) from the located position of the walls (yellow lines).

(ii) Wetting layer thickness ζ

In order to calculate the thickness of the wetting layer on the wall, we first plot the average intensity profile of the raw LSCM image. An example of the LSCM image and the average intensity plots are demonstrated in figure 4.4 (a) and (b), respectively. Analysis of the intensity profile was performed in a similar manner to the finger width analysis. The turning points were located by numerical differentiation (marked as full circles in figure 4.4 (b)). The height halfway between the first points was calculated and extrapolated across the profile. The positions where the dashed line crosses the intensity profile are marked by open squares, and the distance between the first two crossing points has been taken as the average width of the wetting layers following [68]. It was not always possible to calculate the width of the top wetting layer: the intensity was too low when going deep inside the channel due to scattering by the colloidal particles, and this effect leads to an overestimation of the top wetting layer. Thus, we have always used the data on the bottom wetting layer to indicate the layer thickness. In figure 4.4 (c), we demonstrate the calculation of the width of the wetting layers (dashed/green lines).

(iii) Interfacial curvature in the xz-plane

To measure the radius of curvature of the xz-finger in the channel thickness direction, we first located the position of the interface using a gradient method of Mathematica. An edge was located wherever a jump in intensity in the image was observed. The magnitude of the intensity gradient at the edge was defined as $|\nabla f| = \sqrt{\left(\frac{\partial f}{\partial x}\right)^2 + \left(\frac{\partial f}{\partial z}^2\right)}$, which has a direction given by $\theta = tan^{-1}\left(\frac{\partial f}{\partial z}/\frac{\partial f}{\partial x}\right)$, where x and z are the row and column coordinates respectively. Local

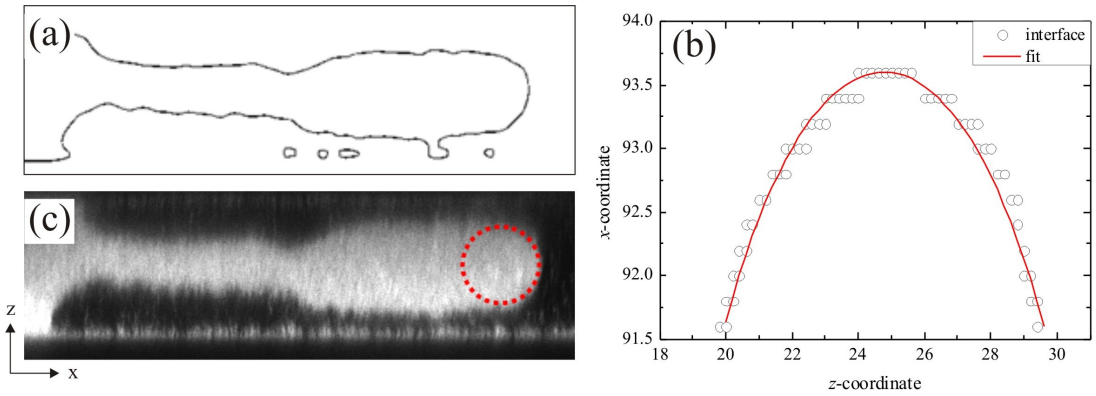


Figure 4.5: Evaluation of the radius of curvature of the xz-finger. (a) Interface detection by means of gradient method. (b) Plot of located position of the interface and a fit from circle equation of radius R_{exp}. (c) LSCM image of xz-finger with fitted circle at the tip (dashed red line).

maxima of the gradient magnitude identify the interface. The effect of noise was suppressed by binarising the raw image. In figure 4.5 (a), we show an example of interface detection by means of the gradient method. We are only interested in measuring the radius of curvature at the tip of the finger. Next, the located interface was fitted to a circle where the radius R_{exp} is defined as the radius of curvature at the tip of the finger (see figure 4.5 (b)).

4.3 Lattice Boltzmann simulation

The simulations were performed independently by my colleague, Dr. I. Zacharoudiou (former D Phil student under supervision of Prof. J. M. Yeomans, Prof. D. G. A. L. Aarts and Dr. A. A. Louis) at the Rudolf Peierls Centre for Theoretical Physics, University of Oxford.

The free energy lattice Boltzmann method [150, 151] (D3Q19 model) was used, which numerically solves the hydrodynamic equations of motion for a binary fluid. In order to study the penetration process in the xz-plane, a channel formed by two plates of infinite width, parallel to the xy-plane, located at $z = 0$ and $z = b$, was considered. Channel dimensions were, in simulation units, $b = 50$ - 100 and length $L = 1000$ - 2000, whereas the thickness of the wetting layer was $\zeta \sim 5$. A constant body force was applied to both phases. Typical fluid viscosities were $\eta_1 = 0.017$, $\eta_2 = 0.036$ ($r = 0.36$) and $\eta_1 = 0.017$, $\eta_2 = 0.33$ ($r = 0.90$) to match the experiments.

4.4 Results and discussion

4.4.1 Three-dimensional profile

In this section we will focus on the experimental interface shape in the z-direction. It turns out that the behaviour of the meniscus is surprisingly rich. Figure 4.6 (a) illustrates that our combination of the system and techniques allows observing the viscous fingers fully in 3D. The left column of figure 4.6 (b) shows a sequence of images of the penetration process as a function of the capillary number; the data are obtained by making an xz-cut through the tip of the advancing finger. The unique wetting situation, which is further illustrated by the presence of thick wetting layers, will amplify any possible curvature effects. The wetting can be qualitatively understood by considering the depletion interactions in play; due to a strong attraction between the colloidal particles and the wall, the colloidal-rich "liquid" phase wets the microfluidic walls completely [49, 85].

At low velocities, the interface advances as a concave meniscus. At a capillary number $Ca'_{xz} = (\eta_1 + \eta_2)U/2\gamma \sim 0.4$, the xz-interfacial profile in the centre of the channel is flat, i.e. its curvature is zero. We note here that we use the average viscosities in the definition of a capillary number as a scaling analysis shows that this is the relevant term [53], and U is the flow velocity. The curvature then changes into a convex meniscus. At this point, the slip velocity at the contact line[1] is comparable to the leading interface velocity in the centre of the channel ($U_s = U$) to maintain the meniscus shape. Then, at higher $Ca'_{xz} \sim 1$, the interface velocity becomes decoupled from that of the contact lines ($U_s < U$), and a finger shape develops in the z-direction, which we will call an xz-finger. The finger emerges from the centre of the channel, leaving behind a thin film of fluid. We stress that this is due to a completely different mechanism from the Saffman-Taylor fingering that will be discussed in chapter 5; it is not driven by an instability of the interface, but rather by the inability of the contact line to move as quickly as the leading interface. The developed finger has a characteristic shape with a narrowing neck between the bulk of the displacing fluid and the front of the finger. At higher capillary numbers a meandering motion of the finger is observed, where it makes contact with either the top or bottom wall (see figure 4.6 (c)) before continuing to move freely again in

[1] As we are in the complete wetting regime, the liquid slides over a colloid-rich wetting layer such that there is no true contact line. However, there is an obvious line where the curved meniscus meets the surface layer, for which contact line is a natural terminology.

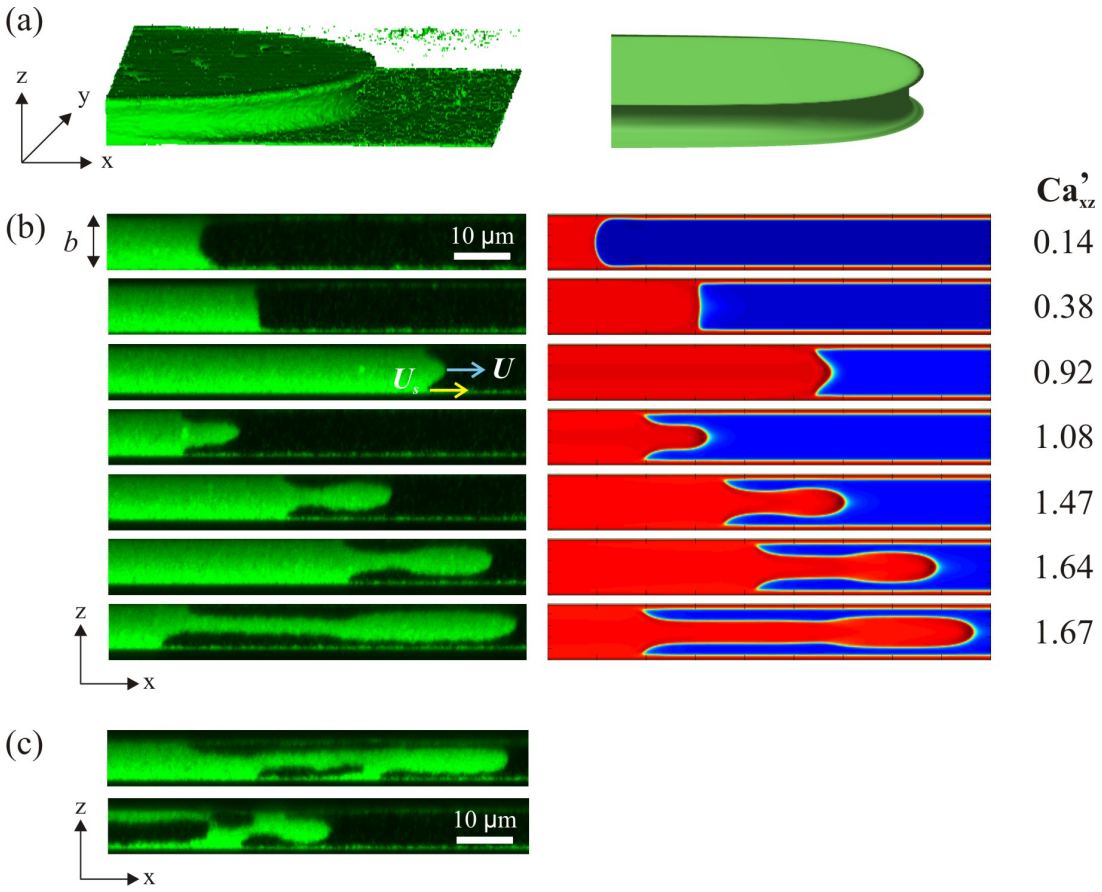


Figure 4.6: (a) 3D images of a single finger from experiments (left panel) and lattice Boltzmann simulations (right panel). (b) Profile of the finger in the xz-plane as a function of the capillary number Ca'_{xz}. LSCM images of the leading interface are compared to the simulations. (c) LSCM images of fingers merging with the top or bottom wetting layers at large capillary numbers, before being pulled back to the centre of the channel, which is the meandering motion of the xz-finger.

the centre of the channel. This is a consequence of the large thermal interface fluctuations in colloid-polymer mixtures and, therefore, intimately related to the ultralow interfacial tension of our system; the advancing xz-finger can feel the wetting layers and, thus, bridge the gap until the mismatch in tip vs. contact line velocity brings the xz-finger in the centre of the channel again. The meandering entraps bubbles of the high viscosity phase in the advancing finger.

4.4.2 Comparison with lattice Boltzmann simulations

The right column of figure 4.6 (b) presents simulation results showing how the xz-interfacial profile responds to the flow, in close correspondence with our experiments at the same capillary

number. When using the lattice Boltzmann approach to model interfaces in molecular fluids, discretisation constraints mean that the diffuse interface is unphysically wide and care must be taken that this does not affect the results. Here, however, the relatively large interfacial width of our colloid-polymer mixtures allows a quantitative match between experiment and simulation: excellent agreement is found. In the simulations the hydrodynamic singularity at the contact line is alleviated by interdiffusion, driven by the chemical potential imbalance as the interface is pulled out of thermodynamic equilibrium. In the experiments it is likely (although not proven) that the mechanism for contact line motion is the same (see chapter 6). This gives us the confidence to use the simulation to interpret the mechanism behind the interfacial transition.

Recently, Ledesma *et al.* [142] have argued, based on a scaling argument relating the velocity of the leading interface to that of the contact line, that for fluids at neutral wetting (i.e. a contact angle of 90°), fingering in the xz-plane occurs for $Pe > c(Ca_{xz})^{-1}$, where the Peclet number $Pe = Ub/2D$, with c a constant of order 1. An extension of their argument to complete wetting and fluids of different viscosity gives [53]:

$$Pe^* > c\,(Ca^*_{xz})^{-1} + \delta \tag{4.1}$$

with the rescaled Peclet and capillary numbers:

$$Pe^* = \frac{U(b/2-\zeta)}{D} \tag{4.2}$$

and:

$$Ca^*_{xz} = \left\{1 - 4\Big(\frac{\zeta}{b}\Big)\Big(1-\frac{\zeta}{b}\Big)\right\} Ca'_{xz}. \tag{4.3}$$

The offset δ accounts for the width ζ of the wetting layer at the surfaces. For a full theoretical derivation, see [53].

Figure 4.7 (a) summarises numerical results in the $(Pe^*, (Ca^*_{xz})^{-1})$ plane, confirming the validity of this prediction for a viscosity ratio $r = 0.36$. The solid line corresponds to $c \sim 150$ and $\delta \sim$ -140. Data shown in the figure describe two regions: to the right of the solid line, the system moves in the meniscus regime, while to the left of the solid line, xz-fingers develop. The different xz-interface configurations are represented by the snapshots. Note that c takes a value two orders of magnitude larger than that for neutrally wetting molecular fluids [142].

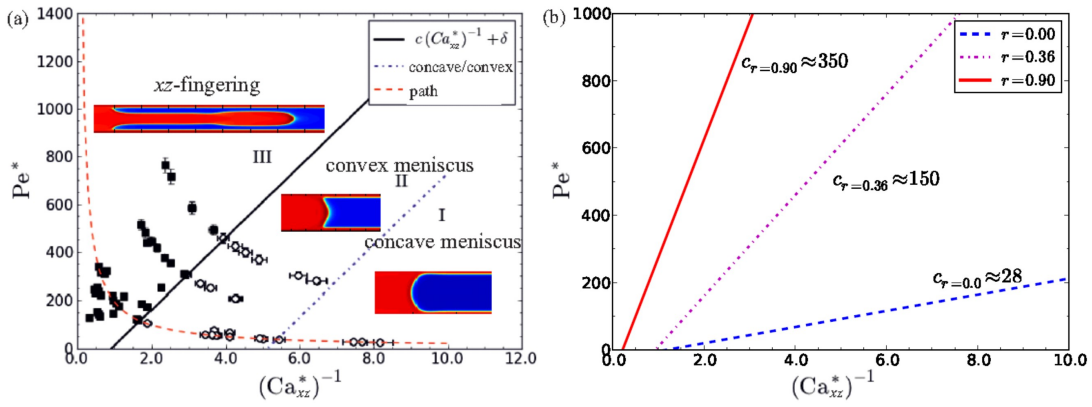


Figure 4.7: Results from lattice Boltzmann simulations [53]. (a) The shape of the interface in the xz-plane for a viscosity contrast $r = 0.36$ depends on the scaled capillary and Peclet numbers, Ca^*_{xz} and Pe^* (∘ meniscus regime, ■ thin film regime). The snapshots represent the different configurations. The solid line corresponds to the onset of fingering in the z-direction; the dash-dotted/blue line indicates an advancing interface with zero curvature κ. The dashed/red line describes an experimental path, where Pe^* and Ca^*_{xz} can be tuned by means of the velocity of the leading interface. (b) The onset of fingering in the z-direction depends on the viscosity contrast. Increasing the viscosity contrast suppresses the finger formation.

This is entirely due to the wetting properties of our fluids. The increased ease with which the contact line can move across the pre-formed wetting layer means that fingering in the z-direction is strongly suppressed. Nevertheless, we find the same qualitative behaviour for the cross-over between meniscus and thin film regimes as in the neutral wetting situation, although now the offset δ accounts for the presence of the wetting layer (we assume $\delta = 0$ for neutral wetting). For both situations, the penetration process is governed by the interplay of capillary and Peclet numbers.

When comparing this numerical phase diagram with our experiments, an excellent agreement is found. The experimental path can be estimated from the $(Pe^*, (Ca^*_{xz})^{-1})$ plane (denoted by the red/dashed line in figure 4.7 (a)) by considering $Pe^*/Ca^*_{xz} = const$, since for a given channel thickness, both the Pe^* and Ca^*_{xz} are varied by slowly increasing the velocity of the interfaces while the other parameters are kept constant. This means that we scan the $(Pe^*, (Ca^*_{xz})^{-1})$ phase diagram from the bottom-right corner (slow velocity) to the top-left corner (high velocity). Note that Pe^*, Ca^*_{xz} and r have been matched to the experiments. The interface thus first moves with a concave meniscus. At intermediate velocities it moves with a convex meniscus. Finally, after crossing the full straight line, it displays xz-fingering. Moreover,

in our experiments the typical velocity at which fingering in the xz-plane commences is $U \sim 2.7$ μm/s, which corresponds to $Ca'_{xz} \sim 1$. With the thickness of the wetting layer $\zeta \sim 1$ μm, we obtain the inverse rescaled capillary number at which fingering commences as $1/Ca^*_{xz} \sim 1.6$. Then, using the Stokes-Einstein equation, we obtain the diffusion coefficient of the colloids $D =$ 9.9 x 10^{-14} m^2/s and an experimental $Pe^* \sim 110$. This compares favourably to $Pe^* \sim 100$ at $1/Ca^*_{xz} \sim 1.6$ found in the simulations.

In addition, simulations further reveal that the onset of fingering in the xz-plane varies with the viscosity ratio r, as shown in figure 4.7 (b). As the difference in viscosity of the two fluids increases, they find that fingering in the z-direction is even more strongly suppressed: much higher capillary numbers are needed both to change the shape of the meniscus from concave to convex and to induce the formation of a finger. Numerically, $c \sim 350$ and $\delta \sim -75$ for $r = 0.90$ (red line) is found, while $c \sim 28$ and $\delta \sim -38$ for $r = 0$ (dashed/blue line).

4.4.3 Steady state finger in the channel thickness direction

We would like to turn our discussion to the steady state finger in the channel thickness direction that appears at high velocities. We have found that the channel thickness does have an important effect on the fingering instability (see chapter 6). In the current chapter, however, we focus on the fingering in which the steady state remains insensitive to the channel thickness chosen ($b =$ 10 μm). Previous studies have suggested that the relevant control parameters to describe the steady state of the xz-finger are the capillary number and viscosity contrast between the fluids. In figure 4.8 (a), we plot λ_b as a function of Ca_{xz}, at a given viscosity contrast. The relative width λ_b of the xz-finger has been measured as described in section 4.2.2. Here, we define the capillary number as $Ca_{xz} = \eta_2 U/\gamma$, where η_2 is the viscosity of the penetrated fluids (colloidal gas phase), to make a direct comparison with previous analysis.

The first detailed analytic prediction of a bubble in a tube was given by Bretherton [154] who reported that the width decays as $\lambda_b \to 1 - 1.337(Ca_{xz})^{2/3}$, as $Ca_{xz} \to 0$ for the fluids with $r = 1$. Taylor [155] then extended the work experimentally and showed a dependence of $1 - (Ca_{xz})^{1/2}$, which is a very similar result proposed by Fairbrother and Stubbs [156], up to $Ca_{xz} = 0.09$. Using a finite different algorithm to solve the Stokes equation and considering values up to $Ca_{xz} > 2$, Reinelt and Saffman [157] were able to reproduce Taylor's 1/2 exponent. Halpern and Gaver [152] extended the prediction beyond $Ca_{xz} = 2$ by means of a boundary

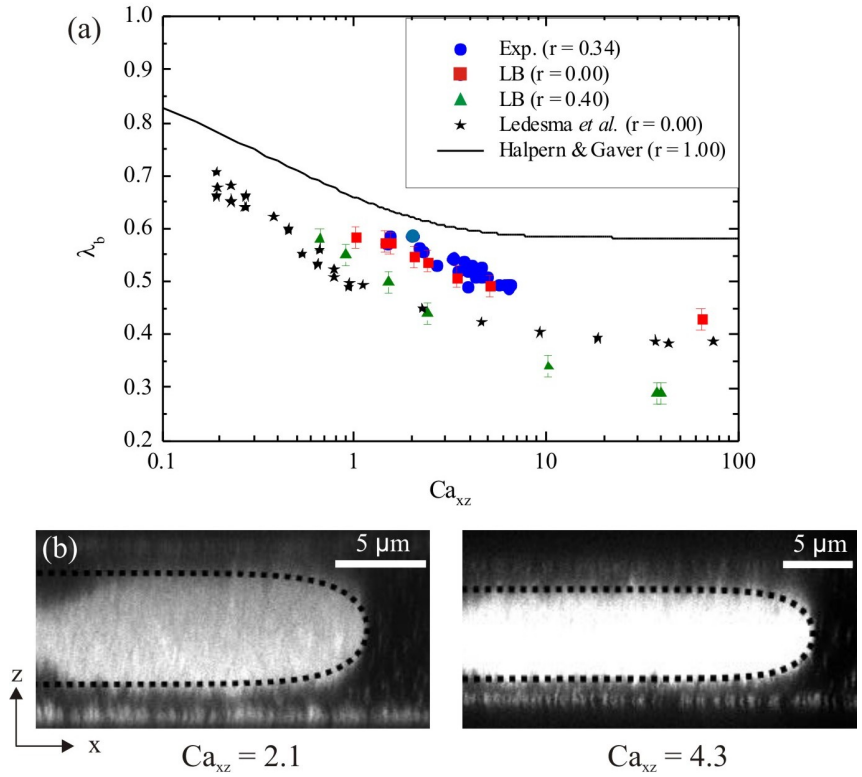


Figure 4.8: (a) Width of xz-finger λ_b as a function of $Ca_{xz} = \eta_2 U/\gamma$ for different viscosity contrast r. For a comparison, we plot the numerical prediction curve by Halpern and Gaver [152] for $r = 1$ (straight line) and also results from Ledesma *et al.* [142] for neutral wetting fluids with $r = 0.0$ (denotes as $\star$). (b) Interface profile of steady state xz-finger at different Ca_{xz} values. The dashed curve follows from the Pitts equation [153].

element analysis of the Stokes equation and showed that the finger width can be fitted to an exponential law $\lambda_b = 1 - 0.417[1 - \exp(-1.69\,(Ca_{xz})^{0.5025})]$ (full line in figure 4.8 (a)). For the low Ca_{xz} regime, their results are consistent with the power law prediction of Taylor [155] and reproduce the results obtained by Reinelt and Saffman [157], whereas for a high Ca_{xz} regime, the finger width saturates at a constant value of $\lambda_b = 0.580$. Most recently, Ledesma *et al.* [142] have addressed this problem by means of the lattice Boltzmann method, which covers the capillary numbers: $10^{-2} \leq Ca_{xz} \leq 10^2$, and fluids with the viscosity contrast ratio: $r \to 1$ and $r = 0$. For $r \to 1$, their results match with the Halpern and Gaver [152] prediction. For a zero viscosity contrast, they observed a thinning effect on the width of the finger: at a low Ca_{xz} regime ($0.1 \leq Ca_{xz} \leq 1$), the finger width follows the power law behaviour $(Ca_{xz})^{0.29}$, while at a high Ca_{xz} regime ($Ca_{xz} > 10$), the finger width saturates to a value of $\lambda_b \simeq 0.386$ (stars in figure 4.8 (a)).

Experimentally, we find that λ_b depends on the viscosity contrast and Ca_{xz}, as the points of our experiments fall in between the curves of those limiting cases ($r = 1$ and $r = 0$) (circles in figure 4.8 (a)). Again, we make a comparison with lattice Boltzmann results obtained by Dr. I. Zacharoudiou [53] for a system with viscosity contrast $r = 0.4$ (squares in figure 4.8 (a)). Note that the ratio of the wetting layer to the channel thickness ζ/b has been matched to the experiments. A good agreement was obtained between experiments and simulations. Simulations further reveal for a high Ca_{xz} regime that the xz-finger width saturates to a constant value of $\lambda_b = 0.417$. This regime (especially for $Ca_{xz} > 10$), however, was not possible to explore in experiments due to the meandering motion of the xz-finger, as mentioned before (see also chapter 6).

In addition, simulations show a narrower finger in the xz-plane with viscosity contrast $r = 0.0$, in agreement with the tendency that λ_b decreased with decreasing r (triangles in figure 4.8 (a)). However, the fingers are much thinner than in the neutral wetting case [142], especially for a large Ca_{xz} regime, where they find that the finger width saturation value is $\lambda_b = 0.29$. One would expect that for both wetting situations with a similar viscosity ratio, the finger width would be the same; therefore, the presence or the absence of the wetting layer does not have any contributions. A detailed experimental verification is needed to support the observations.

Moreover, preliminary experiments using a similar colloid-polymer mixture to ours, performed independently by G. J. Davies (*Part II student under supervision of Prof. D. G. A. L. Aarts at Physical & Theoretical Chemistry Department, University of Oxford*) [158] with a high viscosity contrast $r = 0.84$, show a wider xz-finger (see figure 4.9), supporting previous predictions that λ_b could be controlled by tuning the viscosity contrast. However, again, due to the large interface thermal fluctuations in the colloid-polymer system, the xz-finger experiences a meandering motion; thus, measurements of λ_b at high Ca_{xz} are not possible.

We now focus on the shape of the steady state xz-finger. As explained before, our fingering in the xz-plane is fundamentally different from those of the Saffman-Taylor problem. The xz-finger profile at the front, however, is very similar to the Saffman-Taylor finger that develops in the xy-plane. We compare the shape of the xz-finger with the semi-empirical Pitts equation [153], given by:

$$\cos\left(\frac{\pi z^{'}}{\lambda_b\, b}\right) = \exp\left(\frac{\pi x^{'}}{\lambda_b\, b}\right) \tag{4.4}$$

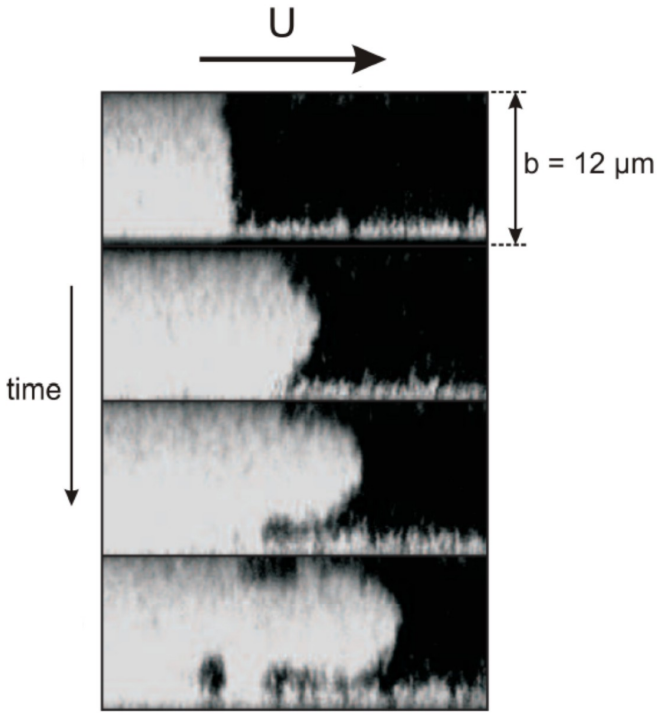


Figure 4.9: LSCM snapshots of xz-finger for system with $r = 0.84$. A wider finger is observed. However, due to a meandering motion, the measurements of λ_b are thus not possible. These preliminary experiments were performed, independently by G. J. Davies [158], using similar colloid and polymer mixtures to ours.

where x' and z' measure the distance from the xz-finger tip. Figure 4.8 (b) shows that the interface profiles can be well described by equation (4.4) at different capillary numbers.

4.4.4 Curvature of the leading interface in the xz-plane

We now turn our attention to the curvature of the leading interface in the channel thickness direction. In figure 4.10 we plot the normalised curvature $\kappa' = b^*/R_{exp}$ as a function of $Ca_{xz} = \eta_2 U/\gamma$. Here, $b^* = (b - 2\zeta)$ the effective width of the cell and R_{exp} the measured radius of the curvature from LSCM images as shown in figure 4.5. At low capillary numbers, where the interface is a concave, we expect that its radius $R = (b - 2\zeta)/2$, which is set by the channel gap and the thickness of the wetting layer. Upon inserting this equation to define the normalised curvature, we obtain $\kappa' \sim 2$, as shown in the figure. They match with results obtained by lattice Boltzmann simulation [53]. Again, ζ/b has been matched to the experiments.

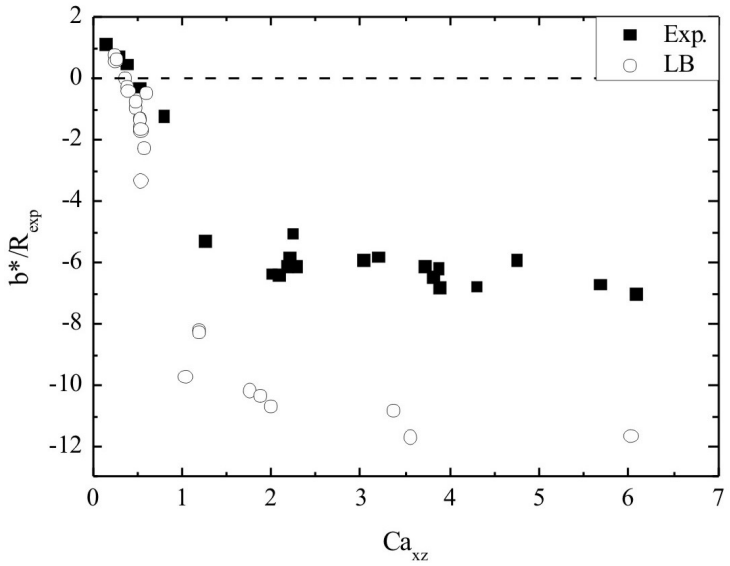


Figure 4.10: Normalised curvature $\kappa' = b^*/R_{exp}$ as a function of $Ca_{xz} = \eta_2 U/\gamma$. The dashed line indicates a flat advancing interface.

In addition, the advancing interface with zero curvature $\kappa' = 0$ (a flat advancing interface) and then the breakthrough in the xz-plane is observed at approximately the same Ca_{xz} in both experiments and simulations. However, as Ca_{xz} increases we observe a deviation between experiments and simulations, from which the interface curvature saturates to a different constant value. This might be attributed to the large thermal fluctuations in the experiments, which effectively increase the radius of curvature at the tip of the penetrating finger.

4.5 Conclusion

We have studied the xz-interface behaviour of the viscous fingers in colloid-polymer mixtures, both in experiments and in simulations. The combination of our techniques (LSCM and microfluidics) has enabled us to observe the fingering instability in three dimensions. We stress that fingering in the xz-plane is caused by the inability of the contact line to keep up with the leading interface instability and not by the interface instability identified by Saffman and Taylor. Furthermore, we can conclude that: (i) despite the ultralow surface tension between the two demixed phases, the xz-fingering displays the classic phenomena. The width of the xz-finger is a function of the capillary number and viscosity contrast, and the finger contour is well described by the Pitts equation. At larger driving velocities, we see a meandering motion

of the xz-fingers in the experiments, a consequence of the large thermal interface fluctuations in the colloid-polymer system. These phenomena, however, are not observed in the simulations. (ii) Our displacing fluid wets the walls of the microfluidic device. As a result, the curvature of the meniscus in the xz-plane is a function of the driving velocity. Lattice Boltzmann simulations subsequently reveal that the cross-over from a concave to a convex meniscus, and to xz-fingers, depends on the capillary and Peclet numbers, and on the viscosity contrast.

In the next chapter, we will describe the xy-behaviour of the viscous fingers and make the connection with this chapter.

Acknowledgments

It is a pleasure to thank Gareth J. Davies for pioneering experiments, Ioannis Zacharoudiou for the simulations, and Rodrigo Ledesma-Aguilar, Daniel Bonn, Roel Dullens, Ard A. Louis, Sebastien Moulinet, Denis Bartolo and Julia M. Yeomans for useful discussions.

Chapter 5

Viscous fingering at ultralow interfacial tension: xy-fingering

ABSTRACT

We study the development of viscous fingers in the xy-plane in the limit of ultralow interfacial tension by means of laser scanning confocal microscopy, and discuss the role of the interfacial curvature in the xz-plane, as shown in the previous chapter in the instability of the finger. It turns out that the concavity of the interfacial curvature in the xz-plane, where the displacing fluid wets the walls completely, suppresses the formation of the viscous finger in the xy-plane. Comparing with lattice Boltzmann simulation shines further light on the experimental observations. We furthermore show the rich stability behaviour of the viscous fingers in which the anomalous, tip splitting, side branching and coalescence between neighbouring fingers are observed.

5.1 Introduction

The study of the Saffman-Taylor instability started over fifty years ago, but continues to bring up new surprises that challenge our understanding of nonlinear pattern dynamics of interfaces. Compared to other pattern formation problems, this instability is more tractable and it has received much attention both theoretically and experimentally [159]. In particular, the observations of viscous fingering in a confined rectangular Hele-Shaw cell with an aspect ratio $\epsilon = b/W \ll 1$, where b is the channel thickness and W the channel width, led to the so-called *selection* problem. According to the McLean and Saffman two-dimensional prediction [133], there is a unique solution for the relative finger width λ_f (with respect to the channel width), which is governed by a dimensionless parameter $1/B = 12Ca_{xy}/\epsilon^2$. Here, $Ca_{xy} = (\eta_2 - \eta_1)U/\gamma$, with U being the velocity of the tip of the finger, γ the surface or interfacial tension, and η_1 and η_2 the viscosities of the displacing and displaced fluids, respectively, where $\eta_1 < \eta_2$. They furthermore showed that λ_f tends towards $1/2$ when $1/B$ goes to infinity. However, there was still a significant disagreement between the theoretical and experimental observations, showing fingers smaller than $1/2$, which was then related to the three-dimensional nature of the interface [137].

In this chapter, as a continuation from chapters 3 and 4, we extend the discussion on the viscous fingering instability with a focus on the development of the finger in the xy-plane (the wide dimension of the channel). As before, we use a mixture of colloids and non-adsorbing polymers which has an ultralow interfacial tension. This enables us to observe the finger at the scale of the thermal fluctuations. We seek the effect of the interfacial curvature in the xz-plane on the formation of the viscous fingering in the xy-plane, which shows deviations from 2D Saffman-Taylor fingers.

To begin, we first present the linear stability analysis of the interface in the two-dimensional limit (section 5.2), followed by the description of the experimental set-up (section 5.3) and the lattice Boltzmann simulation technique (section 5.4). The subsequent sections present the observation of fingering in the xy-plane (section 5.5.1) and discuss the interplay between the interfacial curvature in the xz-plane and the viscous fingering in the xy-plane, also in light of the lattice Boltzmann simulation [53] (section 5.5.2). We will then further discuss related phenomena of the viscous fingers in microfluidics devices (section 5.5.3). Finally, we conclude by considering the further implications of this work (section 5.6).

5.2 Linear stability analysis in the two-dimensional limit

Here we present the linear stability analysis of a flat interface in a Hele-Shaw cell that is subjected to a small perturbation, as illustrated in figure 5.1. We closely follow the derivation by Bensimon *et al.* [119]. The fluid flow in this system is effectively two-dimensional and obeys the Navier-Stokes equation [119, 160], which is given by:

$$\rho\Big[\frac{d\mathrm{v}}{dt} + (\mathrm{v}\,.\,\nabla)\mathrm{v}\Big] = -\nabla P + \eta\nabla^2\mathrm{v}, \tag{5.1}$$

where ρ and v are the density and the speed of the fluid, respectively, and P is the pressure. For small Reynolds numbers and assuming a small velocity gradient in the x- and y-directions compared to its spatial velocity, this equation reduces to a Stokes flow problem:

$$\nabla P = \eta\nabla^2\mathrm{v}. \tag{5.2}$$

By averaging over a flow profile which is assumed to be parabolic across the narrow direction z (perpendicular to the xy-plane, see figure 5.1 (c)), the mean velocity of the fluid can be defined as:

$$\mathrm{v} = U = -\frac{b^2}{12\eta}\nabla P. \tag{5.3}$$

We see that the flow satisfies the Poiseuille-Darcy equation, with permeability constant of $k = b^2/12\eta$. Thus, the Hele-Shaw flow is analogous to the two-dimensional incompressible flow in porous media (see [120] and the references therein).

Let us consider the flat interface being at a position $x(y) = Ut$, which moves with velocity U relative to the walls. A small deviation from flatness as shown in figure 5.1 (b) may be represented by writing:

$$x(y) = Ut + A(t)\cos(qy), \tag{5.4}$$

where the boundary condition imposed at the side walls requires the wavevector q to be $q = 2\pi n/W$, with n being an integer.

From the Stokes equation above, the pressure gradient needed to drive the motion of the fluid is $\nabla P = dP/dx = -12\eta U/b^2$. Adding to this equation a term representing the deviation

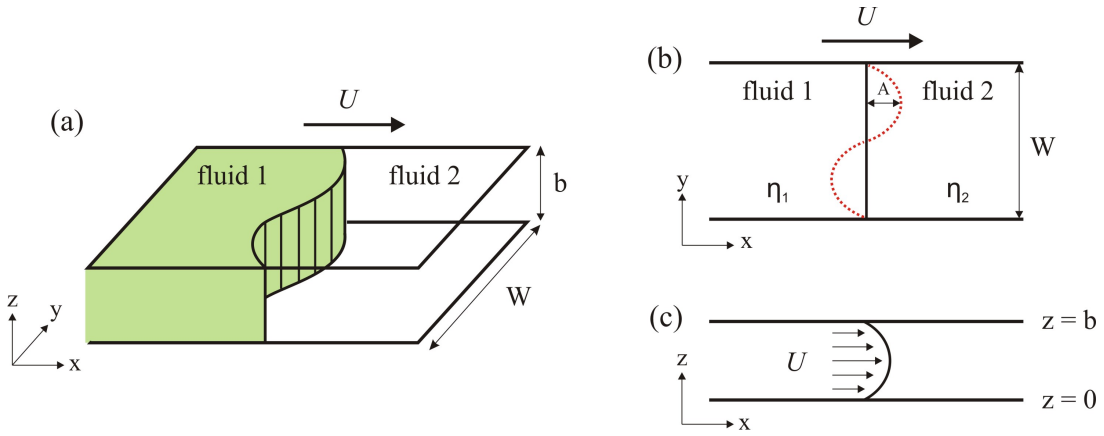


Figure 5.1: (a) Schematic diagram of a Hele-Shaw cell. (b) Schematic motion of the fluid-fluid interface with velocity U, which is then subjected to a perturbation of amplitude A. (c) Poiseuille velocity profile for flow between the two parallel plates.

from flatness, we find that:

$$P_1 = P_0 - \frac{12\eta U}{b^2}(x - Ut) + B(x,t)\cos(qy). \tag{5.5}$$

We furthermore assume that the fluids are incompressible, so that the divergence of the fluid velocity is zero, $\nabla . U = 0$. Thus, the pressure field satisfies Laplace's equation $\nabla^2 P = 0$, and $B(x)$ varies as e^{qx} or e^{-qx}. For the pressure to remain finite as $x \to \infty$, we find:

$$P_1 = P_0 - \frac{12\eta U}{b^2}(x - Ut) + B(t)\, e^{-qx}\cos(qy). \tag{5.6}$$

There are two boundary conditions satisfied at the interface. The first boundary condition is continuity, in which at the interface the normal components of the velocity are equal to each other. If we consider a small deviation from flatness, namely small A, then the velocity of the interface is given by:

$$V_1 = \frac{dx}{dt} = U + \dot{A}\cos(qy). \tag{5.7}$$

On the other hand, from the Stokes flow (5.3) and the pressure equation (5.6) above, we obtain another expression for the velocity which can be written as:

$$V_2 = U + \frac{b^2}{12\eta} qB(t)\cos(qy). \tag{5.8}$$

Equating equations (5.7) and (5.8), giving us a relation between B and $\dot{A}$:

$$B(t) = \frac{12\eta}{b^2 q}\dot{A}, \tag{5.9}$$

so that equation (5.6) becomes:

$$\Delta P_1 = \frac{12\eta}{b^2}\Big[UA - \frac{\dot{A}}{q}\Big]\cos(qy). \tag{5.10}$$

Equation (5.10) now gives us the pressure drop across the interface. On the other hand, the second boundary condition which the interface also has to satisfy refers to the pressure drop across the interface and is given by the Young-Laplace equation:

$$\Delta P_2 = -\gamma\kappa = -\gamma\frac{d^2x}{dy^2} = \gamma q^2 A\cos(qy). \tag{5.11}$$

with κ the curvature of the interface in the xy-plane. Now as $\Delta P_1 = \Delta P_2$, equations (5.10) and (5.11) can be equated to yield $\dot{A} = A\omega$ to find that:

$$\frac{b^2}{12\eta}\Big[\frac{12\eta U}{b^2} - \gamma q^2\Big]q = \omega(q). \tag{5.12}$$

Equation (5.12) gives the amplification factor or growth rate for a perturbation of wavevector q. A positive $\omega(q)$ shows that the disturbance will grow exponentially in size, leading to the formation of a stable finger, whereas a negative $\omega(q)$ will lead to a reduction in amplitude until the flat interface is formed again.

By considering the dimensionless wavenumber $\tilde{q} = WB^{1/2}q$, and the dimensionless frequency $\tilde{\omega}(\tilde{q}) = \omega(q)WB^{1/2}/\eta U$, equation (5.12) becomes universal:

$$\tilde{\omega}(\tilde{q}) = \tilde{q}(1 - \tilde{q}^2), \tag{5.13}$$

with $\eta = (\eta_2 - \eta_1)/(\eta_2 + \eta_1)$ being the viscosity ratio of the system. This allows us to find the critical wavenumber:

$$\tilde{q}_{crit} = 1 \implies q_{crit} = \frac{1}{WB^{1/2}} \tag{5.14}$$

and predict the fastest-growing mode:

$$\tilde{q}_{max} = \sqrt{1/3}\,\tilde{q}_{crit}. \tag{5.15}$$

Equation (5.14) defines the region of unstable modes, $0 \leq q \leq q_{crit}$, which clearly depends on the geometry of the cell, through the width W and the control parameter $1/B$. Conversely, the system is stable when $q > q_{crit}$.

5.3 Experimental details

We used a similar system and microfluidic set-up (illustrated in figure 5.2) as explained in chapter 4. A poly(methylmethacrylate) (PMMA) colloids and xanthan polymer mixture with interfacial tension $\gamma = 30$ nN/m and a viscosity contrast ratio $r = (\eta_2 - \eta_1)/(\eta_2 + \eta_1) = 0.4$ was used. As determined rheologically, the colloidal gas phase displays a shear-thinning behaviour at a critical shear rate of ~ 30 s^{-1}, which was above the maximum shear rate in the experiments ($U/b \sim 0.3$ s^{-1}). The channel was fabricated using the soft-lithography technique, where the width W was varied between 100 μm and 1 mm, and the thickness b was set at: 10, 14 and 17 μm. The less viscous colloidal liquid phase was allowed to push into the more viscous colloidal gas phase along the straight channel by using gravity. We use laser scanning confocal microscopy (LSCM) to record the development of the viscous fingers. Here, we focus on imaging the instability in the xy-plane (scanning point by point in the direction of the channel width at the focal plane equal to $b/2$). In contrast to the observation in the xz-plane (scanning in the direction of the channel thickness by changing the focal depth), the images in the xy-plane suffer less from effects such as a decrease in resolution, intensity drop due to scattering and shift of focus. No correction factor has to be applied when measuring the width of the finger.

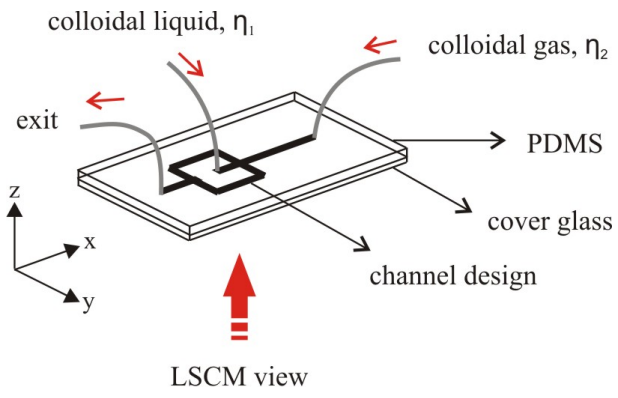


Figure 5.2: Schematic diagram of the microfluidic set-up where the less viscous colloidal liquid fluid is used to displace the colloidal gas phase. The spontaneous development of the viscous fingers along the straight channel was recorded using LSCM.

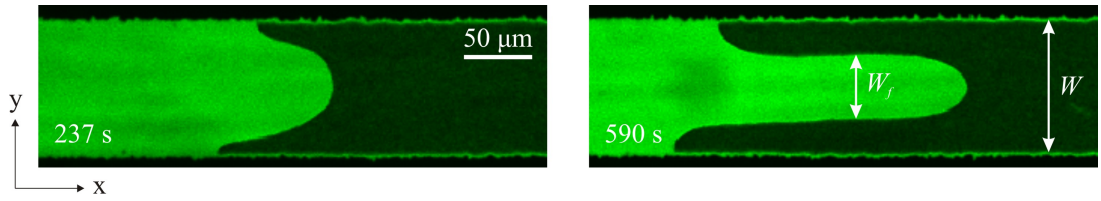


Figure 5.3: The spontaneous development of the Saffman-Taylor finger in the smaller channel at two different times. The finger relaxes to a steady state shape with width $\lambda_f = W_f/W$.

5.4 Lattice Boltzmann simulation

The simulations were performed independently by my colleague, Dr. I. Zacharoudiou (former D Phil student under supervision of Prof. J. M. Yeomans, Prof. D. G. A. L. Aarts, and Dr. A. A. Louis) at the Rudolf Peierls Centre for Theoretical Physics, University of Oxford.

Similar to chapter 4, the simulations were based on the free energy lattice Boltzmann method [150,151] (D3Q19 model) for binary fluid hydrodynamics. To elucidate our experimental observations, numerical simulations were performed by taking the actual channel geometry and fluid properties into account. Channel dimensions were, in simulation units, b = 50 - 100 and length L = 1000 - 2000, whereas the thickness of the wetting layer was $\zeta \sim 5$. The fluid viscosities were $\eta_1 = 0.017$, $\eta_2 = 0.036$ ($r = 0.36$). For the full details on how the simulations were run, we refer to [53] and references therein.

5.5 Results and discussion

5.5.1 Fingering in the xy-plane

Here we focus on the fingering in smaller channels between $W = 100$ μm up to 160 μm, where only a single finger is present. Figure 5.3 shows the spontaneous development of the viscous finger at two different times. Despite the ultralow value of the surface tension γ, it does act as a singular perturbation on the instability and a single finger width λ_f is selected, just as for molecular fluids [136]. The complete wetting situation is further illustrated by the presence of thick wetting layers on the side walls. As a result, the finger holds on to the walls and manages to follow the velocity of the tip of the finger at the lowest velocities.

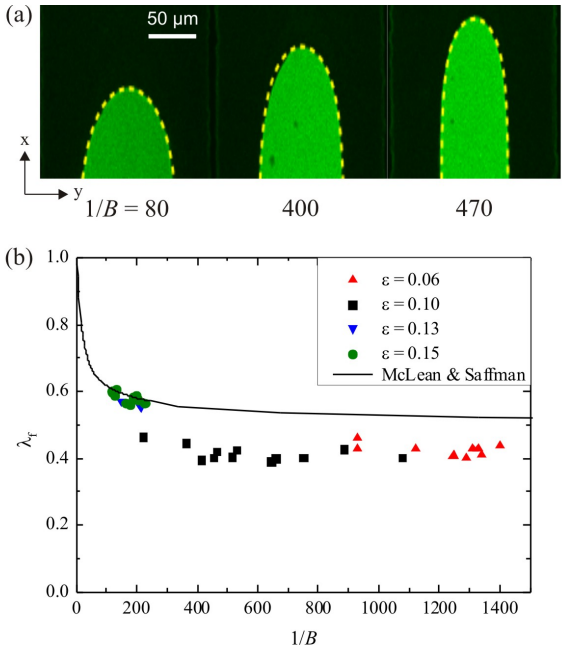


Figure 5.4: (a) LSCM images of a single finger at different modified capillary numbers $1/B$. The dashed/yellow curve follows from the Pitts equation [153]. (b) Scaled finger width λ_f as a function of $1/B$ for various aspect ratios ϵ. The full curve represents the McLean-Saffman solution [133].

As the finger advances in the channel, its tip velocity U slowly increases and the relative finger width λ_f decreases (see figure 5.4 (a)). Figure 5.4 (b) summarises results for λ_f as a function of the control parameter $1/B$. Different experiments for different aspect ratios ϵ collapse. The finger width goes below the 1/2 limit, which is also seen in experiments with molecular fluids [140] and recent simulations [126], albeit at much higher control parameters. Viscoelastic effects cannot be completely ruled out: shear-thinning fluids typically display finger narrowing (see, for example, [125, 148] and references therein). However, as noted above, typical shear rates in our microfluidics experiments lie well below the onset of shear thinning, as determined rheologically. For comparison, we also plot the theoretical curve by McLean and Saffman [133], which tends to 1/2 at large $1/B$. Finally, we observe that the finger shape is well described by the semi-empirical Pitts equation [153], which reads:

$$\cos\left(\frac{\pi y}{2\lambda_f}\right) = \exp\left(\frac{\pi x}{2\lambda_f}\right), \tag{5.16}$$

despite the complex nature of our fluids (see figure 5.4 (a) – dashed/yellow curve). Here, x and y measure the distance from the finger tip in units of half the channel width W.

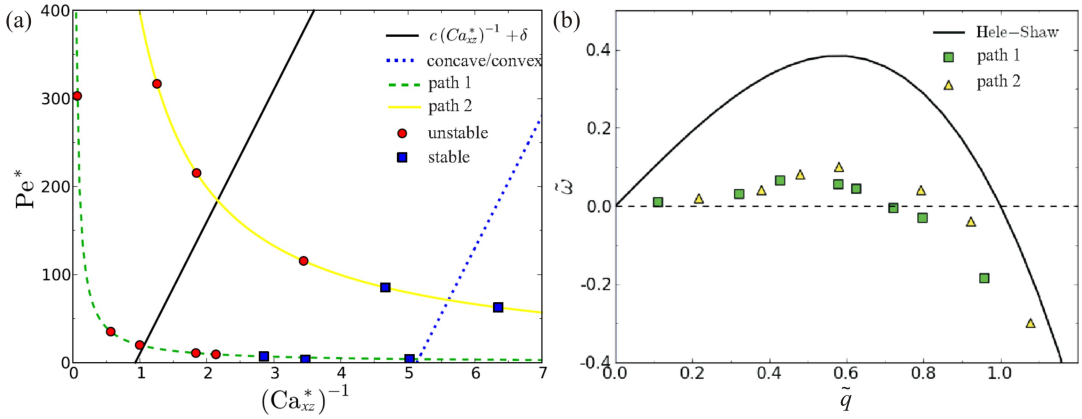


Figure 5.5: Results from lattice Boltzmann simulation [53]. (a) Plot for two different paths in the $(Pe^*, (Ca^*_{xz})^{-1})$-plane with $Pe^*/Ca^*_{xz} = 19.9$ (path 1) and 398.0 (path 2) for r =0.4 and $\epsilon = 0.24$. Red circles denote the results where perturbations grow and lead to viscous fingers in the xy-plane (exponential growth of the amplitude of the perturbations), and blue squares denote results with a negative growth rate. The solid black line corresponds to the onset of fingering in the xz-plane, while the blue/dash-dotted line indicates a flat advancing interface. (b) Dispersion relation for the two paths shown in (a). The solid line describes the predicted two-dimensional dispersion relation for Hele-Shaw flows.

5.5.2 Interplay between interfacial curvature in the xz-plane and xy-fingering

In chapter 4, we have shown the phenomenology of the interfacial curvature in the xz-plane as a function of the capillary number. The interface first advances as a concave meniscus. At intermediate velocities it moves with a convex meniscus. Finally, it develops xz-fingering. The latter is a situation in which the dynamic contact line becomes decoupled from that of the dynamic leading interface. Lattice Boltzmann simulations [53] reveal that the cross-over of the interfacial curvature is controlled by the capillary and Peclet numbers, and the viscosity contrast. Specifically, for a system with a viscosity contrast ratio $r = 0.36$, fingering in the xz-plane occurs for $Pe^* > c(Ca^*_{xz})^{-1} + \delta$, with constant $c = 150$ and offset $\delta = -140$, accounting for the width of the wetting layer ζ at the substrate (see figure 4.7 in chapter 4).

The above has important consequences for the viscous fingering instability in the xy-plane itself. In particular, simulations, which have been performed by Dr. I. Zacharoudiou and of which the main findings will be discussed here [53], reveal that viscous fingering in the xy-plane is suppressed when the meniscus in the xz-plane is concave. This is evident from figure 5.5 (a), where results based on 3D simulations were plotted for two systems with different values of

Pe^*/Ca^*_{xz} at viscosity contrast $r = 0.4$ and aspect ratio $\epsilon = 0.24$. Path 1 (dashed/green line): $Pe^*/Ca^*_{xz} = 19.9$, i.e. for systems with a diffuse interface, such as colloid-polymer mixtures, and Path 2 (yellow line): $Pe^*/Ca^*_{xz} = 398.0$. Red circles denote points where an interface that has been subjected to a small perturbation in the xy-plane led to viscous fingers, i.e. a positive growth rate such that the amplitude of the perturbation grows exponentially, rendering the interface unstable, while blue squares denote the points where the perturbation died out and, therefore, did not develop any fingering (negative growth rate – stable interface).

Furthermore, in order to show the dependency of the xy-finger selection on the Peclet number, the linear stability of an interface in the xy-plane is considered along the two different paths. As shown by simulations [53, 126], the role of the Peclet number is not so important for partial wetting, but it becomes more pronounced in the complete wetting case. As we have seen above, for the two-dimensional case, the universal dispersion relation is given by:

$$\widetilde{\omega}(\widetilde{q}) = \widetilde{q}(1 - \widetilde{q}^2) \tag{5.17}$$

where $\widetilde{q} = WB^{1/2}q$ and $\widetilde{\omega}(\widetilde{q}) = \omega(q)WB^{1/2}/\eta U$ are the dimensionless wavenumber and growth rate respectively. Figure 5.5 (b) shows a comparison between the universal dispersion relation and simulation results for the two paths, which reveal the dependence on Pe^*. For path 1 (green/squares), a first unstable mode is at $\widetilde{q}_{crit} \sim 0.7$, and for path 2 (yellow/triangle), $\widetilde{q}_{crit} \sim 0.85$. These are smaller than the 2D solution for the Hele-Shaw cell, $\widetilde{q}_{crit} = 1.0$, which indicates that the critical modified capillary number $1/B_{crit}$ for the onset of the Saffman-Taylor fingering is shifted to larger values for the case of complete wetting. Moreover, the growth rate for the complete wetting case is much smaller than the one predicted from the classical two-dimensional analysis.

When comparing the simulations with our experimental observations, a good qualitative agreement is achieved. From figure 5.4 (b), the Saffman-Taylor fingers are seen at $1/B \sim 150$, and appear to be suppressed below that, although it is very difficult to control very small velocities. We interpret this as follows: changing the curvature in the z-direction from concave to convex, then to xz-fingers, requires a much higher capillary number before viscous fingers in the xy-plane may be formed. To confirm this, we carried out an experiment in a channel with an aspect ratio $\epsilon = 0.15$ and kept the fluid-fluid flow velocity below the critical modified capillary number $1/B_{crit}$. As can be seen from figure 5.6, at typically low modified capillary

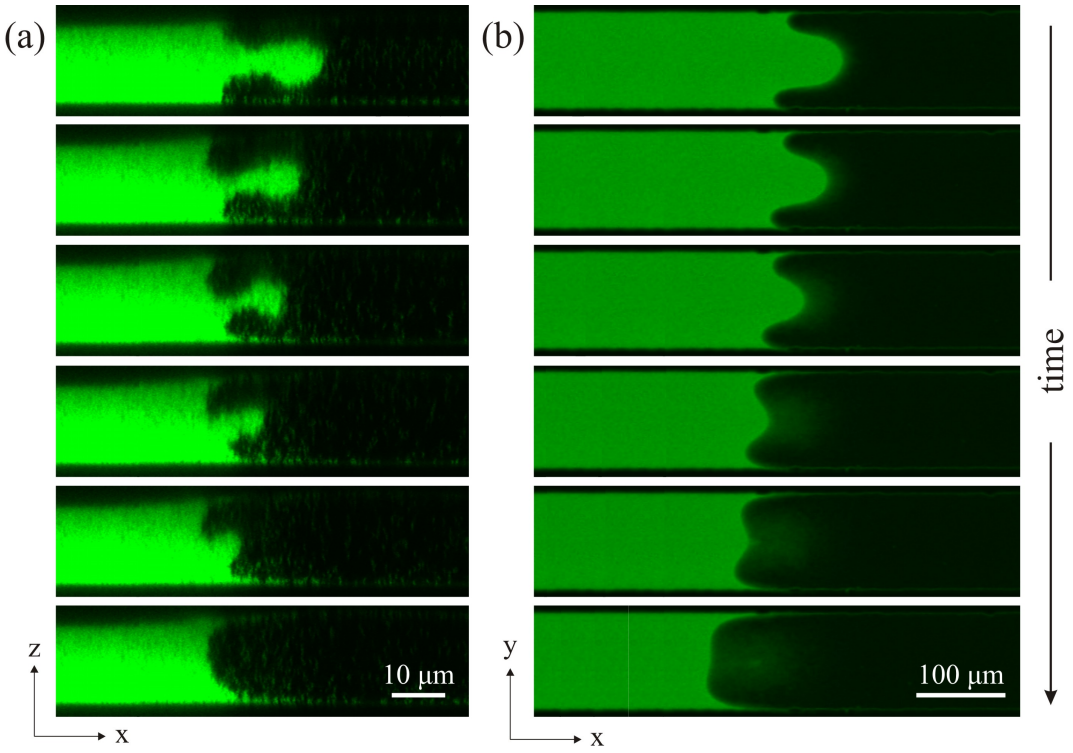


Figure 5.6: LSCM images showing at typically low capillary number $1/B = 50$, and changing the curvature in the z-direction (a) consequently suppressed the onset of the viscous finger in the xy-plane (b).

number $1/B \sim 50$, the interface in the xz-plane (panel (a)), which initially formed a penetrating structure (but with no steady finger shape), pulled the interface back as a concave meniscus. As a consequence, the Saffman-Taylor finger in the xy-plane (panel (b)) did not develop either and the perturbed interface became suppressed until finally a flat interface was formed again. However, the interface also moved backwards, showing the difficulty of working at such small velocities ($\leq$0.4 μm/s). This will require further experimental verification.

The above demonstrates that the onset of viscous fingering in the xy-plane indeed depends strongly on the behaviour of the leading interface in the xz-plane. The concavity of the interface in the xz-plane suppresses the onset of viscous fingering in the xy-plane. Therefore, it is unlikely to be possible to scale the finger width to the McLean-Saffman solutions [133] using just a modified capillary number. This underlines the importance of the third dimension in the viscous fingering instability.

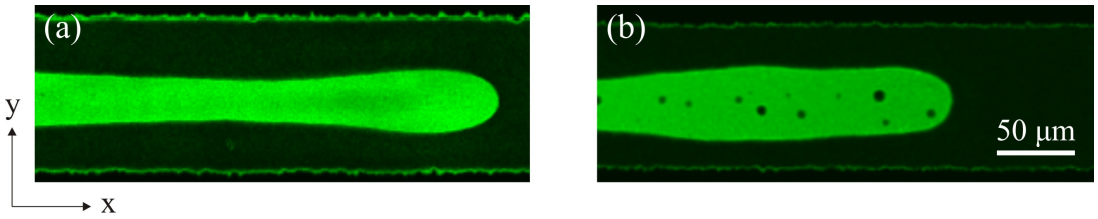


Figure 5.7: (a) Anomalous finger which widens at the tip. (b) Viscous finger with colloidal gas bubbles trapped inside.

5.5.3 Stability of viscous fingers

Here we discuss a number of important observations, some of which are different than in traditional viscous finger experiments.

(i) Single finger

We shall now discuss the stability of the viscous fingers in our microfluidic channels. Figure 5.7 (a) shows propagation of a single finger in a channel of an aspect ratio $\epsilon = 0.10$, which at a later time ($1/B \sim 700$) displays anomalous behaviour, where the tip widens. This deviation from the stable Saffman-Taylor finger might be due to the existence of the thin wetting film in the z-direction. Alternatively, Lindner *et al.* [125, 161] have shown that a high normal stress by non-Newtonian fluids increases the thickness of the thin film. This then leads to an extra pressure within the thin film between the advancing xz-finger and the cell walls, which causes widening of the finger width. However, our fluids do not show such a normal stress (see chapter 2).

In other cases, we observed a finger with colloidal gas bubbles trapped inside (see figure 5.7 (b)). The gas bubbles display Brownian motion and move at a faster rate than the tip of the finger. This may be relevant in the oil industry [162], where the bubbles would represent the oil phase and are carried to the exit more quickly.

Moreover, we also observe tip splitting on a single finger when a considerable perturbation was present in the channel, as shown in figure 5.8. Tip splitting has been discussed intensively: beginning with the stability analysis of Saffman and Taylor [117] for the zero surface tension case, followed by numerical calculations of McLean and Saffman [133] with the inclusion of surface tension, it showed that the finger was linearly unstable. Then, De Gregoria and Schwartz [163]

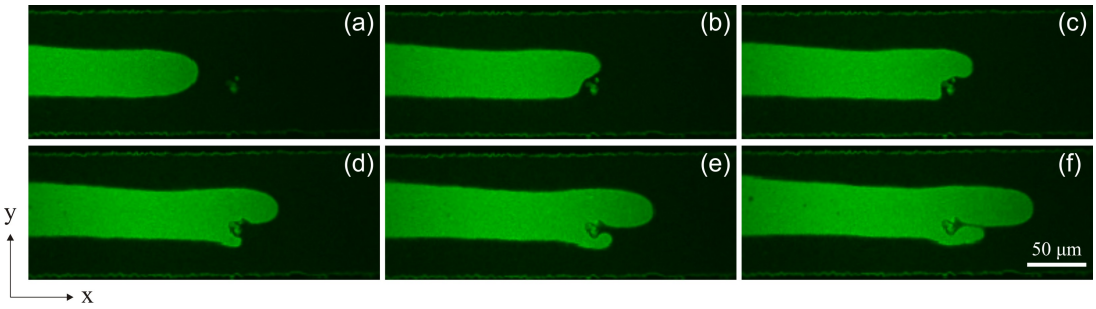


Figure 5.8: Tip splitting effect observed on a single viscous finger by a perturbation in the microfluidic channel.

showed from computer simulations that the onset of the tip splitting instability depended upon the amplitude of the imposed perturbation; the attribution of noise clearly played an important factor in the tip splitting. Kessler and Levine [164] suggested that the tip splitting occurs if the amplitude of the disturbances is large enough, in contrast with Liang [165], where the tip splitting is observed for very low $1/B$, the regime in which the dominant finger should be linearly stable. Bensimon [166] further analysed the nature of the instability and found an exponential relation between the amplitude of noise necessary to destabilise the finger and the parameter $1/B$, thus further suggesting that the system is extremely sensitive to changes in velocity as far as the tip splitting is concerned.

From the experimental side, Park and Homsy [167] were the first reported that $1/B > 100$ for the tip splitting to be observed. Tabeling *et al.* [140] then showed a delay in the onset of splitting to $1/B = 3000$ by reducing the noise in the experiments. They also showed that the critical value of the noise was weakly dependent on the velocity below the critical threshold region, which is in conflict with theory. However, when comparing the shape of the unstable fingers between experiments and theory, qualitatively a very similar pattern was obtained, see ref [119] in which a detailed comparison is made. So far, the critical conditions for onset of tip splitting are still not fully understood, but it is proposed to be dependent on the strength of the applied disturbance [163].

Recently, Chevalier *et al.* [168], using a non-Brownian suspension, showed that the individual grains provide controlled noise and produce a perturbation at the interface. The perturbed interface where the amplitude is proportional to the grain size, then initiated the destabilization of the finger, leading to a much more controllable threshold of the tip splitting instability. In our set-up, the tip splitting can be further studied by, e.g. designing and fabricating channels which

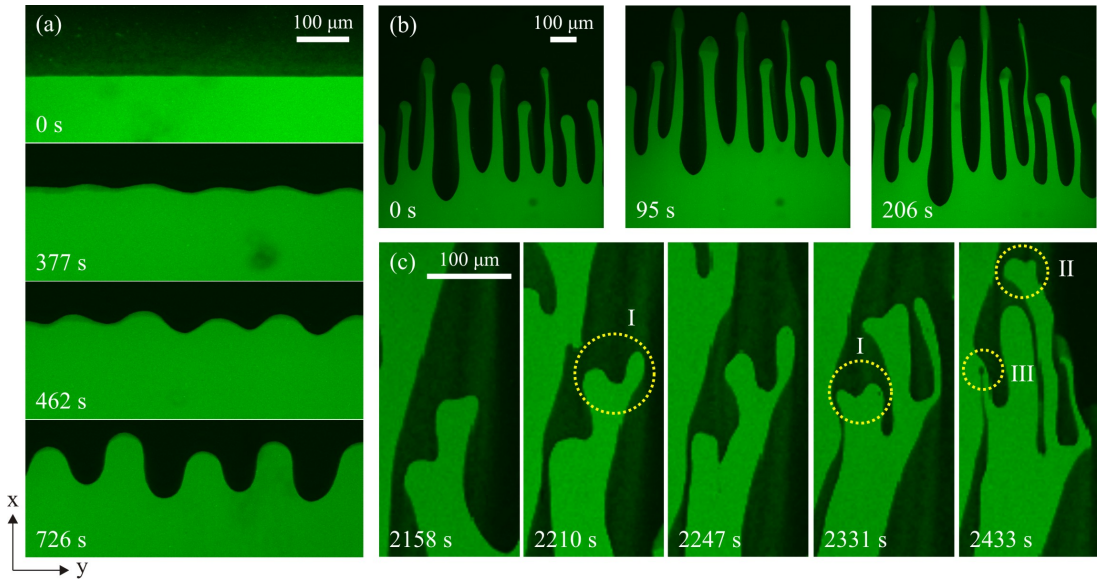


Figure 5.9: LSCM images of the viscous fingering in a wide channel ($W = 1$ mm) where many fingers develop. At later times (b) the fingers become very long and thin and (c) under certain conditions we observe tip splitting and side branching effects.

contain pillar/small dots to initiate destabilisation of the interface. Moreover, the interface itself provides considerable noise in the form of thermal fluctuations and it is still an open question as to whether tip splitting may occur at very high $1/B$ as an intrinsic property of the fluids.

(ii) Multiple fingers

Figure 5.9 shows images of the viscous fingering instability in a wide channel ($W = 1$ mm) that can accommodate many fingers. The fingering has all of the characteristics of the Saffman-Taylor instability (figure 5.9 (a)). The further development of the fingers, however, where they become very thin, is very different from in the normal case and again has to do with the wetting boundary condition (figure 5.9 (b)). They also show tip splitting (figure 5.9 (c) - I) and side branching (figure 5.9 (c) - II) as in the classical case. But they go on and show coalescence of neighbouring fingers, where the fingers can re-join and trap the colloidal gas phase in between (figure 5.9 (c) - III). These effects will dynamically change the interfacial contact area, which may be of interest for a chemical reaction in microfluidic devices [128].

5.6 Conclusion and outlook

In summary, we have studied the development of viscous fingering in the xy-plane in the limit of ultralow interfacial tension. A single finger width is selected as a function of $1/B$ and the finger contour is well described by the Pitts equation despite the ultralow interfacial tension. We explained the importance of the third dimension, which an often neglected ingredient of the instability. The complete wetting behaviour displayed by our colloidal fluids leads to rich behaviour. When the interface curvature in the xz-plane is concave, fingering in the xy-plane is suppressed, suggesting that $1/B$ does not capture the fingering mechanism that selects the width of the finger.

We discussed the rich stability behaviour of the viscous fingers in which the anomalous, tip splitting, side branching and coalescence between neighbouring fingers may be exploited to enhance recovery of the crude oil industry. Furthermore, the small lengthscales in microfluidics cut off any inertial effects, which poses limitations on how efficiently fluids can mix. For immiscible fluids, where wetting effects play a dominant role, this becomes even more pronounced. Here, we have shown that the interfacial contact area can be increased considerably by exploiting the Saffman-Taylor instability. A further design may further make use of the related Rayleigh-Taylor instability, which is based on density mismatches between fluids [169–171]. In figure 5.10, we present a preliminary experiment of the Rayleigh-Taylor instability in a Y-shape channel (a), where the colloidal liquid phase (top) displaced the colloidal gas phase (bottom) by gravity (b). An initial flat interface becomes mechanically unstable and develops sinusoidal disturbances which continuously grow, whereby forming finger-like structures. This clearly demonstrated that these instabilities with a suitable cell design can be exploited to mix complex fluids in microfluidics devices.

In the next chapter we show that driving the flow of the colloidal fluids at higher velocities (above the meandering motion threshold) leads to the formation of a liquid jet, which then destabilises and shortly emits a series of droplets. This new instability allows us to study the related dynamic contact line problem in great detail.

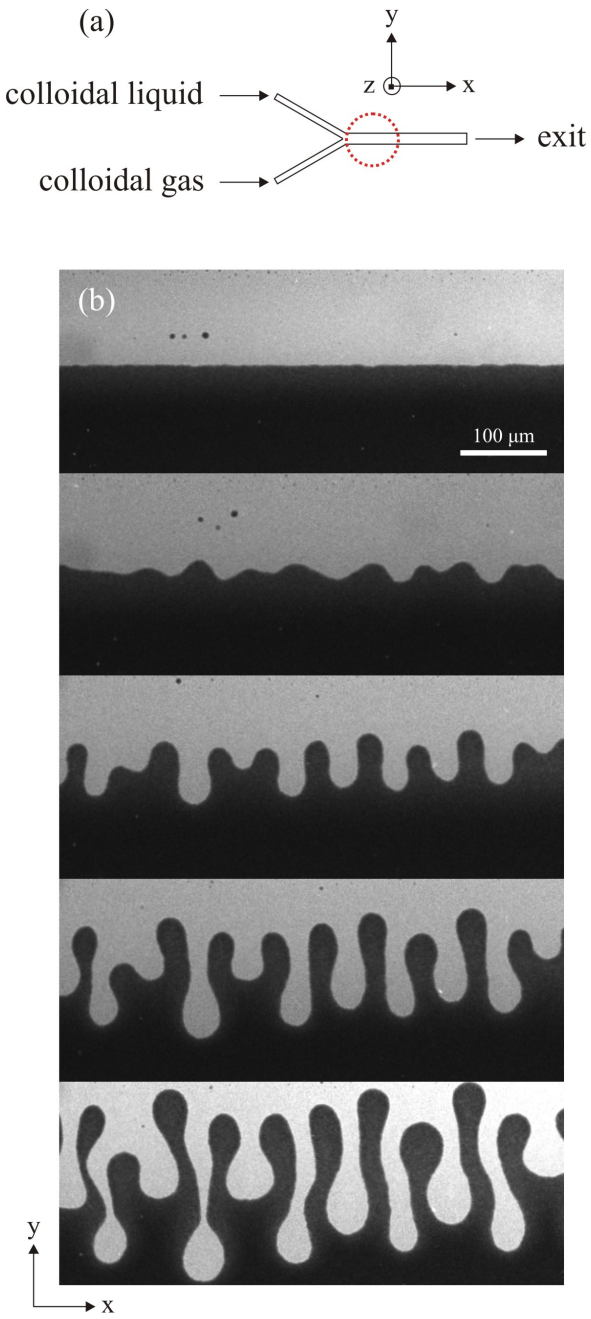


Figure 5.10: (a) Y-shape microfluidic channel. (b) LSCM images of the Rayleigh-Taylor instability imaged in the area indicated by the dashed red circle, where the colloidal liquid phase (top) displaced the colloidal gas phase (bottom) by gravity. Gravity is along the negative y-axis.

Acknowledgments

It is a pleasure to thank Gareth J. Davies for pioneering experiments, I. Zacharoudiou for the simulation effort, and Rodrigo Ledesma-Aguilar, Daniel Bonn, Roel Dullens, Ard A. Louis, Sebastien Moulinet, Denis Bartolo and Julia M. Yeomans for useful discussions.

Chapter 6

Drop spitting instability in superconfinement

ABSTRACT

In this chapter, we study the dynamics of fluid fronts in *superconfinement*, where the gap between the intrinsic slip length and device lengthscales becomes very small by exploiting the Saffman-Taylor instability described in previous chapters. Here, we find that the strong coupling between contact line friction and geometric confinement gives rise to a new stability regime where the maximum speed for a stable moving front exhibits a distinctive scaling with the cell thickness. Unstable fronts develop into drop-emitting jets controlled by the degree of confinement through thermal fluctuations. Using a combination of laser scanning confocal microscopy and diffuse interface hydrodynamic theory, we directly quantify the contact line slip length. Our combination of work constitutes a first step towards understanding and controlling the motion of fluid fronts in systems governed by a lengthscale overlap.

6.1 Introduction

Successful attempts to harness the motion of fluids at small scales in the last decade have resulted in the emergence of micro- and nanofluidics as mainstream source fields for novel technologies [64, 172, 173]. The impact of the new applications developed is indisputable, and covers a wide range of fields, from health [174] to materials science [175]. An inevitable consequence of further miniaturisation is that the size of the devices containing the fluids becomes comparable to the intrinsic lengthscales of the fluids themselves. As a result, the central assumption of classical hydrodynamics of clearly separated lengthscales no longer holds. In this regime, which we call *superconfinement*, the physical response of the system is determined by the interplay between the fluid and system lengthscales through a strong coupling between the local friction offered by the fluids and the geometric confinement of the solid boundaries. Understanding the way fluids behave in this regime is crucial to developing applications where solid-fluid interactions can be exploited to manipulate extremely small volumes of fluid.

One of the central problems in small scale solid-fluid interactions is understanding the dynamics of contact lines [176,177] and their connection to the stability of moving fronts. Despite their familiarity and widespread occurrence in everyday life, this has proven a challenging task. By definition, a fluid front advancing on a solid violates the stick boundary condition of classical hydrodynamics [178], which dictates that the fluid is at rest with the solid at the fluid-solid boundary. This apparent contradiction is an artefact of the classical hydrodynamic theory, which relies on a sharp-interface description and, therefore, does not take into account the molecular interactions that allow the contact line to move [179]. From a macroscopic perspective, these interactions result in the slippage of the fluid past the solid over a characteristic contact line slip length. The interplay between the intrinsic contact line slip length and the characteristic lengthscale of the flow is crucial for the stability of advancing fronts; beyond a maximum speed of forced wetting (or dewetting) [180], the contact line lags behind, and the fluid-fluid interface is entrained by the solid. While this process has been studied experimentally in a variety of configurations [181–187], direct measurements of the coupling between contact line and front dynamics in molecular fluids, e.g. water and air, remain elusive. This complication stems from the extremely different lengthscales involved in traditional set-ups, which span several orders of magnitude (from nanometres at the interfacial scale, to, e.g. tens of microns for the size of the front in a microfluidic channel).

Motivated by the importance of front stability at small scales, here we analyse the effect of superconfinement on the stability of an advancing front and determine whether the lengthscale overlap associated with superconfinement can be used to rationalise and control the stability of forced fronts. To address these questions, we have carried out microfluidic experiments of forced fronts using demixed colloid-polymer phases, where the thickness of the interface is typically of the order of microns. This allows us to access the superconfined regime in micron-sized channels. As opposed to more traditional set-ups, the large interface scale in our experiments offers the additional advantage of directly visualising the front and the contact line using confocal microscopy [10].

To begin, we first described the experimental set-up used in this chapter (section 6.2). This is followed by section 6.3, where we present and discuss the results. The first part will be focused on the entrainment of the fluid dynamics and the second part will discuss the drop spitting regime. Finally, we end with a conclusion in section 6.4.

6.2 Experimental set-up

We used a similar system and set-up as described in the previous chapter. The cross microfluidic channel as illustrated in figure 6.1 (a) was fabricated in poly(dimethylsiloxane) (PDMS) elastomer (chapter 2). The rectangular channel has a fixed width $W = 110$ μm (along the y-axis) and variable thickness $H = 8$, 10, 14, and 17 μm (along the z-axis). The system consisted of fluorescently labelled poly(methylmethacrylate) (PMMA) colloids and xanthan polymer dispersed in water. At high enough polymer concentrations, the mixture phase separates spontaneously in a colloid-rich polymer-poor (liquid) phase in coexistence with a colloid-poor polymer-rich (gas) phase due to the depletion interaction mediated by the polymers [24, 28, 29]. For the statepoint used in our experiments (point I in figure 2.2, chapter 2), the interfacial tension $\gamma = 30$ nN/m, the capillary length $L_c = 14$ μm, and the interface thickness $\xi \sim 1.2$ μm, as determined from the capillary wave spectrum. The viscosities of the separated phases were measured on a TA AR-G2 rheometer. Both viscosities remained in the Newtonian regime for a wide range of applied shear rates, giving $\eta_L = 7$ mPa s for the colloidal liquid phase and $\eta_G = 15$ mPa s for the colloidal gas phase.

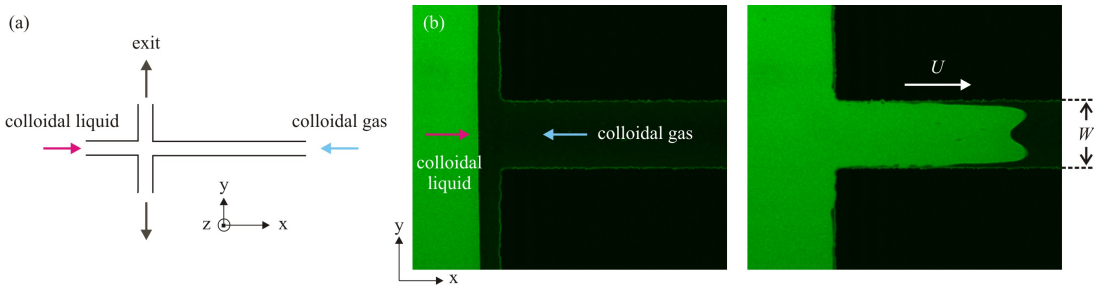


Figure 6.1: (a) Schematic diagram of cross microfluidics channel with width W and thickness H. (b) Flow of colloidal fluids; the low viscous displacing liquid is forced into the high viscous gas phase along the straight channel where the initially flat interface (left) develops into fingering by virtue of the Saffman-Taylor instability (right).

After the phase separation had been completed, we carefully isolated the two phases; the two fluids were subsequently injected into the microfluidic channels, at which point they were at coexistence again (see figure 6.1 (b)). A flat interface of liquid and gas phases was formed at the centre of the cross-channel (left). Then, the displacing colloidal liquid phase was controlled to displace the more viscous colloidal gas phase along the straight channel (right). The driving pressure between the inlet and outlet of the channel was controlled by gravity. The resulting flow instability was imaged by means of laser scanning confocal microscopy (LSCM, Zeiss Exciter) in three dimensions, which records the fluorescence of the colloids.

6.3 Results and discussion

In this section, we will present and discuss the results. We start with section 6.3.1, the instability of fluid fronts in microfluidics, which we show can be controlled through the geometri of the confinement. This is followed by section 6.3.2, the emission of droplets, where the size and rate of snap-off will be the focus of the discussion.

6.3.1 Fluid fronts instability induced by superconfinement

The displacing of the more viscous colloidal gas phase by the less viscous colloidal liquid phase in the rectangular microfluidic channel spontaneously induces the formation of viscous fingers by virtue of the Saffman-Taylor instability (figure 6.2 (a)) (see also chapters 4 and 5). We observe that there is a critical velocity at which the velocity at the contact line is less than the velocity at the finger tip. This leads to the different fluorescent intensities between the front and the

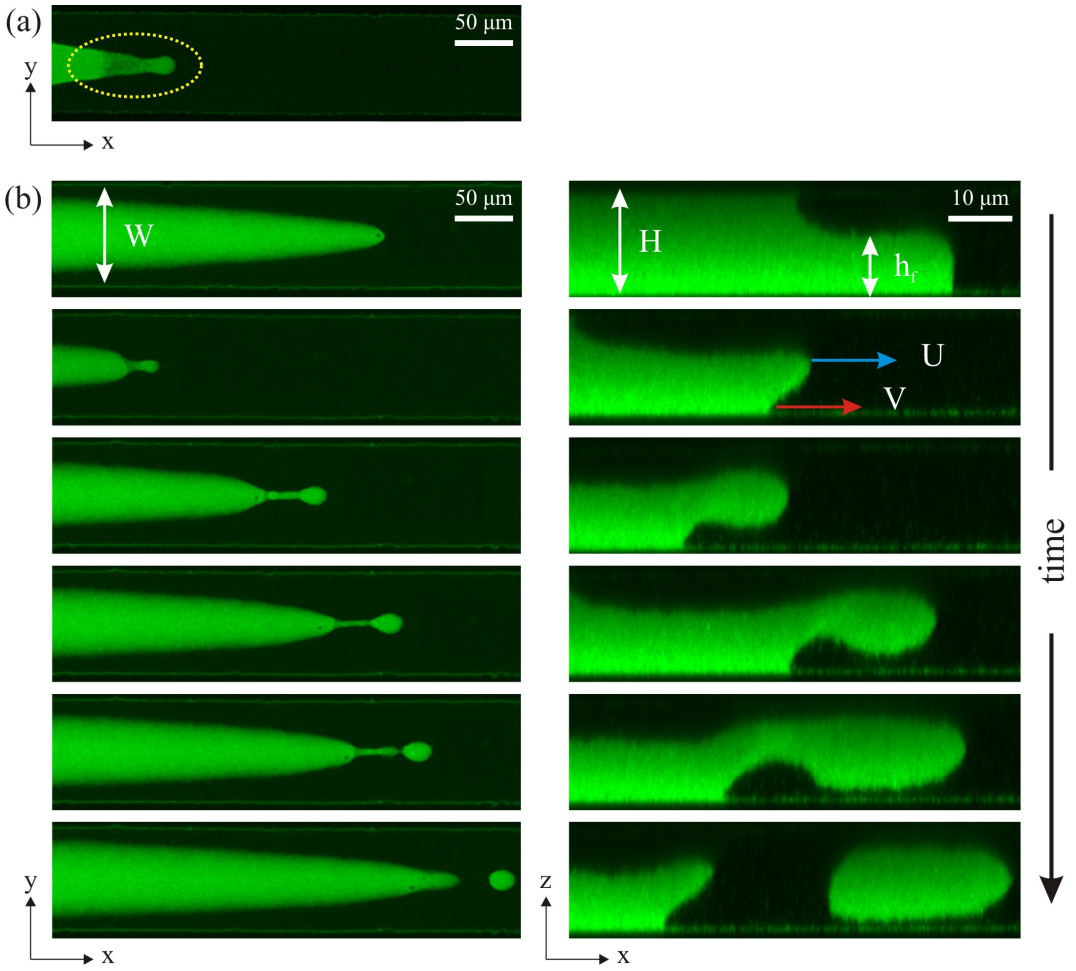


Figure 6.2: Destabilisation of dynamics fluid front leading to drop spitting due to a mismatch in velocity between contact line and its front ($V < U$), which can be noticed by the different fluorescent intensities in the images (see area in the dashed/yellow circle); (left) corresponds to the projection in the xy-plane (top view of the channel with width W) and (right) corresponds to the same configuration in the xz-plane (lateral view of the channel thickness H).

bulk finger (see area in the dashed/yellow circle) and is ultimately related to the mechanism with which the contact line moves over a solid surface.

To further probe this idea and understand the phenomena, we imaged the instability process in three dimensions. Figure 6.2 (b) shows three-dimensional LSCM images of the formation of the thin film in the microfluidic channel, which subsequently destabilised, leading to drop emission; (right) corresponds to the projection in the xz-plane (lateral view of the channel thickness H) and (left) corresponds to the same configuration in the xy-plane (top view of the channel with width W). Note that the interface roughness is visible in our optical microscopy images. In chapter 4, we have shown that at a critical velocity a thin film penetrates from the

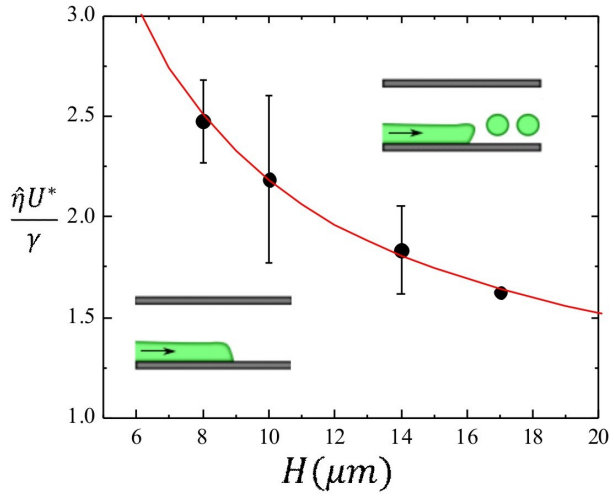


Figure 6.3: Critical capillary number as a function of channel thickness to onset the destabilisation process. A symbol denotes the experimental data and a red line represents the theoretical fitting (equation (6.9)).

centre of the interface and develops into an xz-finger. The finger experiences a meandering motion at higher driving velocities where it starts to make contact with the walls before it continues to move into the centre of the channel again. Beyond that critical point, due to a comparable lengthscale of L_c with the channel thickness H in our experiments, gravitational effects force the finger to adhere onto the bottom of the wall. This creates a thin film of thickness h_f, which takes up approximately half of the channel thickness (see top row of the images).

Upon increasing the driving pressure gradient, the interface reaches a well-defined maximum speed U^*, at which point entrainment occurs and initiates the destabilisation process. Henceforth, the contact line of speed V moves slower than the leading front of speed U (second row). The mismatch gives rise to the development of a liquid jet whose neck thins and eventually collapses, emitting a droplet (last row). Once the drop has been emitted, a new liquid jet develops and breaks at the neck, releasing the subsequent drop, thus making the drop emission process periodic. We plot the critical driving velocity U^* as a function of the channel thickness H in figure 6.3. The critical speed decays as the channel thickness increases, showing a strong dependency of confinement on the onset of the entrainment of the liquid film.

To understand the interplay between the contact line and front dynamics that leads to fluid entrainment, we need to account for the fluid dynamics at lengthscales comparable to the interface thickness. However, in this regime, classical models relying on the assumption of large-scale separation are no longer valid. Instead, we approach this problem using a diffuse-interface

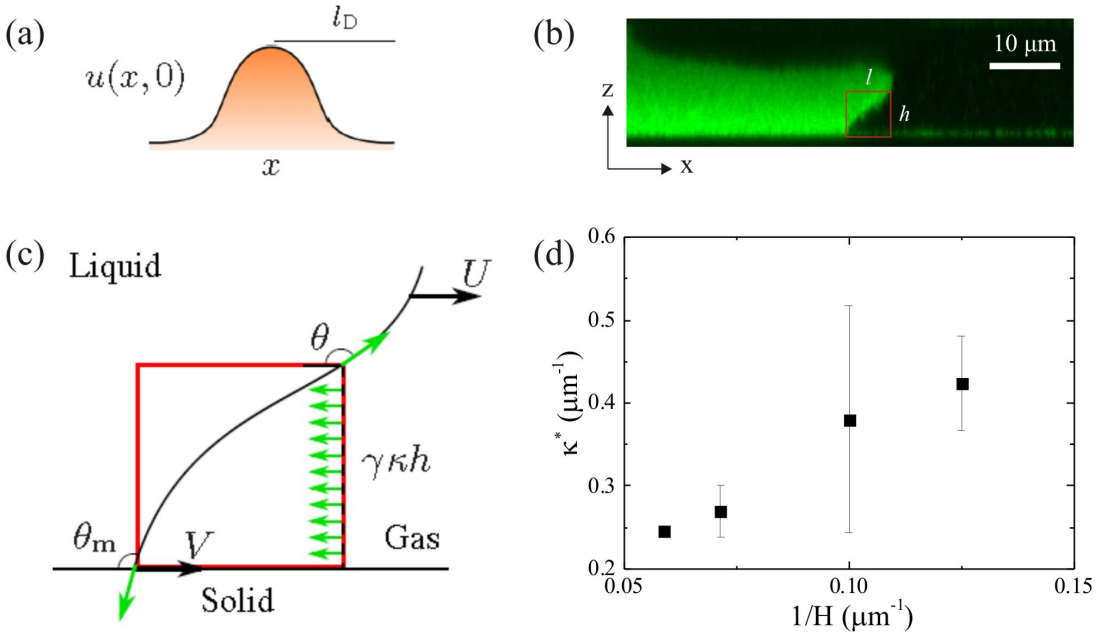


Figure 6.4: (a) Schematic of the slip velocity profile, l_D close to the contact line. (b) Interface configuration at the critical speed just before drop emission. (c) Schematic representation of the interface configuration close to the contact line (amplified from frame b). (d) Scaling of the curvature of the interface at the critical point with the channel thickness.

hydrodynamics description. Within this framework, it is proposed that the relaxation of the stick boundary condition at the contact line is controlled by the diffusion of fluid molecules past the solid over an intrinsic lengthscale l_D due to gradients in the chemical potential [188, 189]. From the point of view of macroscopic hydrodynamics, l_D acts as a localised contact line slip length. This is different from the Navier slip length, which characterises weak deviations from the stick boundary condition at a solid-fluid interface.

The existence of the slip profile at the contact line has been shown using molecular dynamics and diffuse-interface simulations [190]. Moving along the solid-fluid interface, the tangential velocity, $u(x, z = 0)$, shows a slow (algebraic) decay with an increasing distance from the contact line, x (see figure 6.4 (a)). Both approaches show that l_D is larger, of at least one order of magnitude, than the interface thickness and the Navier slip length. This was also confirmed by lattice Boltzmann simulations of a diffuse interface run by Dr. I. Zacharoudiou [53], where he found a large slip region for the fluid velocity profile at the contact line, when compared to the velocity profile for Poiseuille flow. The contact line slip is lost at large distances from the contact line (compared to l_D), where the bulk slip, characterised by the Navier length, is recovered. In case of proper lengthscale separation, i.e. $H \gg l_D$, the velocity profile away from the solid-fluid

boundary will show the characteristic pattern of flow near a corner [191].

In our experiments, the front is driven by a fixed pressure gradient, which results in a strong deformation of the interface as shown in figure 6.4 (b). To describe the dynamics of the contact line, we used continuum hydrodynamic formulation by combining the Cahn-Hilliard convection-diffusion equation, which naturally describes the diffusion at the contact line region, with the Navier-stokes equation for an incompressible fluid, $\nabla.v = 0$:

$$\frac{\partial \phi}{\partial t} + v.\nabla\phi = M\nabla^2\mu \tag{6.1}$$

$$\nabla P = \eta\nabla^2 v + \phi\nabla\mu. \tag{6.2}$$

Here, v and P are the fluid velocity and pressure, respectively, μ is the chemical potential, M is a diffusive transport coefficient, η is the local dynamic viscosity and ϕ is the local concentration variable. The additional term on the right of equation (6.2) arises from the diffuse interface. This is converges to the Laplace pressure in the sharp-interface limit, *i.e.*, $\mu \to \gamma\kappa$, where κ is the interface curvature.

The theory below was first derived by Dr. R. Ledesma-Aguilar, post-doctoral research assistant with Prof. J. M. Yeomans at the Rudolf Peierls Centre for Theoretical Physics, University of Oxford.

Theory of front dynamics in superconfinement (i): contact line

We first focus on the contact line itself. Integrating the above equations over a scaling lengthscale l_D, where the slip occurs, we obtain a maximum value of the velocity $V \sim M\mu_{max}/l_D$ and chemical potential $\mu_{max} \sim \eta V/l_D$ of the interface. Equating μ_{max} from these relations gives $l_D \sim \sqrt{M\eta}$, which leads to the contact line friction force:

$$F_f \sim \hat{\eta} V \zeta. \tag{6.3}$$

The friction force arises from the sliding of both liquid and gas molecules past the solid and, thus, depends on their speed and average viscosity, $\hat{\eta} = \frac{1}{2}(\eta_G + \eta_L)$. The friction coefficient $\zeta = \xi/l_D$ characterises the extent to which slip occurs, and is fixed by l_D.

On the other hand, considering the tension forces acting at the triple line leads to the unbalanced Young's force:

$$F_Y = \gamma(\cos\theta_e - \cos\theta_m). \tag{6.4}$$

Note that Young's force depends purely on the geometry of the interface through the microscopic contact angle, θ_m (figure 6.4 (c)), and is controlled by the solid-liquid, solid-gas and liquid-gas tension forces acting at the contact line. Combining F_f and F_Y sets the dynamics of the microscopic contact angle as [192]:

$$\cos\theta_m = \cos\theta_e - \frac{\hat{\eta}V}{\gamma}\zeta \tag{6.5}$$

For static interfaces $V = 0$ and the microscopic angles reach their equilibrium value, θ_e.

Theory of front dynamics in superconfinement (ii): capillary versus viscous term

The speed of the front, on the other hand, is set by a global balance between viscous and capillary forces acting on the fluid wedges that meet at the contact line, whose size is comparable to the size of the front (see figure 6.4 (c)). We can write the force balance per unit length of the contact line as:

$$\int^{l} dx \int^{h} dz \nabla P = \int^{l} dx \int^{h} dz \eta \nabla^2 u \tag{6.6}$$

where l and h are the local length and thickness of the wedges. The net driving capillary force (first term) follows after integrating the gradient of the Laplace pressure, $\sim \partial_x \gamma\kappa$, from the contact line (located at $x = 0$) over the size of the wedge. Since the size of the wedge in our experiments is of the order of l_D, we can write:

$$\gamma\kappa l_D + \gamma(\cos\theta_m - \cos\theta) \tag{6.7}$$

where we have used the relations $\kappa = \partial_x^2 h(1 + (\partial_x h)^2)^{-3/2}$ and $\cos\theta = -(1 + (\partial_x h)^2)^{-1/2}$; κ and θ are the curvature and bending angle of the interface, respectively. It consists of the Laplace pressure force exerted by the fluid lying in front of the wedge, and of two tension forces pulling on the corners (depicted as arrows in figure 6.4 (c)). The effect of the capillary force is to push the gas in front of the contact line and to pull on the liquid lying behind it.

The last term in equation (6.6) corresponds to the resisting viscous forces originating from the flow within the gas wedge and the surrounding liquid[1]. This term contains the scale dependence of the flow: for molecular fluids, e.g. water, air, where $\xi < l_D \ll h$, this scales as $U \log(h/\xi)$ [177]. However, in superconfinement, $l_D \simeq h$, which leads to $\nabla^2 u \sim U/l_D^2$ [192]. Therefore, the viscous terms in equation (6.6) scale as ηU. A more detailed analysis taking both fluids into account as well as the wetting layer thickness leads to $\hat{\eta} U$.

Theory of front dynamics in superconfinement: onset of the instability

Combining the scaling of the viscous-capillary term (6.6) with the contact line motion expressed in equation (6.5), we find:

$$\kappa l_D + \cos\theta_e - \cos\theta \simeq \frac{\hat{\eta} V}{\gamma}\xi + \frac{\hat{\eta} U}{\gamma}. \tag{6.8}$$

For stable fronts, the contact line speed matches the front speed ($V = U$). The resulting interface shape is characterised by κ and θ, as dictated by equation (6.8). For unbounded fronts, where $h \ll H$, the curvature of the profile near the contact line is controlled by the diffusive lengthscale, *i.e.* $\kappa \sim 1/l_D$. However, in our microfluidic experiments the fluids were strongly confined, $h \simeq H$. The interface curvature is set instead by the thickness of the channel and obeys $\kappa \sim 1/H$, as shown in figure 6.4 (d).

At the onset of entrainment the contact line speed reaches a maximum, $V = U = U^*$, and equation (6.8) gives the condition:

$$\frac{\hat{\eta} U^*}{\gamma} \sim \frac{l_D}{\zeta + l_D}\left(\frac{l_D}{H} + \cos\theta_e - \cos\theta^*\right) \tag{6.9}$$

where $\hat{\eta} U^*/\gamma = Ca^*$ and θ^* are the critical capillary number and critical bending angle. This equation (6.9) reflects the effect of superconfinement on the coupling between the contact line and front dynamics, and predicts the distinctive algebraic decay of the critical speed with channel thickness measured as shown in figure 6.3 (red line). This contrasts with previous predictions of entrainment in free [193] and confined systems [194], where sharp lengthscale separations give rise to a logarithmic decay.

Our prediction of the onset of entrainment can be used to extract the contact line slip length

[1]The effect of the prewetting layer, of thickness $\sim \xi$, is absorbed into the last term.

by comparing to our experiments. Since equation (6.9) holds up to the critical velocity, we have verified it for $\theta = 90°$, which is close to the critical θ^*. However, given the transient nature close to criticality, we have used 90°, which is well defined. A best fit of the experimental data shown in figure 6.3 to equation (6.9) gives $l_D \sim 12$ μm. This value exceeds the interface thickness by one order of magnitude. This ratio is consistent with molecular dynamics simulations of fluids moving on smooth surfaces [190], reflecting the scaling of fluctuations of the interface in the colloid-polymer mixtures which lie in the range of hundreds of nanometres to microns. To our knowledge, this is the first time that the contact line slip length has been measured experimentally. Since both ξ and l_D are intrinsic properties of the system, their values can be used to estimate the friction coefficient of the contact line, $\zeta \simeq 0.1$. Recently, it has been shown that small values of ζ (compared to unity) can strongly reduce the large-scale stability of forced fronts by fixing the shape of the interface at small scales, which in turn increases the viscous friction coming from sharp corner flows [193]. Such an interplay between the contact line and bulk friction can give rise to different entrainment regimes depending on the wetting properties of a given solid-fluid system. Using superconfinement to measure contact line friction can therefore prove very useful to exploit surface specificity in controlling front dynamics.

6.3.2 Jet formation and drop emission

Beyond the onset of entrainment, drops are emitted periodically as shown in figure 6.5 (a), where the size and rate of snap-off can be controlled by choosing the channel thickness (figure 6.5 (c-e)). This process begins with the slow-down of the contact line relative to the front, which triggers the growth of a liquid jet from the contact line. For small H, when the jet and interface thickness are comparable, the jet develops a thinning neck that connects to a nascent drop, which is then released (figure 6.5 (b)). Because the speed of the front is kept above the entrainment threshold, a subsequent jet forms and further emitting drops at a constant rate.

The volume of the drop, as shown in figure 6.5 (d) as a function of the channel thickness, is determined by the snap-off process, which sets the typical fluid volume flowing into the jet (of thickness $\sim h_f$) over the snap-off time t_s, i.e.:

$$v_{jet} \simeq \frac{\pi}{2} h_f^2 (U - V) t_s. \tag{6.10}$$

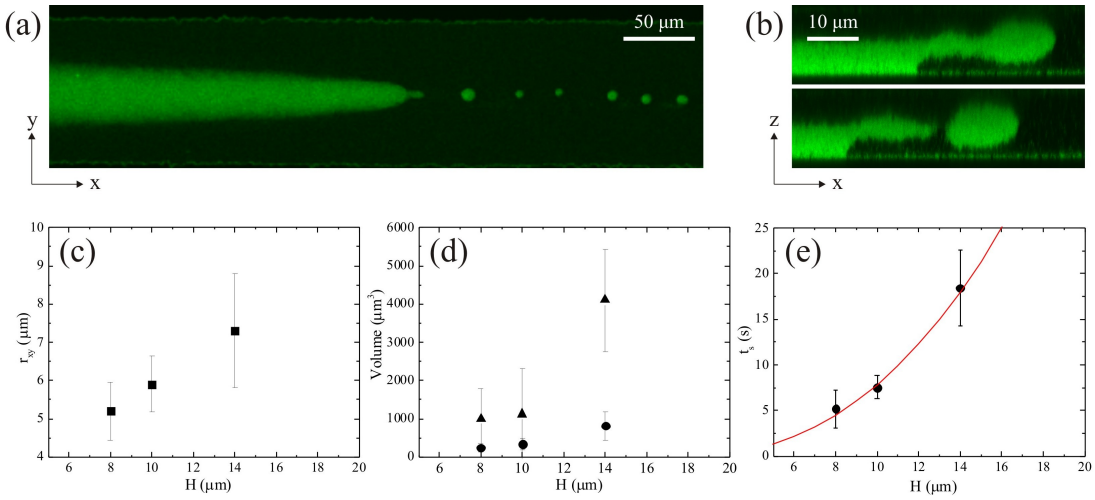


Figure 6.5: (a) Periodic emission of droplet in superconfinement. (b) Formation of liquid jet above the onset of entrainment (top) and collapse of neck to realise a drop (bottom). (c) Radius r_{xy} and (d) volume v of the drop as a function of channel thickness H. (e) Drop snap-off time t_s versus channel thickness H. Solid line represents theoretical fitting for thermal fluctuation-dominated neck break-up, which decays with exponent $\alpha = 0.42$.

As shown in the figure, v_{jet} is generally larger than the volume of the drops, which we estimate assuming an ellipsoidal shape as:

$$v_{drop} \simeq \frac{4}{3}\pi(2r_{xy})^2(2r_{xz}), \tag{6.11}$$

where r_{xy} and r_{xz} are the drop radii of curvature in the parallel and perpendicular planes to the wall. The mismatch between v_{jet} and v_{drop} is caused by the typically long necks that develop, which are absorbed by the main front once the drop is released.

The growth of the drop size with H observed in figure 6.5 (c) arises because both h_f ($\simeq \frac{1}{2}H$) and t_s increase with the channel thickness. Since the thickness of the neck connecting the jet to the drop, h_n, is comparable to the interface thickness ξ, we expect that its collapse is dominated by thermal fluctuations. This contrasts with drop emission at large scales, where drop emission is dominated by hydrodynamics [186]. The fluctuation-dominated neck breakup is characterised by (i) double-cone jet profiles [143, 195]; here, we find the opening angle $\sim 28°$ at the neck side and $\sim 37°$ at the drop side (see figure 6.6 (a)), in reasonable agreement with previous experiments [196], where the angles were around 30° on both sides of the breakup point. (ii) The pinching rate is described by a faster (algebraic) decay than that of macroscopic jets,

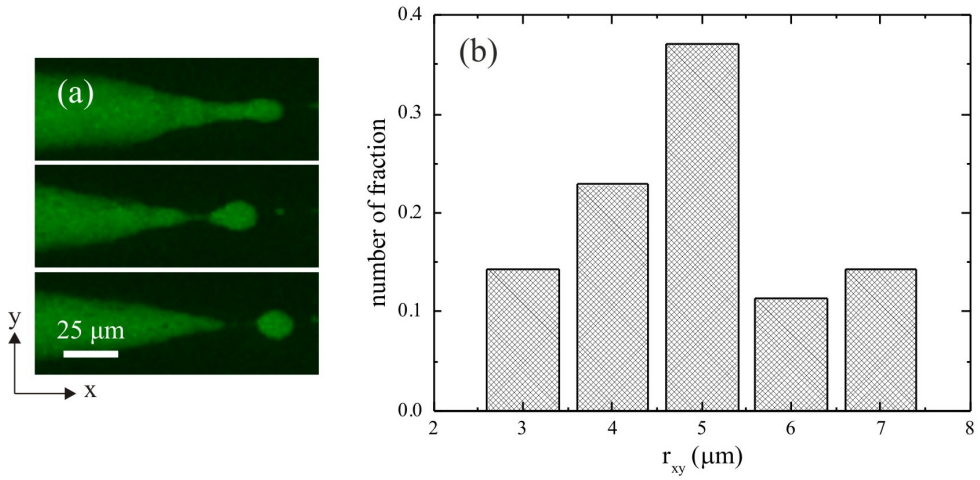


Figure 6.6: (a) Symmetric break-up profile. (b) Drop size distribution for $H = 10$ μm showing no satellite drops are emitted. The number of fraction is with respect to the total number of drops (~ 30).

which is linear [196]. Following reference [144], the collapse of the neck obeys:

$$h_n(t) \sim (t_s - t)^{\alpha}, \tag{6.12}$$

where $\alpha \simeq$ is 0.42. Since $h_n \sim H$, we expect that the snap-off time obeys $t_s \sim H^{1/\alpha}$. This prediction is tested against the experimental data in figure 6.5 (e), showing a good agreement. (iii) As the pinch-off occurs in the middle of the double-cone neck, the noise therefore imposes less polydispersity of the size of the drops. In figure 6.6 (b) we plot a histogram of the drop size distribution, which clearly shows that for a relatively small channel thickness, a regular drop size is produced, except for the case of large fluctuations in the neck region, where the formation of satellite drops is observed (see also the error bars in figure 6.5 (c)). Still, this is expected to be smaller than for the deterministic case, which is characterised by the formation of strings of satellite drops.

Remarkably, for the thicker channel used in our experiments ($H = 17$ μm), the jet is stabilised after one snap-off event and no further drops are emitted (figure 6.7). This suggests a cross-over to macroscopic hydrodynamics where viscous stresses coming from the flow within the jet hamper its collapse.

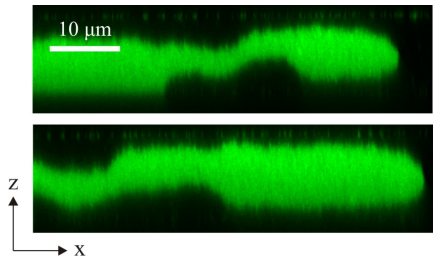


Figure 6.7: Stabilisation of emitted drop in $H = 17$ μm.

6.3.3 Related behaviour due to the thermal fluctuations

In addition to the above-mentioned phenomena, here we further show related behaviour in microchannels. Currently, we do not have an explanation for these observations, but clearly there is a rich interplay between wetting, thermal fluctuations and gravity.

(i) The combination of high capillary numbers and strong confinement in our set-up can be further exploited to induce the formation of complex structures; by quickly forcing the interface into our microchannels, it is possible to trigger the formation of pairs of fingers, which subsequently emit drops concurrently (figure 6.8).

(ii) The large thermal fluctuations displayed by our colloidal system may lead to a connection being formed between the colloidal liquid jet and the solid substrate upon drop emission, as shown in figure 6.9. The contact captures colloidal gas.

(iii) Figure 6.10 shows "bouncing" behaviour of a droplet in a channel. Again, gravity brings the interface of the drop in contact with the wetting layer, and allows the drop to coalesce with the wetting layer assisted by thermal fluctuations. However, as the drop moves forward with increasing velocity, it is being pushed back to the centre of the channel. This caused some volume of the drop left to be adhered on the wall.

These experiments indicate the feasibility of manipulating fluids through the combination of low surface tension and superconfinement, and open the possibility of controlling the stability and synchronisation of the emerging structures.

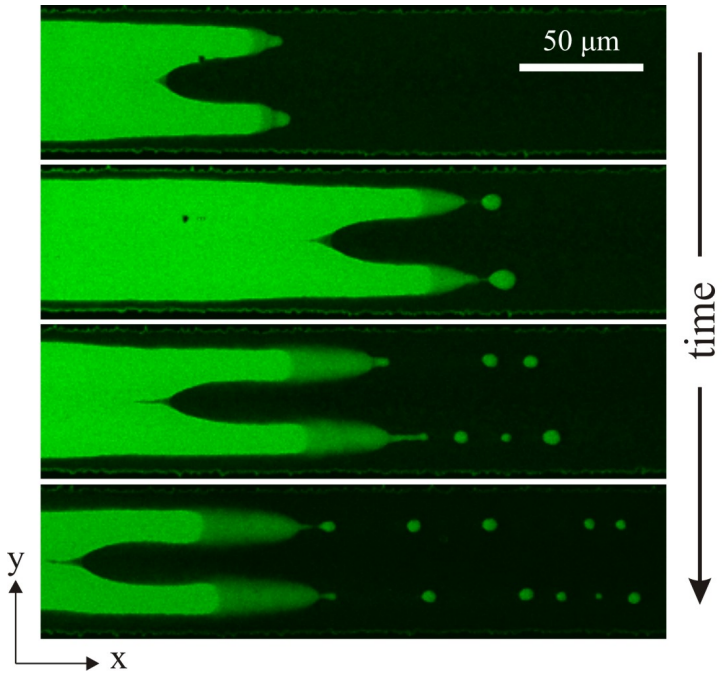


Figure 6.8: Tip splitting and double drop emission. At high capillary numbers the front splits into two fingers that subsequently destabilise and emit drops periodically.

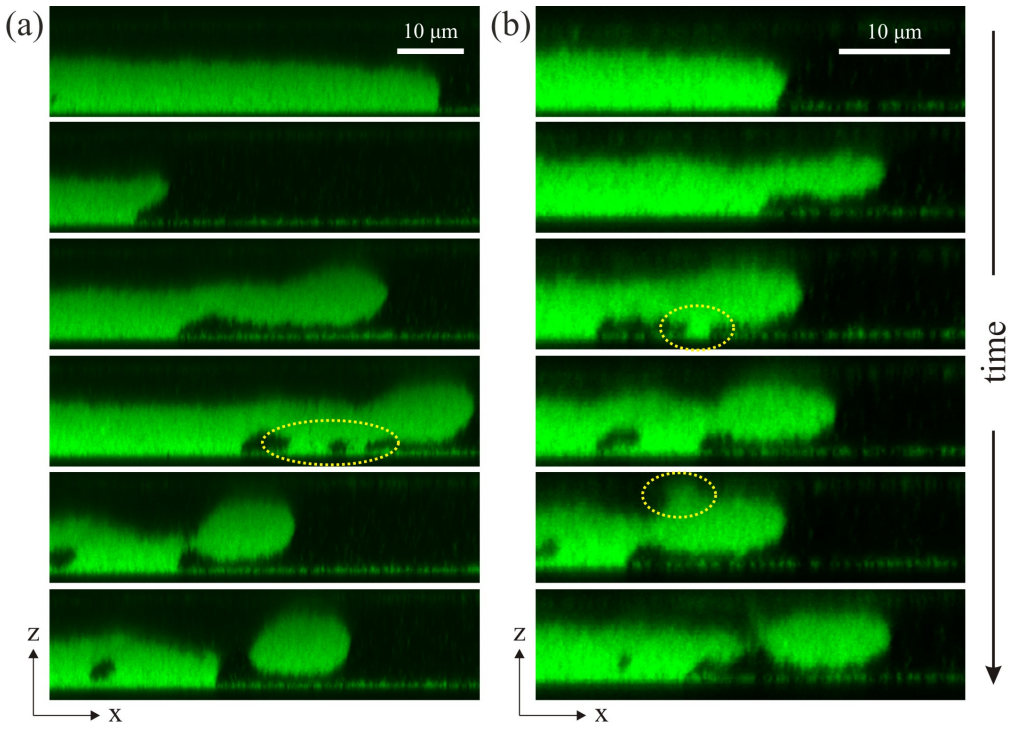


Figure 6.9: Contact of colloidal liquid jet with solid substrates due to the large thermal fluctuations in channel of thickness (a) $H = 14$ μm and (b) $H = 8$ μm.

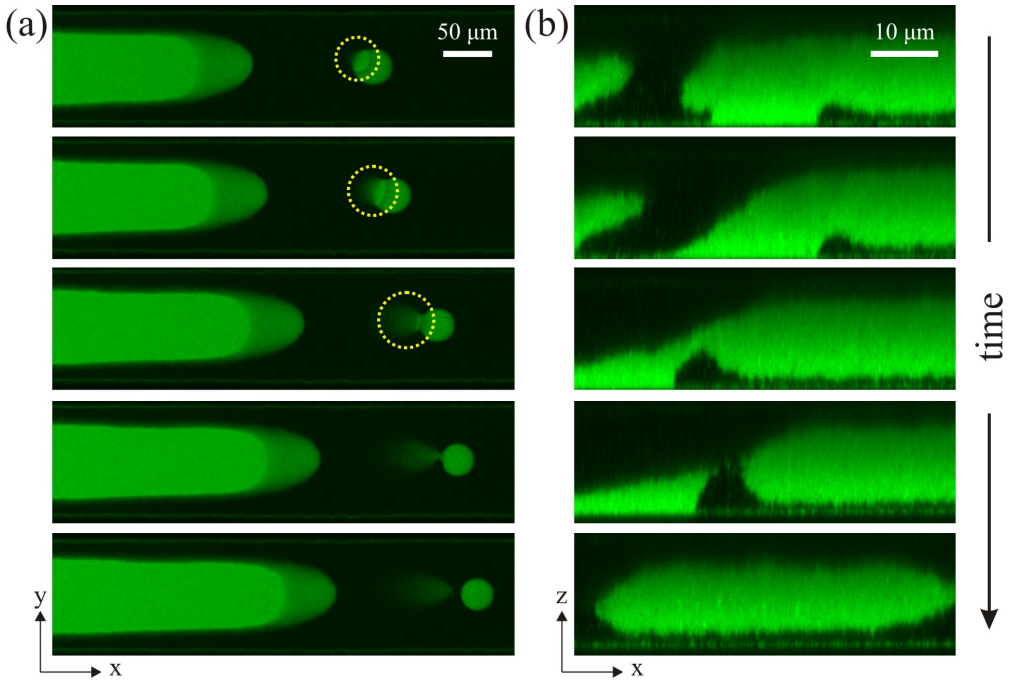


Figure 6.10: "Bouncing" movement of drop in channel viewed from (a) top of the channel (xy-plane) and (b) cross-section of the channel thickness (xz-plane).

6.4 Conclusion

In conclusion, we have presented the first experimental results of the rich fluid front behaviour which comes after the well-known Saffman-Taylor instability in superconfinement, where the intrinsic interfacial lengthscale overlaps with the lengthscale of confinement. The motion of the fluid front can lead to distinct fluid entrainment and drop spitting through the interplay between wetting, interfacial area and curvature, thermal fluctuations and gravity. By comparing to our theory, the contact line slip length, which is crucial to determine the stability of the moving front, can be directly defined. This destabilisation mechanism can be used to offer a more versatile and flexible technique to generate droplets in microfluidics devices, and opens the need to explore other important phenomena in superconfinement, e.g. hydrodynamic instabilities [127], superhydrophobicity [197], elastocapillarity [198], and active [199] and soft matter dynamics [200], to harness fluid manipulation at extremely small scales.

Acknowledgments

This work was a collaboration with Rodrigo Ledesma-Aguilar. We thank Ignacio Pagonabarraga, Aurora Hernandez-Machado and Roel Dullens for useful discussion.

Chapter 7

Wetting phenomena at geometrically sculpted wedges

ABSTRACT

We study wetting phenomena in a confined channel with geometrically sculpted walls, which we directly visualise by using laser scanning confocal microscopy. We use a mixture of colloid and non-adsorbing polymer as model fluid, with a short-ranged depletion interaction, rather than using simple molecular fluids where the typical van der Waals interactions are long-ranged. Our system displays complete wetting behaviour, a regime which has been widely investigated in theory. We discuss the shape, the thickness and the radius of the adsorbed colloidal liquid film formed inside the wedges. The growth of the wetting layer thickness shows a strong dependence on the geometry of the walls. Furthermore, moving from a flat surface to a capillary slit wedge, we observe a transition from wetting to capillary condensation phenomena. These observations are interpreted in light of modern theories.

7.1 Introduction

Pushed by the demand in the development of "lab-on-chips" devices, new advances in the soft-lithography technique have made it possible to fabricate substrates at size ranges from 1 to 100 μm with highly controllable geometrical shapes [64]. Fluids confined by such structured solid surfaces display rich phenomena, with relevance for applications in fields as diverse as microfluidics [201–203], biophysics [204], and super-repellent technologies [205, 206]. Recent studies focusing on the interplay between geometry and wetting have shown a variety of so-called *wetting transitions* that are extremely sensitive to the shape of the confining walls [54,207–214]. In particular, consider wedges of which the cross-section profile can be described by a shape function $h_w \propto |x|^s$ exposed to a gas that is close to coexistence with its liquid phase. Here, h_w is a lengthscale related to the height of the wedge and the exponent s sets the curvature from a flat ($s = 0$) to a parallel slit ($s = \infty$) (see figure 7.1). General stability arguments, supported by numerical and effective interfacial calculations, predict that the adsorbed liquid film grows with a power law of which the exponent depends on the shape of the wedge [54, 55]. This is sharply in contrast to that of flat surfaces, where the growth parameter depends only on the adsorbate-substrate interactions.

Efforts in this area have mainly been made within a theoretical framework. Experimental investigations proved to be challenging, despite interesting work using simple fluids [215–219]. Accessing this regime within the context of complex fluids such as colloidal mixtures has attracted considerable academic interest [220, 221]. This system brings several advantages: (i) in these complex systems, the strong depletion attraction between walls and colloidal particles consequently leads to a considerable amount of colloidal particles adsorbed inside the wedges. This allows to a direct visualisation of the adsorption phenomena using optical techniques such as confocal microscopy. (ii) Furthermore, the lengthscales in colloidal dispersions are of the micron rather than of the Angstrom scale as for typical molecular fluids. This range of lengthscales is directly compatible with microfluidics, so that the well-established soft-lithography protocols can be exploited to produce confining geometries to probe and observe the wetting behaviour over a whole range of structures [200]. (iii) In addition, the colloidal size leads to an ultralow interfacial tension, which consequently results in large thermal fluctuations. These give an extra opportunity to visualise the wetting transitions at the fluctuations level, providing a unique way to address these issues with short-ranged forces. Details of this colloid-polymer system are given

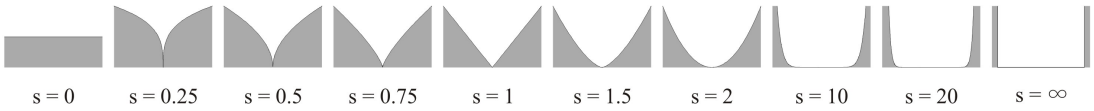


Figure 7.1: Possible shape of curvature of power law wedges described by cross-section function $h_w \propto |x|^s$. See also reference [54].

in chapter 2, and additional information may be found in [38].

In this work, we study the influence of geometry on wetting behaviour using colloid-polymer mixtures, which we visualise by means of laser scanning confocal microscopy (LSCM). In moving from flat to parallel slit walls, there is a whole zoo of theoretical predictions to be explored from wetting to capillary condensation. We will focus on complete wetting phenomena. Close to coexistence, one expects that the critical exponent describing the divergence of the wetting liquid film is strongly dependent on the shape of the walls. We access this regime by varying the dimensions of the channel, while keeping the bulk colloidal gas phase in contact with the walls.

This chapter is organised as follows: we begin by briefly describing the experimental set-up (section 7.2.1) and analysis procedure of the images (section 7.2.2). We then present and discuss the results. In section 7.3.1, we discuss the complete wetting behaviour on a flat substrate. In section 7.3.2, we analyse our wedge profiles by fitting with a shape function $h_w \propto |x|^s$. This is followed by section 7.3.3, where we discuss the wetting behaviour of fluid-fluid phase separated colloid-polymer mixtures in wedges of different shapes. Here, we focus on the shape, the thickness and the radius of the adsorbed wetting film. In section 7.3.4, we show a transition from wetting to capillary condensation phenomena when the wedge has a capillary slit shape. We finish with a conclusion and outlook (section 7.4).

7.2 Experimental details

7.2.1 Set-up

We used a mixture of fluorescently labelled poly(methylmethacrylate) (PMMA) colloids and xanthan polymer dispersed in water. A sample at a statepoint $\phi_c = 0.07$, $\phi_p = 7.50$ (point II in figure 2.2, chapter 2) was prepared, where the phase separation occurred via nucleation and growth. Analysis of the capillary waves spectrum of the free interface yields the interfacial tension $\gamma = 50$ nN/m and the capillary length $L_c = 52$ μm.

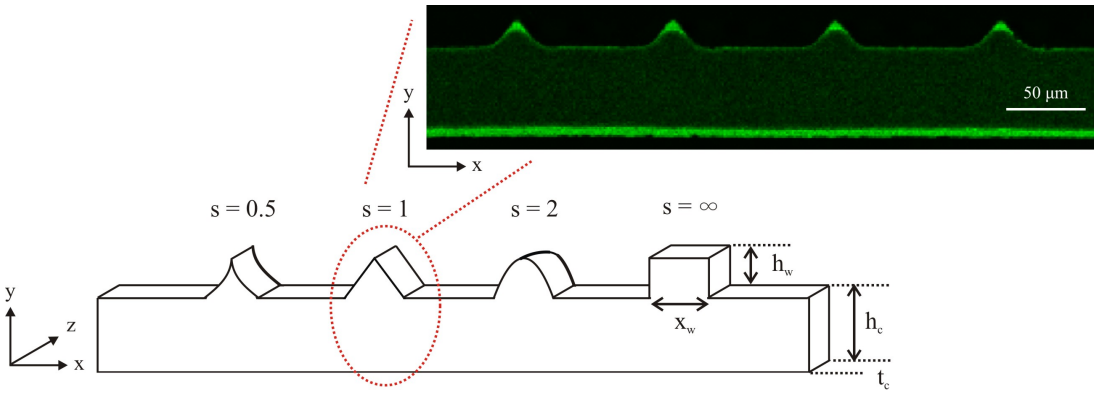


Figure 7.2: (Bottom) Schematic geometry of the microfluidic channel structured with different wedge shapes at the top wall. (Top) LSCM image of an example of the resulting fabricated wedge channel. Gravity points along the negative y-axis.

Microfluidic channels were constructed out of UV glue (NOA 81), as outlined in chapter 2. A straight channel was structured with power law wedges at the top wall. In this chapter, we limit the exponent s such that the curvature of the walls has a shape of a cusp ($s = 0.5$), linear ($s = 1$), parabolic ($s = 2$) and capillary slit ($s = \infty$), as schematically illustrated in figure 7.2 (bottom). Each wedge shape was repeated 10 times along the straight channel and two consecutive wedges were separated by a flat surface ~ 50 μm wide. The wedges were characterised by their height h_w and width x_w. The straight channel has height h_c, which was varied between 40 and 175 μm, while the thickness t_c was fixed at 10 μm, whereby giving "pseudo-2D" confinement. The walls are smooth on the colloidal lengthscale (~ 1 μm). An example of the fabricated microfluidic channel with a linear wedge is shown in figure 7.2 (top).

The structured microfluidic channel was plasma-cleaned for 3–4 minutes to change the hydrophilicity of the surface. The PMMA-xanthan sample was homogenised, and then the channel was filled by capillary action. A short plasma cleaning time resulted in a slow filling speed, which caused bubbles to be trapped on the bottom of the wedge structures. The channel was sealed using glue and left for an hour for the mixtures to completely phase separate. This is a sufficient time by which we observed no significant changes occurring in the channel and we started the measurement, but the actual time needed for the system to be at equilibrium is difficult to determine and might take longer than that (see also the discussion). The wetting behaviour of the separated colloidal phases was imaged by means of LSCM using 10x and 63x magnifications in the plane of gravity. It was not possible to observe the wetting behaviour for a very long time (> 4 hours), as the sample began to dry. The drying event occurred even

more rapidly when we changed the PMMA-xanthan in water to glycerol as the solvent, which also slowed down the equilibration of the system. In all cases, we observed that the flow of the sample in the channel did not stop completely. This might be due to a slight unevenness in the sample positioning, or a remaining small pressure difference between either end of the channel. This made imaging of the representative time series difficult, especially for the analysis of the thermal fluctuations of the adsorbed interface inside the wedges.

7.2.2 Image analysis

(i) Wetting film l_π and radius of curvature R_2 of the adsorbed wetting layer formed inside the wedges in the xy-plane:

LSCM images showing the adsorption of colloidal liquid film in wedges were analysed using Mathematica. The shape of the structured wedge walls was first determined by finding the edge using the built-in "EdgeDetect" function. This step worked well as shown in figure 7.3 (a) (red line), by which the points located at ± two pixels away from the mean surface were considered outliers and eliminated from the data list. The same method was used to define the shape of the adsorbed colloidal liquid meniscus formed inside and outside the wedge. The thickness of the wetting film l_π was estimated by defining a surface normal to the actual wall and varying its magnitude until the film was best described (see figure 7.3 (b)) – green line and the graph inset. This step gave information on the average thickness of the wetting film that covers all of the surfaces but the fluctuations of the interface were ignored. Finally, the radius of the adsorbed wetting meniscus inside the wedge was measured by fitting a circle of radius R_2 at the point of maximum curvature of the estimated wetting film, and the upper part of the circle was tangent with the edge of the meniscus. The fitting will of course be affected by the symmetry of the wedge and the actual detailed shape of the meniscus, but the effect seemed to be small and was reduced by tilting the images in a range less than ± 1° (see figure 7.3 (c)).

(ii) Thickness of the adsorbed wetting layer l_0 and height H above the bulk colloidal gas-liquid interface:

Figure 7.3 (d) summarised the located position of the colloidal gas-liquid interface in wedge channels, where the midpoint ($x = 0$) is plotted at the maximum point of the surface wedge

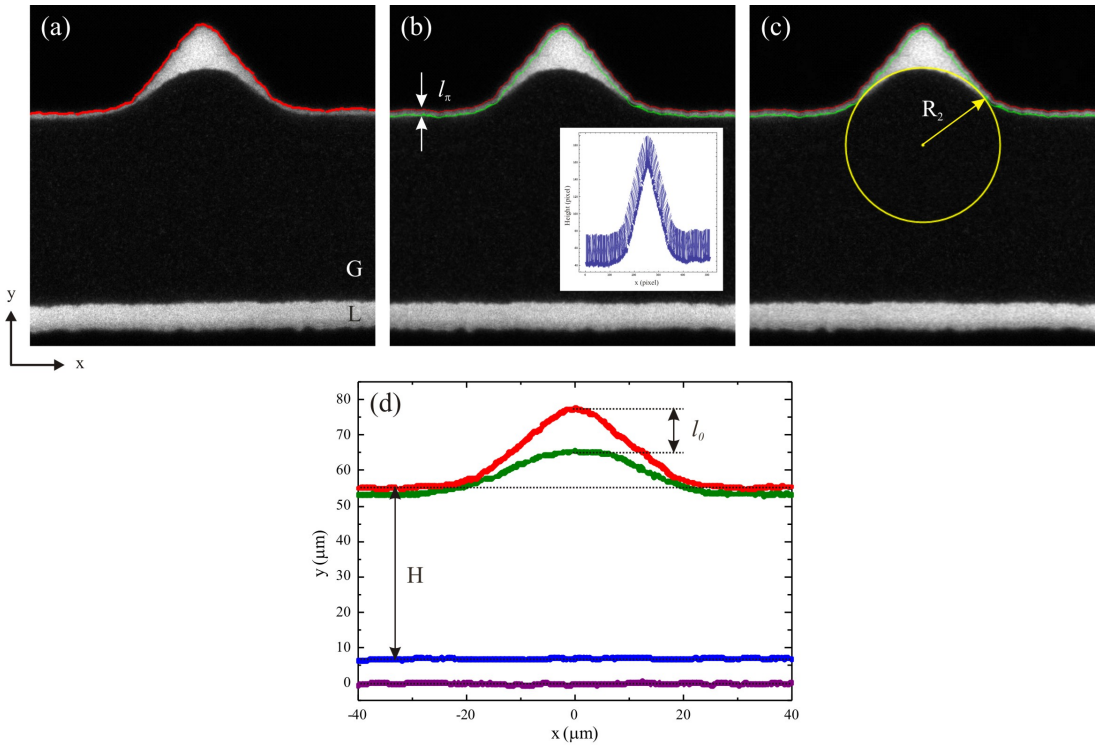


Figure 7.3: (a-c) The steps involved to determine the thickness of the wetting layer l_π and the radius of the adsorbed meniscus R_2 formed inside the wedge using Mathematica. (d) Graph of the located position of the colloidal gas-liquid interface in a wedge channel. The thickness of the adsorbed wetting film l_0 at the centre of the wedge and the height H above the bulk colloidal gas-liquid interface were determined as shown in the graph.

data. The thickness of the meniscus l_0 was calculated as the length from the structured wedge (red line) to the edge of the adsorbed meniscus (green line) at $x = 0$. Meanwhile, the height H was determined as the distance from the average position of the bulk colloidal gas-liquid interface (blue line), which was located using the same method as described above, to the flat surface at the top channel wall (red line).

7.3 Results and discussion

7.3.1 Complete wetting on a flat substrate

We begin by briefly discussing complete wetting on flat substrates, which depend on the physical interactions between the fluid particles and the substrate. In the case of van der Waals forces,

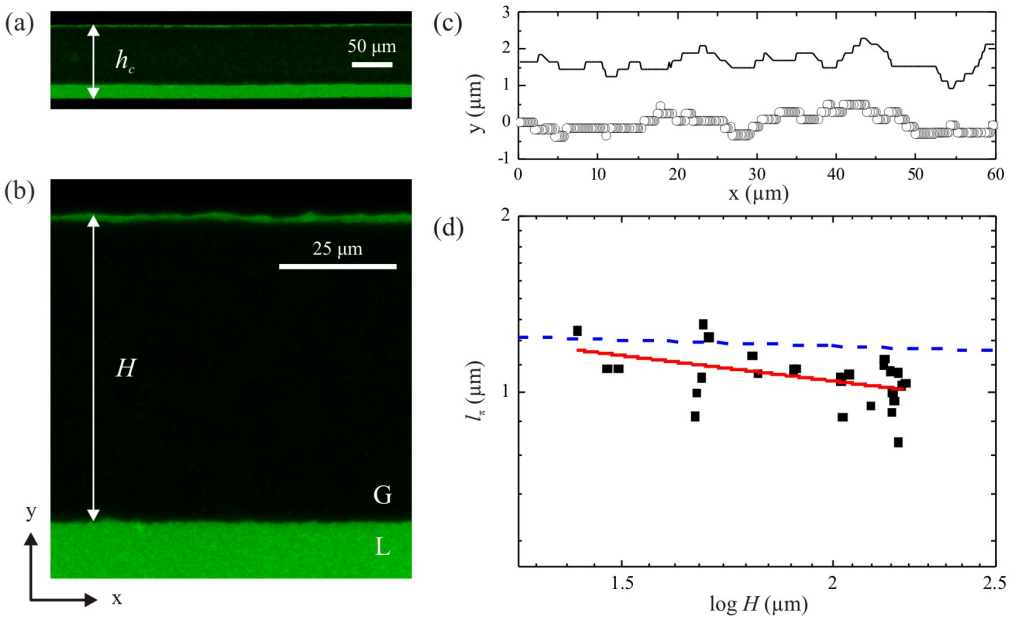


Figure 7.4: LSCM images of the separated colloidal-liquid and -gas phases in a flat channel taken with (a) 10x and (b) 63x objectives. (c) Plot of channel wall (full line) and colloidal liquid wetting film (open circles) along the x-direction. l_π is measured as an average height between the plots. (d) Plot of l_π as a function of log H. Filled squares represent experimental data. The full/red line is a linear fit with slope $\beta = -0.345$, while the dashed/blue line satisfies equation 7.2 [225].

the thickness of the adsorbed liquid film grows as a power law [222]:

$$l_\pi \sim |\delta\mu|^{-\beta^{co}} \tag{7.1}$$

where the exponent $\beta^{co} = 1/3$ [223, 224]. Here, $\delta\mu = \mu_0 - \mu$ represents the deviation of the bulk chemical potential from its saturation value μ_0. For short-ranged forces, however, the dependence with thermal roughness of the interface is more complicated, as will be discussed below.

For comparisons with further analysis, we measured l_π of phase separated colloid-polymer mixtures in flat microchannels are shown in figure 7.4 (a) – 10x and (b) – 63x magnifications. We made use of gravity by simply varying the gap between the upper and lower walls (h_c), so that at a distance H above the bulk colloidal gas-liquid interface, the chemical potential difference from coexistence becomes $\delta\mu = m^* gH$. For our colloids with a density $n_c = 1.17$ g/ml, the gravitational length $l_g = k_B T/m^* g$ is ~ 500 μm in water. Here, m^* is the buoyant mass, g the Earth's acceleration due to gravity, and $k_B T$ the thermal energy. We ignored the gravitational

effect on the polymer due to its negligible buoyant mass.

Our colloid-polymer system shows complete wetting behaviour, where a thin film of the colloidal liquid phase is seen to wet the walls. In figure 7.4 (d) we plot the mean thickness of the liquid wetting film l_π as a function of log H. The solid/red line represents a linear fit to these data with a slope equal to $\beta = -0.345$, in good agreement with that found for long-ranged forces. However, the substrate is relatively rough, comparable to the interface roughness (see figure 7.4 (c)). A more complex behaviour is found for rough surfaces, where the power law exponent β is smaller than 1/3 — its value depends on the fractal dimensions of the interface [226]. Moreover, for short-ranged forces the thermal fluctuations may play a dominant role (see, e.g. [62,225] and also the discussion below). Finally, we note here that the range over which $\delta\mu$ has been varied is limited and we are not able to discriminate the different behaviours here. This was also not in the scope of the performed research.

Furthermore, we observed surprisingly thick wetting layers of the colloidal liquid phase, typically ~ 1 μm. Similar behaviour has been observed previously by Aarts and Lekkerkerker [221], who pointed out possible non-equilibrium effects. Experiments by Hennequin *et al.* [62] showed that indeed a very thick film can be formed after several days of equilibration time. Remarkably, this is two orders of magnitude thicker than typical wetting films stabilised by van der Waals forces, which were absent for their colloid-polymer mixtures; the colloid-colloid forces are considered short-ranged with a range of the order of the colloid radius augmented with the effective polymer radius. It has been suggested that the confined interfacial fluctuations of the system can consequently create an entropic repulsion, which stabilised the wetting film [227,228]. The contribution of such interface fluctuations to the wetting stability has been explored by Hennequin *et al.* [62, 225] using confocal microscopy. In their calculations using a combination of capillary wave theory and renormalisation group theory for complete wetting, the following result was derived (indicated as a dotted/blue line in figure 7.4 (d)):

$$4\pi \exp\Big(-\frac{4\pi\gamma b l_\pi}{k_B T}\Big) = \frac{\Delta\rho g H k_B T}{\gamma b A}. \tag{7.2}$$

Here, $\Delta\rho$ is the density difference between gas and liquid phases, b is proportional to the bulk correlation length, i.e. $\sim R_c$ and A is proportional to $k_B T/R_c^2$ (see equation 42 in [225]), with R_c the radius of a colloid. This is of a similar magnitude and illustrates that we cannot discriminate between the two predictions.

7.3.2 Shape of the wedge walls (s)

The first column of figure 7.5 shows LSCM images of colloid-polymer mixtures in microfluidic channels with different wedge geometries. The shape of the walls has been analysed using Mathematica as explained in section 7.2.2. To easily compare the shape of each wedge, we plotted them at the same scale. Again, the average roughness of the wall is comparable with the colloidal lengthscales (~ 1 μm) and, for simplicity, has been ignored in this study. To further analyse the shape of the walls, the profiles are fitted to the expression $h_w \propto |x|^s$, as shown in figure 7.5 (second column). In case of a cusp (a and e), the wall profile is described by an exponent $s = 0.8$, a much larger value than expected — originally, a photomask with $s = 0.5$ was used. The change in the structure might come from several steps in patterning the channel, as, for example, (i) the air gaps between the mask and resist during the irradiation process result in non-uniform irradiation doses at the edges, consequently causing enlargement of the structure. (ii) The sharp, tiny structure at the centre of the cusp might cut off when peeling the PDMS elastomer away from the cured UV glue prepolymer. In case of linear (b and f) and parabolic (c and g) wedges, the wall profiles are very nicely described with exponent $s = 1$ and $s = 2$, respectively, while for the capillary slit (d and h), the wall is well fitted with exponent $s = 15$.

In sum, the soft-photolithography techniques used to pattern the channels with different wedge shapes in this study open the possibility to fully explore the complex behaviour of wetting in non-planar substrates. To our knowledge, although the behaviour has been broadly discussed in theory, experimentally only the behaviour of a liquid layer at walls with $0 < s \ll 1$ and one particular case of $s = 3$ have been studied [216, 219].

7.3.3 Wetting phenomena at geometrically structured substrates

In this section, we will present and discuss the rich wetting phenomenology that emerges when the shape of the substrate is varied from flat to various wedge curvatures. We consider the shape (l_k), the thickness (l_0) and the radius (R_2) of the adsorbed wetting film formed at the centre of the wedges.

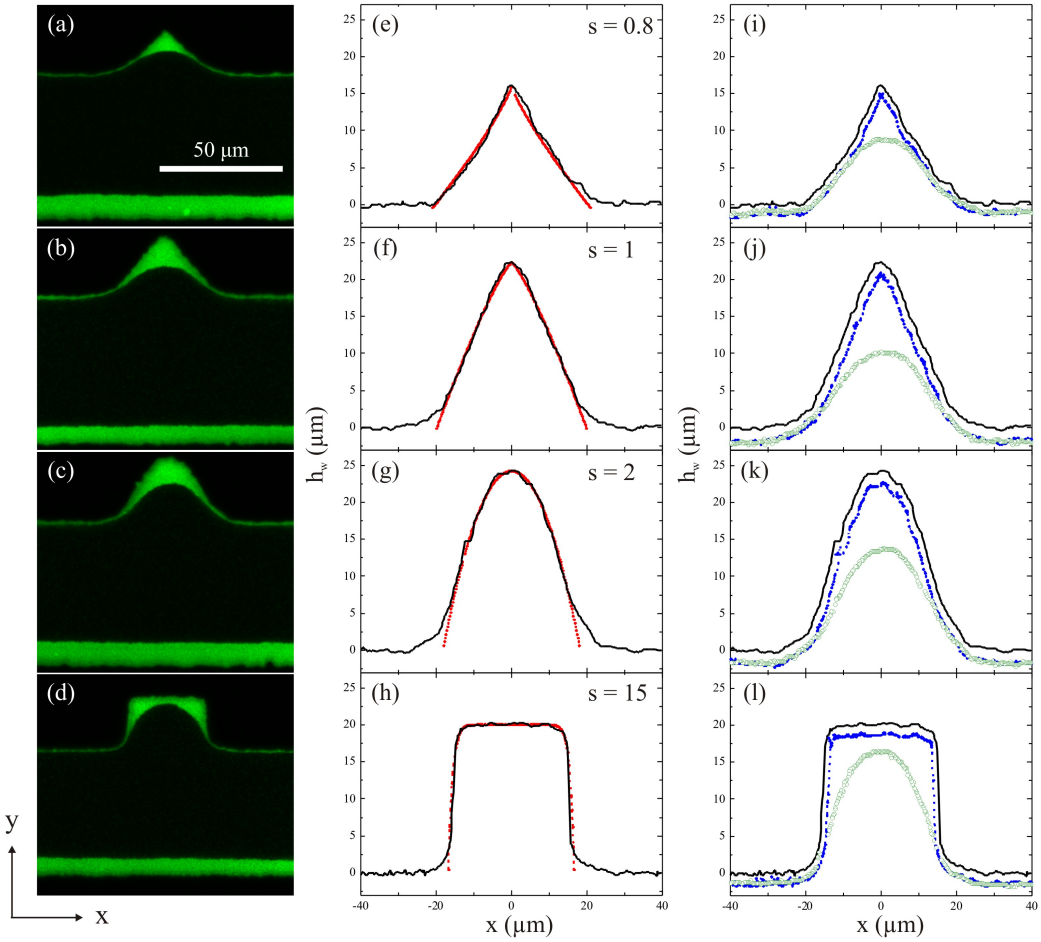


Figure 7.5: LSCM images showing the behaviour of phase separated colloid-polymer mixtures in (a) cusp, (b) linear, (c) parabolic and (d) capillary slit wedges. (e-h) Fitting the shape of the walls (black/full line) with wedge function $h_w \propto |x|^s$ (red/dotted line). (i-l) Plot of the wedge walls (black/full line), estimated wetting film (blue/dotted line) and adsorbed wetting interface (green/circles) in the direction x.

(i) Shape of the adsorbed meniscus (l_k)

Directly after filling the channel, a thick layer of colloidal liquid was observed at the midpoint ($x = 0$) of the wedges. This behaviour is in clear contrast with that previously observed on a flat substrate. The adsorption of a liquid phase in wedges in the case of complete wetting at coexistence can be understood from a simple stability argument [54]: below the saturation, a meniscus forms inside the wedge. The shape of the meniscus is given by the combination of maximum curvature with the radius set by the Laplace equation $R = \gamma/(\rho_L - \rho_G)|\delta\mu|$ and the thickness of the wetting layer l_π that cover the substrate here in case of an infinitely long wedge.

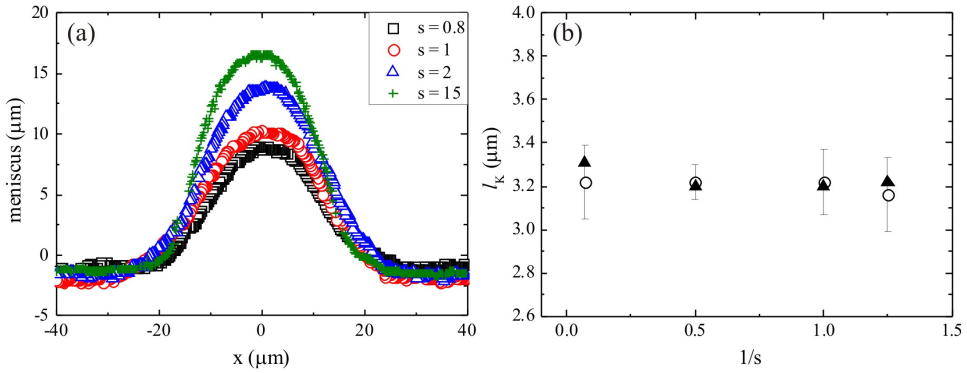


Figure 7.6: (a) The shape of the meniscus of the adsorbed wetting film in different wedges. (b) Plot of measured (open circles) and calculated (filled triangles) Kelvin length of the adsorbed meniscus in wedges.

In the third column of figure 7.5, we analysed the radius of curvature of the meniscus formed in each wedge, as described in section 7.2.2. The formation of such curved menisci is related to the Kelvin length as given by the Young-Laplace equation:

$$\frac{1}{l_K} = \frac{1}{R_1} + \frac{1}{R_2} \tag{7.3}$$

where R_x is the radius of curvature in the plane ($x = 2$) or in the perpendicular direction ($x = 1$). At $H \sim 45$ μm above the colloidal gas-liquid interface, the radius of the curvature R_2 is ~ 18 μm, and since $R_1 = (t_c - 2l_\pi)/2$ is assumed to be constant, the observed Kelvin length is found to be of the order of ~ 3 μm for all shapes. Of course a thick film may modify the Kelvin length, as first recognised by Derjaguin [229], but here, for simplicity, we fixed the thickness of the wetting layer at $l_\pi = 1.4$ μm.

In figure 7.6 (b), we compare our experimental Kelvin length for each wedge to those following Evans [230, 231]. Adapting those to the colloid-polymer mixtures in a capillary slit (see [221]), we find:

$$l_K = \frac{\gamma_{GL}}{(n_c^L - n_c^G(n_p^L/n_p^G))\delta\mu_c} \tag{7.4}$$

with n_x^L and n_x^G the colloid ($x = c$) or polymer ($x = p$) number density in the liquid (L) and gas (G) phases, respectively. For colloid-polymer mixtures far away from the critical point with an interfacial tension of 50 nN/m, for a small shift in the chemical potential $\delta\mu \sim 0.09$ k_BT ($H = 45$ μm), and assuming that $\Delta n = n_c^L - n_c^G(n_p^L/n_p^G) = 0.3/v_c$, with v_c the volume of a

colloid, the Kelvin length becomes of the order of a few micrometres, which is comparable with those found in the experiments. If we ignore the effect of wetting layer thickness in the Kelvin equation above, we can qualitatively draw the conclusion that the system is close to equilibrium, although it is actually difficult to determine how close.

(ii) Adsorption thickness (l_0)

Now, we will see how the shape of the wall can alter the thickness of the meniscus measured in the midpoint of the wedge when approaching the bulk liquid-gas coexistence. Rascón and Parry [54,55] have established novel critical exponents which depend on geometry for the full range of shapes. Interestingly, the exponents are universal with respect to the exponents associated with the range of the intermolecular forces. For comparisons with later observations, we summarise their results in figure 7.7.

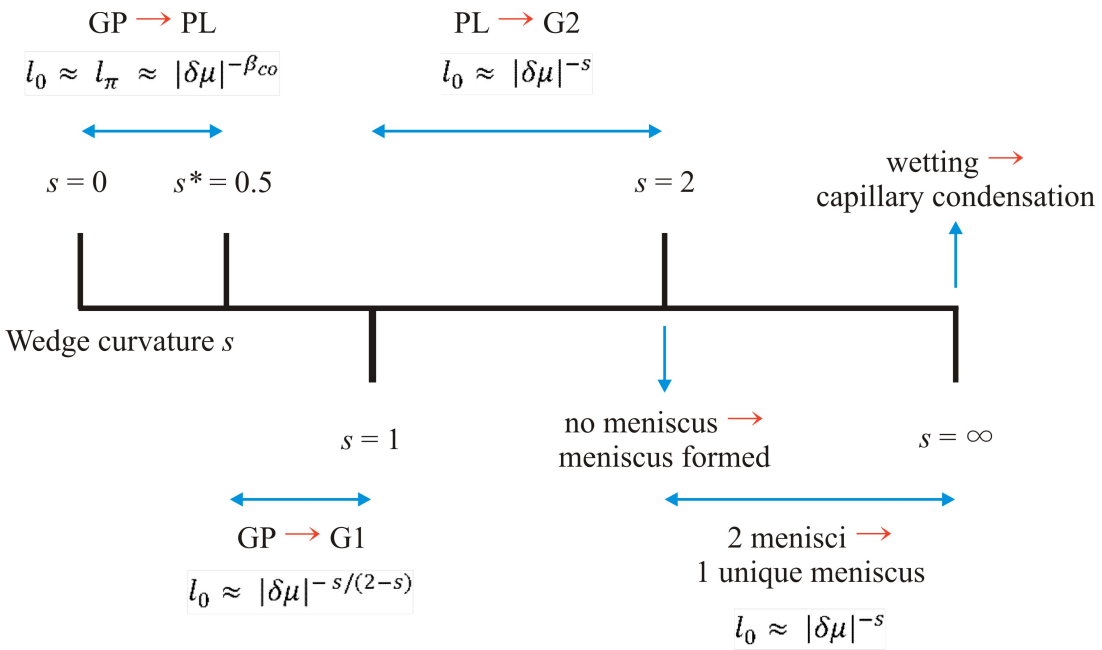


Figure 7.7: Wetting behaviour of a fluid in the full wedge shapes obtained by Rascón and Parry [54]. Red arrows represent transitions of the wetting regime when approaching the coexistence; PL = planar, GP = geometry and planar, G1 = first geometry-dominated and G2 = second geometry-dominated regimes. The thickness of the adsorbed meniscus l_0 grows by different exponents as stated, which depend on the curvature of the wedges s. For the marginal case of $s^* = 0.5$ (for van der Waals forces), the adsorbed liquid film grows by an exponent $\beta = 1/3$.

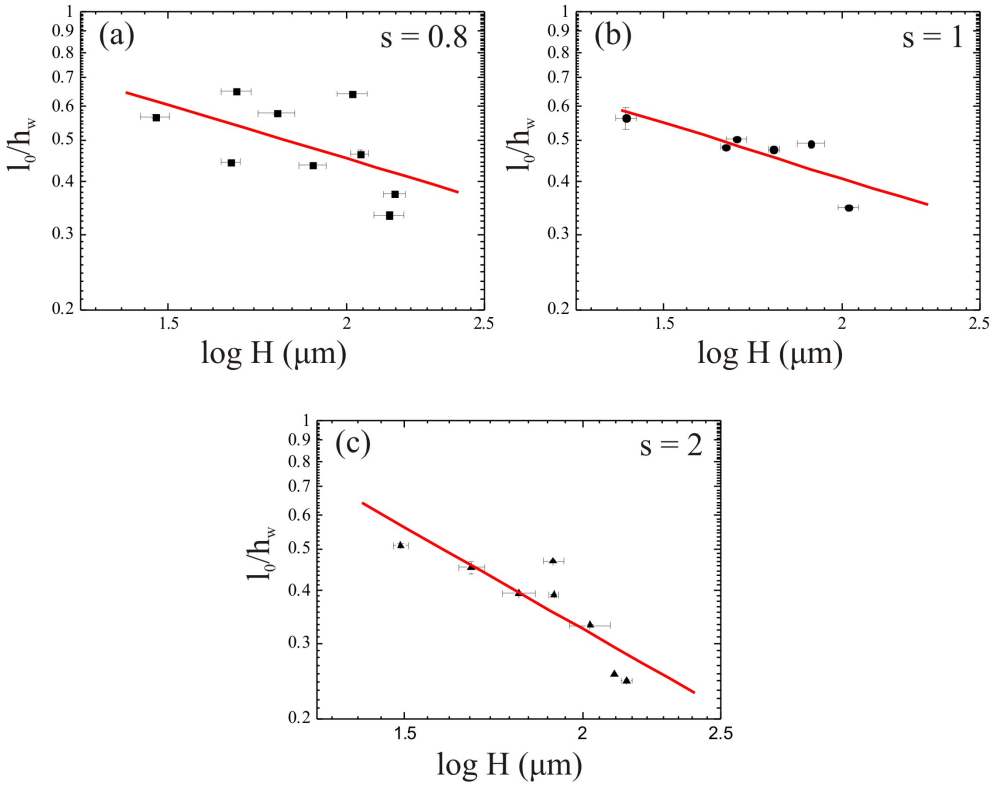


Figure 7.8: Ratio of the adsorbed wetting layer thickness l_0/h_w measured at wedge midpoint $x = 0$ as a function of log H for (a) $s = 0.8$, (b) $s = 1$ and (c) $s = 2$. Symbols represent experimental data and full lines are linear fits to those data.

For a more quantitative analysis, we plot the ratio of wetting film thickness measured at $x = 0$ divided by the height of the wedge l_0/h_w, as a function of log H, as shown in figure 7.8. Error bars are found within one channel by measuring for different wedges with the same s. The solid lines represent the result of the power law fit to these data. Again, we stress that we have only been able to take data over a limited range and the given exponent should be carefully interpreted.

The wetting thickness measured for wedge profile $s = 0.8$ shows a growth exponent with $\beta \sim$ -1 when approaching bulk liquid-gas coexistence. We then extend our analysis for $s = 1$. The midpoint thickness again grows by an exponent $\beta \sim$ -1. The exponent is comparable with the value of -1 found numerically by Rascón and Parry in their mean field analysis of wedges with profiles $0.5 < s < 1$ [54, 55] and later shown by experiments [215–217]. For both shapes, a cross-over behaviour from planar-like to geometry-dependent is expected, but not observed here. This might be due to the wedge dimensions, which are expected to alter the position of the cross-over. However, in other experiments, we found that the wetting growth exponent is

not affected by the dimensions of the wedge.

For the case of $s = 2$, which corresponds to a parabolic wedge, the wetting behaviour becomes even more complicated, as shown in figure 7.9. Far from saturation, no meniscus was formed and a thin layer wets the substrates (image 1). At critical log $H \sim 2$ the meniscus starts to develop (image 2) and continuously grows by an exponent $\beta \sim 1.9$ (images 3 and 4), which is again comparable with theory which predicts 2 [54]. This rich wetting behaviour is a direct result of the geometry. In theory, the critical limit of chemical potential difference from which the meniscus starts to be formed is given by $R + l_\pi = x_w/2$. In our experiments, we find $R_2 + l_\pi \sim 16$ μm, which is comparable with $x_w/2 \sim 20$ μm.

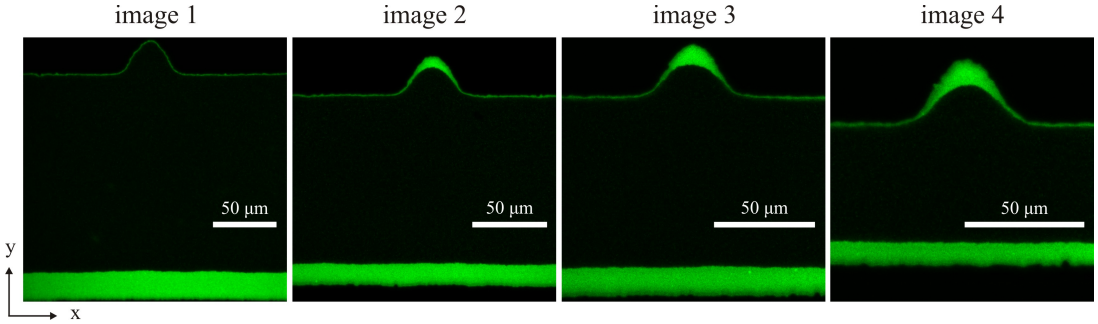


Figure 7.9: Wetting behaviour of phase separated colloid-polymer mixtures in channel with wedge $s = 2$ and varying height h_c. Away from the bulk colloidal liquid-gas coexistence, no meniscus is observed (image 1). At the critical threshold, the meniscus starts to develop (image 2) and continuously grows by an exponent $\beta \sim 1.9$ (images 3 and 4).

(iii) Radius of curvature of the adsorbed meniscus (R_2)

Approaching coexistence ($\delta\mu \to 0$), the radius of curvature also increases, creating a much flatter interface. Figure 7.10 demonstrates this dependence where we plot R_2 as a function of log H. The solid line represents power law fits to the data, but given the limited range they are simply used to guide the eye. In particular, in the case of $s = 0.8$ and $s = 1$, the data display two distinct regimes, above and below $\log H \sim 2\,\mu$m. Far away from coexistence, there is a steep increase in the growth of the meniscus radius. Moving closer to the coexistence, a smaller growth was found. In contrast, for the parabolic case ($s = 2$), a single growth exponent was observed. A cross-over from a planar to a geometrically dominated regime may be behind the changes in slopes, and we are currently in the process of discussing with Prof. A. O. Parry and Dr. C. Rascón.

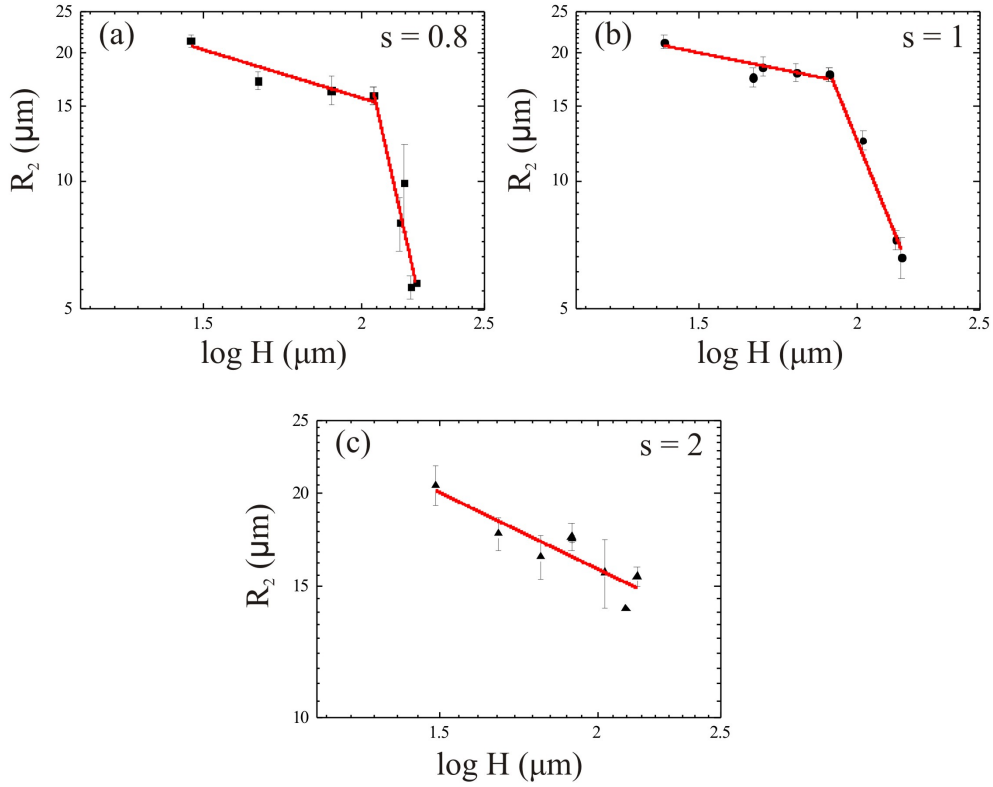


Figure 7.10: Radius of adsorbed curvature as a function of log H for (a) $s = 0.8$, (b) $s = 1$ and (c) $s = 2$. Symbols represent experimental data and full lines are linear fits to guide the eye.

7.3.4 Capillary condensation

By extending the wedge profile to the limiting case of $s \to \infty$ (a parallel slit geometry), a new phenomenon emerges, where the wetting transforms smoothly into capillary condensation. To further study the transformation, we specifically design the wedge by varying the gap between parallel walls x_w = 20, 30, 40 and 50 μm, while fixing the wedge height at $h_w = 20$ μm. The channel height h_c was fixed at 50 μm, so that at $H \sim 40$ μm above the bulk colloidal gas-liquid interface, the shift chemical potential from coexistence was $\delta\mu \sim 0.08\, k_B T$.

Figure 7.11 shows (a) LSCM images and (b) shapes of the wetting behaviour of the colloidal liquid phase in capillary slits of different widths x_w. At the largest x_w, the wetting is identical to that of a flat surface, where a thin layer of the colloidal liquid phase covers the surface (image 1). Decreasing the gap between planar walls leads to the formation of menisci individually centring at both corners, whose shapes are symmetrical with one another (image 2). Further decreasing the slit gap makes the menisci slowly grow and eventually at $x_w = 30$ μm, the menisci merge

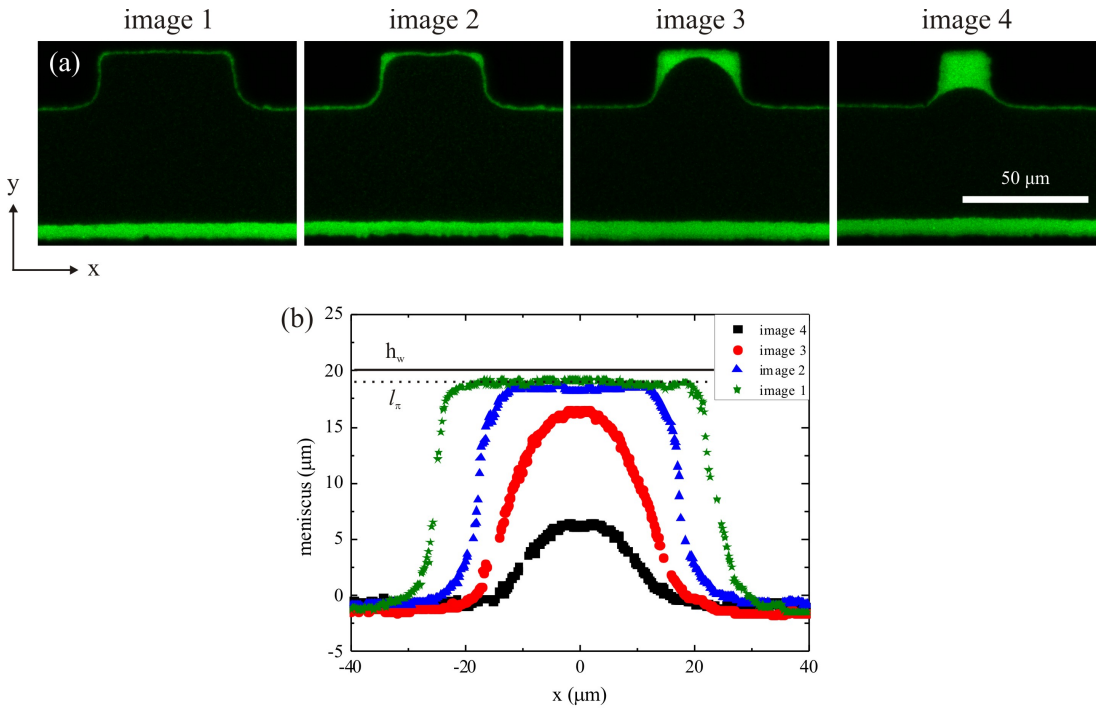


Figure 7.11: (a) LSCM images of separated colloidal-liquid and -gas phases in capillary slit of varying width x_w. (b) Plot of the shape of the adsorbed meniscus (symbols). Full line represents the average height of the wedge h_w and dotted line represents estimated wetting layer l_π.

into a single one centralised at the centre of the wedge (image 3). Here, we found that at the given chemical potential difference $\delta\mu$, the thickness of the wetting layer $l_0 \sim 1.84 \pm 0.25$ μm and the radius of the curvature $R_2 \sim 14.35 \pm 0.58$ μm. Since this is the first direct observation of the transition (from images 2 to 3), we state the values for comparison with later studies. The thickness of this single meniscus is expected to strongly depend on the changes in chemical potential difference. Finally, at the smallest slit gap, the colloidal liquid layer almost completely filled the space between the walls, giving a capillary condensation phenomenon (image 4). In this case, the thickness of the wetting layer drastically increased to $l_0 \sim 10.32 \pm 2.52$ μm, while the radius of curvature $R_2 \sim 10.20 \pm 1.82$ μm. This transformation (from images 3 to 4) is qualitatively in good agreement with theory [54].

Furthermore, a purely geometrical model predicts that the transformation seen between images 3 to 4 occurs at $R + l_\pi = l_K$, which recovers the Kelvin length, with a small correction from l_π to account for the influence of the short-ranged forces [54]. This is in line with work of Schmidt *et al.* [220] who used density functional theory and performed simulations to study the capillary condensation phenomenon of colloid-polymer mixtures in a capillary slit. Their

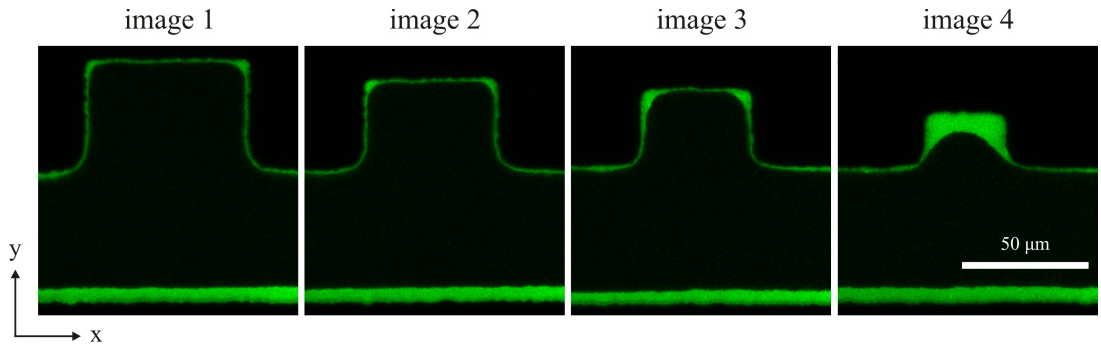


Figure 7.12: Behaviour of phase separated colloid-polymer mixtures in capillary slit of varying both the height h_w and width x_w imaged by LSCM.

results show a good agreement with the Kelvin equation, except for the system being very close to the critical point. In our experiments, the threshold was calculated to be $\sim 11.06 \pm 1.9$ μm, although further experimental verification is required.

In addition, in figure 7.12 we show a similar transformation of wetting to capillary condensation phenomena when varying both the height h_w and width x_w of the capillary slit, giving an alternative set-up to further study the behaviour. This also reflects the flexibility of using soft-lithography to fabricate and control the shape of the channels and the effectiveness of using colloid-polymer mixtures as a model system.

7.4 Conclusion and outlook

In conclusion, we have shown that a perfect compatibility match between microfluidics and colloidal particles allows to directly observe the behaviour of wetting in patterned substrates over the whole range of geometry shapes. The colloidal liquid film completely wets the walls forming a thick meniscus at the centre of the wedges and finally shows a transition to capillary condensation in the capillary slit geometry. We have focused on the shape, the thickness, the radius and transitions for $s = \infty$. The observations are in good agreement with those predicted by theory, but further experimental work will reveal the influence of possibly remaining non-equilibrium effects. We furthermore have performed analysis of the thermal fluctuations, which show promising effects, but they will require further work (figure 7.13). Finally, we note that the dynamics behind the wetting phenomena are still largely unexplored, both from an experimental and theoretical point of view.

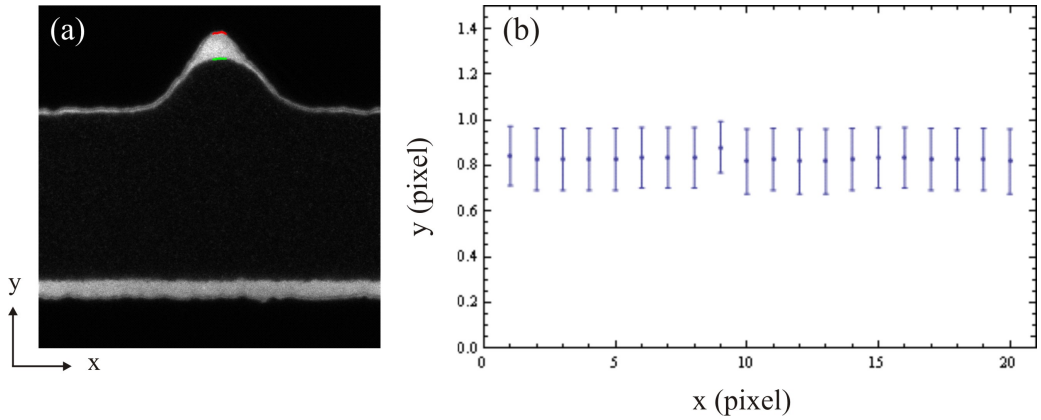


Figure 7.13: (a) LSCM image of colloidal fluids in a linear wedge. The positions of the adsorbed meniscus (green) and wedge walls (red) are located by fitting the intensity with tanh function using Mathematica. (b) Mean roughness of the located meniscus interface.

Acknowledgments

We thank Andy Parry and Carlos Rascón for useful discussion.

Summary

This thesis reported on a study of the interfacial instabilities and wetting behaviour of confined colloid-polymer mixtures. In chapter 1, we introduced the colloid-polymer system. A colloidal system with a colloidal diameter a thousand times larger than that of atoms/molecules brings the interfacial tension down to an ultralow limit. As a consequence, both the static and dynamic properties of our interfaces are being altered: some lengthscales increase, whereas others decrease. The characteristic units are such that they become highly compatible with optical microscopy and micro-fabrication techniques. This makes the colloid-polymer mixture an excellent model fluid to study interfacial instabilities and wetting problems.

In chapter 2, we introduced the colloid-polymer model system, i.e. poly(methylmethacrylate) (PMMA) colloids + xanthan polymers in water. The system phase separated into colloidal-liquid and -gas phases, where the interface between them was very rough and could be directly observed by laser scanning confocal microscopy (LSCM). We outlined the analysis of the thermal capillary waves of the free interface where we were able to obtain the physical properties of the system. These are the central, key parameters for the study of interfacial instabilities and wetting phenomena. Furthermore, the experimental techniques were described, which include the rheometer used, the soft-lithography protocols for fabrications of microfluidics devices and LSCM to visualise the behaviour of the colloidal interface in real-space and -time in three dimensions.

A review of the Saffman-Taylor instability was presented in chapter 3. Beginning with the original work by Saffman and Taylor in 1958, we then focussed on the extensions of their theory, dealing with the role of surface tension and the third dimension of the viscous fingers. We highlighted the advantages of using a colloid-polymer system, together with microfluidics and confocal microscopy techniques to address the subject.

In chapter 4 and chapter 5, we presented and discussed our experimental results. We focused on three aspects of the instability. (i) The interface between the two demixed phases has an ultralow surface tension, such that the role of thermal interface fluctuations can be addressed. (ii) We imaged the interface in three dimensions, allowing us to study the interplay between interface curvature and flow. (iii) The displacing fluid wetted all walls completely, in contrast to traditional viscous fingering experiments, in which the displaced fluid wets the walls. Starting with chapter 4, observations in the xz-plane were presented. Compared with lattice Boltzmann simulations, we revealed that the cross-over of the interfacial profile from a concave to a convex meniscus, and to xz-fingers, depended on the capillary and Peclet numbers, and on the viscosity contrast. Experiments further showed a meandering motion of the xz-finger, which might be due to the large thermal fluctuations effects of the interface. Chapter 5 continued with the observations of fingering in the xy-plane, the wide dimensions of the channel. The interfacial curvature in the xz-plane had a pronounced effect on the onset of the Saffman-Taylor instability. In particular, there was a threshold velocity for viscous fingering. Finally, we contrasted fingering in the xz-plane, caused by the inability of the contact line to move at sufficient velocity to keep up with the leading interface, and fingering in the xy-plane, due to the interface instability identified by Saffman and Taylor.

In chapter 6 we experimentally studied the contact line motion in super-confined rectangular cells, which is actually a continuation from the Saffman-Taylor experiments in a high velocity regime. Changing the thickness of the confinement relative to the capillary length of the system provided a mechanism to control the stability of the fluid front dynamics. A theoretical argument based on the coupling between contact line friction and capillary viscous bending was presented. A good agreement between experiments and theory was obtained for the onset of the instability, leading to a direct method to probe the slip length of the interface. Unstable fonts developed into liquid jets, which then led to the periodic emission of droplets with narrow size distributions. We found that the drop emission was dominated by thermal fluctuations.

In the final chapter, chapter 7, we turned our attention to the wetting behaviour in geometrically wedged substrates. We used the colloid-polymer mixtures as model fluid, in which the depletion interaction is short-ranged, rather than using molecular fluids where the van der Waals interactions are typically long-ranged. We discussed the shape, the thickness, and the radius of the adsorbed colloidal liquid film formed inside the wedges in light of the theoretical

prediction of Rascón and Parry [54, 55]. A satisfied agreement with theory was achieved over a wide range of wedge shapes. Furthermore, for the parallel capillary slit limit, we observed a transition from wetting to capillary condensation, again in agreement with theory. However, some non-equilibrium effects could not be completely ruled out.

Bibliography

[1] The Quran. Chapter 55, verses 19-20.

[2] J. D. van der Waals. *Z. f. Phys. Chem.*, 13:657, 1894.

[3] M. V. von Smoluchowski. *Ann. Phys.*, 25:205, 1908.

[4] L. Mandelstam. *Ann. Phys.*, 41:609, 1913.

[5] F. P. Buff, R. A. Lovett, and F. H. Stillinger. *Phys. Rev. Lett.*, 15:621, 1965.

[6] A. Vrij. *Adv. Colloid Interface Sci.*, 2:39, 1968.

[7] M. K. Sanyal, S. K. Sinha, K. G. Huang, and B. M. Ocko. *Phys. Rev. Lett.*, 66:628, 1991.

[8] C. Fradin, A. Braslau, D. Luzet, D. Smilgies, M. Alba, N. Boudet, K. Mecke, and J. Daillant. *Nature*, 403:871, 2000.

[9] J. H. Sikkenk, J. M. J. van Leeuwen, E. O. Vossnack, and A. F. Bakker. *Physica A*, 146A:622633, 1987.

[10] D. G. A. L. Aarts, M. Schmidt, and H. N. W. Lekkerkerker. *Science*, 304:847, 2004.

[11] D. Derks, D. G. A. L. Aarts, D. Bonn, H. N. W. Lekkerkerker, and A. Imhof. *Phys. Rev. Lett.*, 97:038301, 2006.

[12] C. P. Royall, D. G. A. L. Aarts, and H. Tanaka. *Nature Phys.*, 3:636, 2007.

[13] D. G. A. L. Aarts and H. N. W. Lekkerkerker. *J. Fluid Mech.*, 606:275, 2008.

[14] J. S. Rowlinson and B. Widom. *Molecular Theory of Capillarity*, Clarendon Press, Oxford, 1982.

[15] P. G. de Gennes. *Scaling Concepts in Polymer Physics*, Cornell University Press, Ithaca, 1979.

[16] T. Graham. *Phil. Trans. Roy. Soc.*, 151:183, 1861.

[17] M. D. Haw. *J. Phys.: Condens. Matter*, 14:7769, 2002.

[18] C. Bigg. *Stud. Hist. Phil. Sci.*, 39:312, 2008.

[19] A. Einstein. *Ann. Phys.*, 17:549, 1905.

[20] J. Perrin. *Ann. de Chim. Phys.*, 18:5, 1908.

[21] J. Perrin. *Les Atomes*, Libr. Felix Alcan, Paris, 1920.

[22] R. J. Hunter. *Foundations of Colloid Science*, Oxford University Press, 2nd edition, 2001.

[23] S. Hachisu. *Croatica chemica acta*, 71:975, 1998.

[24] A. Vrij. *Pure and Applied Chemistry*, 48:471, 1976.

[25] P. Atkins and J. de Paula. *Physical Chemistry*, Oxford University Press, 7th edition, 2002.

[26] B. V. Derjaguin and L. Landau. *Acta Physicochim (URSS)*, 14:633, 1941.

[27] E. J. Verwey and J. Th. G. Overbeek. *Theory of the Stability of Lyophobic Colloids*, Elsevier, Amsterdam, 1948.

[28] S. Asakura and F. Oosawa. *J. Chem. Phys.*, 22:1255, 1954.

[29] S. Asakura and F. Oosawa. *J. Pol. Sci.*, 33:183, 1958.

[30] H. N. W. Lekkerkerker, W. C. K. Poon, P. N. Pusey, A. Stroobants, and P. B. Warren. *Europhys. Lett.*, 20:559, 1992.

[31] T. Eckert and E. Bartsch. *Phys. Rev. Lett.*, 89:125701, 2002.

[32] P. Lu, E. Zaccarelli, F. Ciulla, A. B. Schofield, F. Sciortino, and D. A. Weitz. *Nature*, 453:499, 2008.

[33] W. C. K. Poon. *J. Phys.: Condens. Matter*, 14:R859, 2002.

[34] A. P. Gast, C. K. Hall, and W. B. Russel. *J. Coll. Int. Sci.*, 96(1):251, 1983.

[35] B. Vincent. *Colloids Surf.*, 24:269, 1987.

[36] B. Vincent, J. Edwards, S. Emmett, and R. Croot. *Colloids and Surfaces*, 31:267, 1988.

[37] H. N. W. Lekkerkerker. *Colloids Surf.*, 51:419, 1990.

[38] H. N. W. Lekkerkerker and R. Tuinier. *Colloids and the Depletion Interaction*, Lecture Notes in Physics. Springer, Dordrecht, 2011.

[39] G. A. Vliegenthart and H. N. W. Lekkerkerker. *Prog. Colloid Polym. Sci.*, 105:27, 1997.

[40] E. H. A. de Hoog and H. N. W. Lekkerkerker. *J. Phys. Chem. B*, 103(25):5274, 1999.

[41] B. H. Chen, B. Payandeh, and M. Robert. *Phys. Rev. E*, 62:2369, 2000.

[42] E. H. A. de Hoog and H. N. W. Lekkerkerker. *J. Phys. Chem. B*, 105(47):11636, 2001.

[43] D. G. A. L. Aarts, J. H. van der Wiel, and H. N. W. Lekkerkerker. *J. Phys.: Condens. Matter*, 15:S245, 2003.

[44] E. A. G. Jamie, G. J. Davies, M. D. Howe, R. P. A. Dullens, and D. G. A. L. Aarts. *J. Phys.: Condens. Matter*, 20:494231, 2008.

[45] A. Vrij. *Physica A*, 235:120, 1997.

[46] J. M. Brader and R. Evans. *Europhys. Lett.*, 49(5):678, 2000.

[47] J. M. Brader, R. Evans, M. Schmidt, and H. Löwen. *J. Phys.: Condens. Matter*, 14(1):L1, 2002.

[48] A. Moncho-Jordá, B. Rotenberg, and A. A. Louis. *J. Chem. Phys.*, 119(23):12667, 2003.

[49] D. G. A. L. Aarts, R. P. A. Dullens, H. N. W. Lekkerkerker, D. Bonn, and R. van Roij. *J. Chem. Phys.*, 120(4):1973, 2004.

[50] G. K. Batchelor. *An introduction to Fluid Dynamics*, Cambridge University Press, Cambridge, 1967.

[51] P. G. de Gennes, F. Brochard-Wyrat, and D. Quéré. *Capillarity and Wetting Phenomena: Drops, Bubbles, Pearls, Waves*, Springer, 2004.

[52] U-S Jeng, L. Esibov, L. Crow, and A. Steyerl. *J. Phys.: Condens. Matter*, 10:4955, 1998.

[53] I. Zacharoudiou. *Viscous Fingering and Liquid Crystals in Confinement*, PhD thesis, 2012.

[54] C. Rascón and A. O. Parry. *Nature*, 407:986, 2000.

[55] C. Rascón and A. O. Parry. *J. Chem. Phys.*, 112(11):5175, 2000.

[56] D. G. A. L. Aarts. *The interface in Demixed Colloid-polymer Systems: Wetting, Waves and Droplets*, PhD thesis, 2005.

[57] S. M. Ilett, A. Orrock, W. C. K. Poon, and P. N. Pusey. *Phys. Rev. E*, 51:1344, 1955.

[58] A. Moussaïd, W. C. K. Poon, P. N. Pusey, and M. F. Soliva. *Phys. Rev. Lett.*, 82(1):225, 1999.

[59] D. G. A. L. Aarts. *J. Phys. Chem. B*, 109:7407, 2005.

[60] D. G. A. L. Aarts, R. P. A. Dullens, and H. N. W. Lekkerkerker. *New J. Phys.*, 7:40, 2005.

[61] D. Derks, D. G. A. L. Aarts, D. Bonn, and A. Imhof. *J. Phys.: Condens. Matter*, 20:404208, 2008.

[62] Y. Hennequin, D. G. A. L. Aarts, J. O. Indekeu, H. N. W. Lekkerkerker, and D. Bonn. *Phys. Rev. Lett.*, 100:178305, 2008.

[63] A. O. Parry, C. Rascón, E. A. G. Jamie, and D. G. A. L. Aarts. *Phys. Rev. Lett.*, 108:246101, 2012.

[64] G. M. Whitesides. *Nature*, 442:368, 2006.

[65] E. A. G. Jamie, R. P. A. Dullens, and D. G. A. L. Aarts. *J. Phys.: Condens. Matter*, 24:284120, 2012.

[66] E. A. G. Jamie, R. P. A. Dullens, and D. G. A. L. Aarts. *J. Chem. Phys.*, 137:204902, 2012.

[67] M. D. Howe. *Synthesis of Novel Polymeric Colloidal Particles for Use in Confocal Scanning Laser Microscopy*, Part II thesis, 2008.

[68] E. A. G. Jamie. *Colloidal Interfaces in Confinement*, PhD thesis, 2011.

[69] E. Kumacheva, O. Kalinina, and L. Lilge. *Adv. Mater.*, 11(3):231, 1999.

[70] G. Bosma, C. Pathmamanoharan, E. H. A. de Hoog, W. K. Kegel, A. van Blaaderen, and H. N. W. Lekkerkerker. *J. Coll. Inf. Sci.*, 245:292, 2002.

[71] G. H. Koenderink, D. G. A. L. Aarts, V. W. A. de Villeneuve, A. P. Philipse, R. Tuinier, and H. N. W. Lekkerkerker. *Biomacromolecules*, 4:129, 2003.

[72] G. H. Koenderink, S. Sacanna, D. G. A. L. Aarts, and A. P. Philipse. *Phys. Rev. E*, 69:021804, 2004.

[73] E. A. G. Jamie, H. H. Wensink, and D. G. A. L. Aarts. *Soft Matter*, 6:250, 2010.

[74] P. N. Pusey, W. C. K. Poon, S. M. Ilett, and P. Bartlett. *J. Phys.: Condens. Matter*, 6:A29, 1994.

[75] P. B. Warren. *Langmuir*, 13:4588, 1997.

[76] R. P. Sear and D. Frenkel. *Phys. Rev. E*, 55(2):1677, 1997.

[77] M. Fasolo and P. Sollich. *Phys. Rev. Lett.*, 91(6):068301, 2003.

[78] M. Fasolo and P. Sollich. *Phys. Rev. E*, 70:041410, 2004.

[79] P. Paricaud, S. Varga, P. T. Cummings, and G. Jackson. *Chem. Phys. Lett.*, 398:489, 2004.

[80] J. W. Cahn. *J. Chem. Phys.*, 42:93, 1965.

[81] J. W. Cahn. *Acta Metallurgica*, 9:795, 1961.

[82] J. W. Cahn and J. E. Hilliard. *J. Chem. Phys.*, 31:688, 1959.

[83] J. W. Cahn and J. E. Hilliard. *J. Chem. Phys.*, 28:258, 1958.

[84] K. Binder and D. Stauffer. *Phys. Rev. Lett.*, 33:1006, 1974.

[85] D. G. A. L. Aarts. *Soft Matter*, 3:19, 2007.

[86] V. W. A. de Villeneuve, J. M. J. van Leeuwen, J. W. J. de Folter, D. G. A. L. Aarts, W. van Saarloos, and H. N. W. Lekkerkerker. *Europhys. Lett.*, 81:60004, 2008.

[87] S. A. Safran. *Statistical Thermodynamics of Surface, Interface and Membranes (Frontiers in Physics)*, Westview Press, 2003.

[88] H. N. W. Lekkerkerker, V. W. A. Villeneuve, J. W. J. de Folter, M. Schmidt, Y. Hennequin, D. Bonn, J. O. Indekeu, and D. G. A. L. Aarts. *Eur. Phys. J. B*, 64:341, 2008.

[89] M. Tolan, O. H. Seeck, J. P. Schlomka, W. Press, J. Wang, S. K. Sinha, Z. Li, M. H. Rafailovich, and J. Sokolov. *Phys. Rev. Lett.*, 81(13):2731, 1998.

[90] D. G. A. L. Aarts. *Soft Interfaces: the Case of Colloid-Polymer Mixtures*, Oxford University Press, 2013.

[91] K. R. Mecke and S. Dietrich. *Phys. Rev. E*, 59:6766, 1999.

[92] E. M. Blokhuis, J. Kuipers, and R. L. C. Vink. *Phys. Rev. Lett.*, 101:086101, 2008.

[93] P. Tarazona, E. Chacón, and F. Bresme. *J. Phys.: Condens. Matter*, 24:284123, 2012.

[94] V. W. A. de Villeneuve, J. M. J. van Leeuwen, W. van Saarloos, and H. N. W. Lekkerkerker. *J. Chem. Phys.*, 129:164710, 2008.

[95] J. F. Steffe. *Rheological Methods in Food Process Engineering*, Freeman Press, 1996.

[96] M. M. Cross. *J. Coll. Sci.*, 20:417, 1965.

[97] W. P. Cox and E. H. Merz. *J. Pol. Sci.*, 28:619, 1958.

[98] G. M. Whitesides, E. Ostuni, S. Takayama, X. Jiang, and D. E. Ingber. *Annu. Rev. Biomed. Eng.*, 3:335, 2001.

[99] Y. Xia and G. M. Whitesides. *Angew. Chem. Int. Ed.*, 37:550, 1998.

[100] Y. Xia and G. M. Whitesides. *Annu. Rev. Mater. Sci.*, 28:153, 1998.

[101] Y. Xia, J. J. McClelland, R. Gupta, D. Qin, X-M Zhao, L. L. Sohn, R. J. Celotta, and G. M. Whitesides. *Adv. Mater.*, 9:147, 1997.

[102] X-M. Zhao, Y. Xia, and G. M. Whitesides. *J. Mater. Chem.*, 7(7):1069, 1997.

[103] P. Kim, K. W. Kwon, M. C. Park, S. H. Lee, S. M. Kim, and K. Y. Suh. *Biochip Journal*, 2(1):1, 2008.

[104] M. A. Burns, B. N. Johnson, S. N. Brahmasandra, K. Handique, J. R. Webster, M. Krishnan, T. S. Sammarco, P. M. Man, D. Jones, D. Heldsinger, C. H. Mastrangelo, and D. T. Burke. *Science*, 282:484, 1998.

[105] D. Janasek, J. Franzke, and A. Manz. *Nature*, 442:374, 2006.

[106] H. Craighead. *Nature*, 442:387, 2006.

[107] J. El-Ali, P. K. Sorger, and K. F. Jensen. *Nature*, 442:403, 2006.

[108] A. del Campo and C. Greiner. *J. Micromech. Microeng.*, 17:R81, 2007.

[109] Microchem. *SU-8 2000*, Processing Guidelines, 2010.

[110] V. Prasad, D. Semwogerere, and E. R. Weeks. *J. Phys.: Condens. Matter*, 19:113102, 2007.

[111] P. Habdas and E. R. Weeks. *Curr. Opin. Colloid Interface Sci.*, 7:196, 2002.

[112] M. Minsky. *Scanning*, page 128.

[113] T. Wilson. *Confocal Microscopy*, Academic Press, 1990.

[114] S. W. Paddock. *Molecular Biotechnology*, 16:127, 2000.

[115] R. H. Webb. *Rep. Prog. Phys.*, 59:427, 1996.

[116] R. P. A. Dullens. *Structure and Dynamics of Colloidal Hard Spheres in Real Space*, PhD thesis, 2005.

[117] P. G. Saffman and G. Taylor. *Proc. R. Soc. Lond. A*, 245:312, 1958.

[118] Y. Couder. *Perspectives in Fluid Dynamics*, Cambridge University Press, Cambridge,

2000.

[119] D. Bensimon, L. P. Kadanoff, S. Liang, B. I. Shraiman, and C. Tang. *Rev. Mod. Phys.*, 58(4), 1986.

[120] L. Paterson. *J. Fluid Mech.*, 113:513, 1981.

[121] L. Paterson. *Phys. Rev. Lett.*, 52(18):1621, 1984.

[122] R. Lenormand. *Physica A*, 140:114, 1986.

[123] X. Cheng, L. Xu, A. Patterson, H. M. Jaeger, and S. R. Nagel. *Nat. Phys.*, 4:234, 2008.

[124] B. Sandnes, E. G. Flekkøy, H. A. Knudsen, K. J. Måløy, and H. See. *Nature Communications*, 2:288, 2011.

[125] A. Lindner and C. Wagner. *Comptes Rendus Physique*, page 712, 2009.

[126] R. Ledesma-Aguilar, I. Pagonabarraga, and A. Hernández-Machado. *Physics of Fluids*, 19(10):102113, 2007.

[127] T. T. Al-Housseiny, P. A. Tsai, and H. A. Stone. *Nature Physics*, 8:747, 2012.

[128] B. Jha, L. Cueto-Felgueroso, and R. Juanes. *Phys. Rev. Lett.*, 106:194502, 2011.

[129] L. W. Lake. *Enhanced Oil Recovery*, Prentice Hall, 1989.

[130] S. B. Gorell and G. M. Homsy. *SIAM J. Appl. Math.*, 43:79, 1983.

[131] F. M. Orr and J. J. Taber. *Science*, 224(4649):563, 1984.

[132] T. T. Norton and E. J. Fernandez. *Ind. Eng. Chem. Res.*, 35(7):2460, 1996.

[133] J. W. McLean and P. G. Saffman. *J. Fluid Mech.*, 102:455, 1981.

[134] B. I. Shraiman. *Phys. Rev. Lett.*, 56(19):2028, 1986.

[135] D. C. Hong and J. S. Langer. *Phys. Rev. Lett.*, 56(19):2032, 1986.

[136] R. Combescot, T. Dombre, V. Hakim, Y. Pomeau, and A. Pumir. *Phys. Rev. Lett.*, 56(19):2036, 1986.

[137] P. Tabeling and A. Libchaber. *Phys. Rev. A*, 33(1):794, 1986.

[138] P. Pelcé. *Dynamic of Curved Fronts*, Academic Press, 1988.

[139] C. W. Park and G. M. Homsy. *J. Fluid Mech.*, 139:291, 1984.

[140] P. Tabeling, G. Zocchi, and A. Libchaber. *J. Fluid Mech.*, 177:67, 1987.

[141] G. M. Homsy. *Ann. Rev. Fluid Mech.*, 19:271, 1987.

[142] R. Ledesma-Aguilar, A. Hernández-Machado, and I. Pagonabarraga. *Physics of Fluids*, 19(10):102112, 2007.

[143] M. Moseler and U. Landman. *Science*, 289:1165, 2000.

[144] J. Eggers. *Phys. Rev. Lett.*, 89:084502, 2002.

[145] G. Grün, K. Mecke, and M. Rauscher. *J. Stat. Phys.*, 122:1261, 2006.

[146] M. Alava, M. Dubé, and M. Rost. *Advances in Physics*, 53(2):83, 2004.

[147] E. A. G. Jamie, H. H. Wensink, and D. G. A. L. Aarts. *J. Stat. Mech.*, page P11008, 2010.

[148] Ph. Tordjeman. *Physics of Fluids*, 19:118102, 2007.

[149] S. Hell, G. Reiner, C. Cremer, and E. H. K. Stelzer. *Journal of Microscopy*, 169:391, 1993.

[150] M. R. Swift, W. R. Osborn, and J. M. Yeomans. *Phys. Rev. Lett.*, 75:830, 1995.

[151] M. R. Swift, E. Orlandini, W. R. Osborn, and J. M. Yeomans. *Phys. Rev. E*, 54:5041, 1996.

[152] D. Halpern and D. Gaver. *J. Comput. Phys.*, 115:366, 1994.

[153] E. Pitts. *J. Fluid Mech.*, 97:53, 1980.

[154] F. Bretherton. *J. Fluid Mech.*, 10:166, 1961.

[155] G. Taylor. *J. Fluid Mech.*, 10:161, 1961.

[156] F. Fairbrother and A. E. Stubbs. *Studies in Electro-endosmosis*, page 527, 1935.

[157] D. A. Reinelt and P. G. Saffman. *SIAM J. Sci. Stat. Comput.*, 6(3):542, 1985.

[158] G. Davies. *Development of Colloid-polymer Mixtures for the Study of Hydrodynamic Instabilities in Microfluidics*, Part II thesis, 2008.

[159] C. W. Park, S. Gorell, and G. M. Homsy. *J. Fluid Mech.*, 141:257, 1984.

[160] L. D. Landau and E. M. Lifshitz. *Fluid Mechanics Second Edition*, Pergamon Press, New York, 1987.

[161] A. Lindner, D. Bonn, E. C. Poiré, M. B. Amar, and J. Meunier. *J. Fluid Mech.*, 469:237, 2002.

[162] T. Dang-Vu, R. Jha, S. Y. Wu, D. D. Tannant, J. Masliyah, and Z. Xu. *Colloids and Surfaces A: Physicochemical and Engineering Aspects*, 337:80, 2009.

[163] A. J. Degregoria and L. W. Schwartz. *J. Fluid Mech.*, 164:383, 1986.

[164] D. A. Kessler and H. Levine. *Rapid Communications*, 33(5):3625, 1986.

[165] S. Liang. *Phys. Rev. A*, 33(4):2663, 1986.

[166] D. Bensimon. *Phys. Rev. A*, 33(2):1302, 1986.

[167] C. W. Park and G. M. Homsy. *Phys. Fluids*, 28(6):1583, 1985.

[168] C. Chevalier, A. Lindner, and E. Clément. Saffman-taylor instability in a non-brownian suspension: Finger selection and destabilization. page 1, 2007.

[169] Lord Rayleigh. *Scientific paper*, Cambridge, University Press, Cambridge. Vol. II:200, 1900.

[170] G. I. Taylor. *Proc. R. Soc. London, Ser. A*, 201:192, 1950.

[171] D. J. Lewis. *Proc. R. Soc. London, Ser. A*, 202:81, 1950.

[172] A. Jesorka and O. Orwar. *Nature Nanotechnolgy*, 7:6, 2012.

[173] M. Whitby and N. Quirke. *Nature Nanotechnolgy*, 2:87, 2007.

[174] S. K. Sia and G. M. Whitesides. *Electrophoresis*, 24:3563, 2003.

[175] P. Domachuk, K. Tsioris, F. G. Omenetto, and D. L. Kaplan. *Advanced Materials*, 22:249, 2010.

[176] P. G. de Gennes. *Rev. Mod. Phys.*, 57:827, 1985.

[177] D. Bonn, J. Eggers, J. Indekeu, J. Meunier, and E. Rolley. *Rev. Mod. Phys.*, 81:739, 2009.

[178] C. Huh and L. E. Scriven. *J. Colloid Interface Sci.*, 35:85, 1971.

[179] P. A. Thompson and M. O. Robbins. *Phys. Rev. Lett.*, 63:766, 1989.

[180] J. H. Snoeijer and B. Andreotti. *Annu. Rev. Fluid Mech.*, 45:269, 2013.

[181] T. D. Blake and K. J. Ruschak. *Nature*, 282:489, 1979.

[182] T. D. Blake and J. de Coninck. *Adv. Coll. Int. Sci.*, 96:21, 2002.

[183] C. Duez, C. Ybert, C. Clanet, and L. Bocquet. *Nature Physics*, 3:180, 2007.

[184] J. H. Snoeijer, J. Ziegler, B. Andreotti, M. Fermigier, and J. Eggers. *Phys. Rev. Lett.*, 100:244502, 2008.

[185] I. Peters, J. H. Snoeijer, A. Daerr, and L. Limat. *Phys. Rev. Lett.*, 103:114501, 2009.

[186] R. Ledesma-Aguilar, R. Nistal, A. Hernández-Machado, and I. Pagonabarraga. *Nature Mater.*, 10:367, 2011.

[187] A. Marchand, T. S. Chan, J. H. Snoeijer, and B. Andreotti. *Phys. Rev. Lett.*, 108:204501, 2012.

[188] D. Jacqmin. *J. Fluid Mech.*, 402:57, 2000.

[189] A. J. Briant and J. M. Yeomans. *Phys. Rev. E*, 69:031603, 2004.

[190] T. Qian, X.-P. Wang, and P. Sheng. *Phys. Rev. Lett.*, 93(9):094501, 2004.

[191] H. K. Moffatt. *J. Fluid Mech.*, 18:1, 1964.

[192] P. Yue, C. Zhou, and J. J. Feng. *J. Fluid Mech.*, 645:279, 2010.

[193] R. Ledesma-Aguilar, A. Hernández-Machado, and I. Pagonabarraga. *Phys. Rev. Lett.*, 110:264502, 2013.

[194] E. Vandre, M. Carvalho, and S. Kumar. *J. Fluid Mech.*, 707:496, 2012.

[195] J. Petit, D. Rivière, H. Kellay, and J. P. Delvile. *Proc. Nat. Acad. Sci. USA*, 109:18327, 2012.

[196] Y. Hennequin, D. G. A. L. Aarts, J. H. van der Wiel, G. Wegdam, J. Eggers, H. N. W. Lekkerkerker, and D. Bonn. *Phys. Rev. Lett.*, 97:244502, 2006.

[197] L. Bocquet and E. Lauga. *Nature Mater.*, 10:334, 2011.

[198] A. Carré, J. Gastel, and M. Shanahan. *Nature*, 379:432, 1996.

[199] S. Ramaswamy. *Annu. Rev. Cond. Matter Phys.*, 1:323, 2010.

[200] D. Bartolo and D. G. A. L. Aarts. *Soft Matter*, 8:10530, 2012.

[201] P. Gravensen, J. Branebjerg, and O. S. Jensen. *J. Micromech. Microeng.*, 3:168, 1993.

[202] B. H. Weigl and P. Yager. *Science*, 283:346, 1999.

[203] G. M. Whitesides and A. D. Stroock. *Phys. Today*, 42:42, 2001.

[204] H. Shi, W. B. Tsai, M. D. Garrison, S. Ferrari, and B. D. Ratner. *Nature*, 398:593, 1999.

[205] S. Shibuichi, T. Yamamoto, T. Onda, and K. Tsujii. *J. Colloid Interf. Sci.*, 208:287, 1998.

[206] J. Bico, C. Marzolin, and D. Quéré. *Europhys. Lett.*, 47:220, 1999.

[207] K. Rejmer, S. Dietrich, and M. Napiórkowski. *Phys. Rev. E*, 60:4027, 1999.

[208] A. O. Parry, C. Rascón, and A. J. Wood. *Phys. Rev. Lett.*, 83:5535, 1999.

[209] A. O. Parry, C. Rascón, and A. J. Wood. *Phys. Rev. Lett.*, 85:345, 2000.

[210] A. O. Parry, A. J. Wood, and C. Rascón. *J. Phys.: Condens. Matter*, 12:7671, 2000.

[211] A. O. Parry, A. J. Wood, and C. Rascón. *J. Phys.: Condens. Matter*, 13:4591, 2001.

[212] A. O. Parry, A. J. Wood, E. Carlon, and A. Drzewiński. *Phys. Rev. Lett.*, 87:196103, 2001.

[213] M. Heni and H. Löwen. *Phys. Rev. Lett.*, 85:3668, 2000.

[214] W. F. Saam. *J. Low Temp. Phys.*, 157:77, 2009.

[215] L. Bruschi, A. Carlin, and G. Mistura. *J. Chem. Phys.*, 115:6200, 2001.

[216] L. Bruschi, A. Carlin, and G. Mistura. *Phys. Rev. Lett.*, 89:166101, 2002.

[217] L. Bruschi, A. Carlin, A. O. Parry, and G. Mistura. *Phys. Rev. E*, 68:021606, 2003.

[218] L. Bruschi, A. Carlin, and G. Mistura. *J. Phys.: Condens. Matter*, 15:S315, 2003.

[219] L. Bruschi, G. Fois, G. Mistura, M. Tormen, V. Garbin, E. di Fabrizio, A. Gerardino, and M. Natali. *J. Chem. Phys.*, 125:144709, 2006.

[220] M. Schmidt, A. Fortini, and M. Dijkstra. *J. Phys.: Condens. Matter*, 15:S3411, 2003.

[221] D. G. A. L. Aarts and H. N. W. Lekkerkerker. *J. Phys.: Condens. Matter*, 16:S4231, 2004.

[222] S. Dietrich. in *Phase Transitions and Critical Phenomena*, edited by C. Domb and J. Lebowitz. Academic, London:Vol. 12, 1988.

[223] J. Krim, J. G. Dash, and J. Suzanne. *Phys. Rev. Lett.*, 52:640, 1984.

[224] B. V. Derjaguin. in *Fluid Interfacial Phenomena*, edited by C. A. Croxton. Wiley, New York:page 739, 1986.

[225] J. O. Indekeu, D. G. A. L. Aarts, H. N. W. Lekkerkerker, Y. Hennequin, and D. Bonn. *Phys. Rev. E*, 81:041604, 2010.

[226] P. Pfeifer, Y. J. Wu, M. W. Cole, and J. Krim. *Phys. Rev. Lett.*, 62:1997, 1989.

[227] W. Helfrich. in *Les Houches, Session XLVIII, Liquids at Interfaces*, edited by J. Charvolin, J. -F. Joanny, and J. Zinn-Justin. Elsevier, Amsterdam, 1990.

[228] M. Schick. in *Les Houches, Session XLVIII, Liquids at Interfaces*, edited by J. Charvolin, J. -F. Joanny, and J. Zinn-Justin. Elsevier, Amsterdam, 1990.

[229] B. V. Derjaguin. *Acta Phys. Chem.*, 12:181, 1940.

[230] R. Evans and U. M. B. Marconi. *J. Chem. Phys.*, 86:7138, 1987.

[231] R. Evans. *J. Phys.: Condens. Matter*, 2:8989, 1990.

List of publications

To date the following publications based upon work in this thesis have been submitted or are in preparation:

Siti Aminah Setu, Ioannis Zacharoudiou, Gareth J. Davies, Denis Bartolo, Sébastien Moulinet, Ard A. Louis, Julia M. Yeomans and Dirk G.A.L. Aarts, *Viscous fingering at ultralow interfacial tension*, Soft Matter, (2013). (Chapter 4 and 5).

Siti Aminah Setu, Roel P. A. Dullens, Aurora Hernández-Machado, Ignacio Pagonabarraga, Dirk G. A. L. Aarts and Rodrigo Ledesma-Aguilar, *Superconfinement tailors fluid flow at micro-scales*, Nature Communications, (in review). (Chapter 6).

Siti Aminah Setu, Andy O. Parry, Carlos Rascón, Dirk G. A. L. Aarts, *Wetting phenomena at geometrically sculpted wedges*, In preparation. (Chapter 7).

Acknowledgments

In the name of Allah, the Most Gracious and the Most Merciful.

Alhamdulillah. All praises to Allah. For all the things You have given to me, I never thanked You once.

I would like to express my sincere gratitude to my supervisor Dirk Aarts for the continuous support of my DPhil study, for his patience, motivation, enthusiasm, and immense knowledge. His guidance helped me during the research and writing of this thesis. Also, thanks to him for always understanding me as a student parent. An equal thanks to Roel Dullens for his additional encouragement.

Special thanks to Ioannis Zacharoudiou, Rodrigo Ledesma-Aguilar, Carlos Rascón and Andy Parry for our collaborations.

Being a part of the Soft Matter group leaves wonderful memories in me. This is the place where I gained a lot of knowledge about science and life, and meeting great people: Liz, Tom, Oli, Paola, Sam, Mike, Alice, Julia, Harry, Ellie, Seb, Nina, Lia, Raam, Oli B, Francois, Arran, Kira and Huzaifah.

Next on the list, eternal thanks to my husband, Azad Anugerah, for his love and constant support, and for allowing me time away from family stuff to get this thesis completed. But most of all, thank you for being my best friend. To my lovely daughter, Ainul Mardhiah, and son, Baihaqi Wafiuddin, a massive thank-you for inspiring me to finish my thesis and for always putting a smile on my face. Having both of you during this time is a great challenge, but continuously teaches me to be a better person. To all of you this thesis is dedicated.

To my mother, Zaibedah Misran and father, Setu Ahmad, thank you for your prayers, love, support, sacrifices, and unwavering belief in me. Without you, I would not be the person I am today. Thanks also to my brothers and sisters who are so supportive in whatever I do in my life. A special mention to my in-laws, for accepting me as your family.

I would also like to thank my best friends: KB and Ramlee, Aliah, Aliza, Ana and Ridza, Yati and Syarif, and to all Malaysian students at the University of Oxford, for always offering a helping hand to us and for making our weekends never dull.

Last but not least, I would also like to express my sincere thanks to the Ministry of Higher Education Malaysia and Universiti Teknologi Malaysia (UTM) for financial support. An extra warm thank you to everyone who helped me in making this study a reality.